Measurement of hadronic final states with the L3 Detector at LEP

D I S S E R T A T I O N

zur Erlangung des akademischen Grades

doctor rerum naturalium

(Dr. rer. nat.)

im Fach Physik

eingereicht an der

Mathematisch-Naturwissenschaftlichen Fakultät I
der Humboldt-Universität zu Berlin

von

André Krüger

geboren am 19. August 1973 in Hennigsdorf

Präsident der Humboldt-Universität zu Berlin
Prof. Dr. Jürgen Mlynek

Dekan der Mathematisch-Naturwissenschaftlichen Fakultät I
Prof. Dr. Michael Linscheid

Gutachter:
Prof. Dr. Eva-Maria Kabuss
Prof. Dr. John H. Field
Prof. Dr. Thomas Hebbeker

Tag der mündlichen Prüfung: 21.10.2002

Zusammenfassung

Die Messung von $\sigma_{\rm had}$ und $\rm R_b$ mit dem L3 Detektor am LEP Speicherring bei Schwerpunktsenergien von 192 GeV bis 207 GeV wird vorgestellt. Aus den Messwerten wurden die Vektor- und Axial-Vektor-Kopplungen des Z Bosons an die bottom quarks bestimmt. Die Vektor- und Axial-Vektor-Kopplungen testen die Gültigkeit des Standardmodells der Elementarteilchenphysik. Abweichungen der Messungen von der Standardmodellvorhersage wurden im Rahmen erweiterter Modelle diskutiert.
Die Prozesse $\rm e^+e^- \to$ Hadronen und $\rm e^+e^- \to b\bar{b}$ wurden untersucht. Die hadronischen Ereignisse wurden mit einer effektiven Schwerpunktsenergie von $\sqrt{\rm s'} > 0.85\sqrt{\rm s}$ selektiert und aus diesen Ereignisse mit B Hadronen separiert. Die Selektion von Ereignissen mit B Hadronen wurde mit dem L3 B-tag durchgeführt. Dieser nutzt die relativ lange Lebensdauer B-Hadronen. Bei der grössten erreichten Schwerpunktsenergie, $\sqrt{s}$=207 GeV, wurden folgende Werte für $\sigma_{\rm had}$ und $\rm R_b$ gemessen:

$$\sigma_{\rm had} = 17.86 \pm 0.54(\text{stat.}) \pm 0.32(\text{sys.}) \text{ pb}$$

$$\rm R_b = 0.191 \pm 0.014(stat.) \pm 0.007(sys.) - 0.256 \frac{(R_c - R_c^{used})}{R_c}.$$

Die Vektor- und Axial-Vektor-Kopplungen sowie die links- und rechts-händigen Kopplungen wurden mittels eines χ^2-fits an die L3 Messungen bestimmt und betragen:

$$\bar{\rm g}_{\rm V}^{\rm b} = -0.302^{+0.033}_{-0.043}$$
$$\bar{\rm g}_{\rm A}^{\rm b} = -0.530^{+0.027}_{-0.018}$$
$$\bar{\rm g}_{\rm L}^{\rm b} = -0.416^{+0.008}_{-0.008}$$
$$\bar{\rm g}_{\rm R}^{\rm b} = +0.114^{+0.026}_{-0.035}$$

Darüberhinaus wurden die Kopplungen durch einen χ^2-fit an kombinierte LEP und SLD Messungen bestimmt. Die Resultate beider Analysen wurden verglichen. Die Ergebnisse für die Kopplungen, abgeleitet aus den kombinierten Messungen von LEP und SLD, weisen eine Abweichung von ca. 3 Standardabweichungen von der Standardmodellvorhersage auf. Die Messergebnisse wurden genutzt, um nach neuen Phänomenen in der Elementarteilchenphysik zu suchen. Erweiterungen des Standardmodells wie Vier-Fermion Kontaktwechselwirkungen, Modelle mit einem zusätzlichen schweren Eichboson, Z′, Graviton Austausch und räumliche Ausdehnungen von Quarks wurden untersucht und Grenzen werden angegeben.

Abstract

The measurement of $\sigma_{\rm had}$ and $\rm R_b$ with the L3 detector at the LEP collider at centre–of–mass energies from 192 GeV to 207 GeV are presented. From the measurements are determined the vector and axial vector couplings of the Z boson to the bottom quarks. The vector and axial vector couplings probe the validity of the Standard Model of elementary particle physics. Deviations of the measurements from the Standard Model prediction are discussed in the framework of extended models.
The process $\rm e^+e^- \to$ hadrons and $\rm e^+e^- \to b\bar{b}$ were studied. The hadronic events were selected at an effective centre–of–mass energy of $\sqrt{\rm s'} > 0.85\sqrt{\rm s}$ and from these, events with B hadrons were separated. The selection of events containing B hadrons is performed using the L3 B-tag, exploiting the relatively long lifetime of B hadrons. At the highest centre–of–mass energy reached, $\sqrt{s}$=207 GeV, the following values of $\sigma_{\rm had}$ and $\rm R_b$ are measured:

$$\sigma_{\rm had} = 17.86 \pm 0.54(\rm stat.) \pm 0.32(\rm sys.)\ pb$$

$$\rm R_b = 0.191 \pm 0.014(stat.) \pm 0.007(sys.) - 0.256\frac{(R_c - R_c^{used})}{R_c}$$

The vector and axial vector couplings and the left- and right-handed couplings achieved from a χ^2-fit to the L3 measurements amount to:

$$\bar{\rm g}_{\rm V}^{\rm b} = -0.302^{+0.033}_{-0.043}$$

$$\bar{\rm g}_{\rm A}^{\rm b} = -0.530^{+0.027}_{-0.018}$$

$$\bar{\rm g}_{\rm L}^{\rm b} = -0.416^{+0.008}_{-0.008}$$

$$\bar{\rm g}_{\rm R}^{\rm b} = +0.114^{+0.026}_{-0.035}$$

The couplings were determined from a χ^2-fit to the combined LEP and SLD measurements. The results of both analyses are compared. The couplings achieved from the combined measurements of LEP and SLD show a deviation of almost 3 standard deviations from the Standard Model prediction.
The results are taken to search for new phenomena in Elementary Particle Physics. Extensions of the Standard Model in terms of four-fermion contact interactions, models with one additional heavy gauge boson, Z′, graviton exchange and quark sizes are studied and limits are given.

Contents

1 Introduction **15**

2 Theory **17**
2.1 Quantum Field Theory and Gauge Invariance . . . 17
2.2 The Standard Model . . . 18
2.3 Hadronization . . . 24
2.4 Fermion Pair Production . . . 26
2.5 Higher Order Corrections . . . 29
2.5.1 Electroweak Corrections . . . 30
2.5.2 The running QED coupling constant . . . 32
2.5.3 QCD Radiative Corrections . . . 33
2.5.4 Improved Born Approximation . . . 34
2.6 QED corrections . . . 34
2.7 The Process $e^+e^- \rightarrow$ Hadrons . . . 36
2.8 Beyond the Standard Model . . . 39
2.8.1 Contact Interactions . . . 40
2.8.2 Fermion Sizes . . . 41
2.8.3 Extra Z Bosons . . . 41
2.8.4 Graviton Exchange . . . 43

3 The L3 Experiment at LEP **45**
3.1 The e^+e^-Collider LEP . . . 45
3.2 The L3 coordinate system . . . 46
3.3 The L3 Detector . . . 47
3.3.1 The Silicon Microvertex Detector . . . 47
3.3.2 The Central Tracking Chambers . . . 48
3.3.3 The Electromagnetic Calorimeter (BGO) . . . 51
3.3.4 The Scintillation Counters . . . 52
3.3.5 The Hadron Calorimeter . . . 52
3.3.6 The Muon Chambers . . . 53
3.3.7 The Luminosity Monitor . . . 55
3.3.8 The Trigger System . . . 55

4 The Luminosity Measurement **57**
4.1 Basic Principles . . . 57
4.2 Measurement of the Integrated Luminosity . . . 58

5 Monte Carlo Event Simulation and Data Reconstruction **61**
5.1 The General Scheme . . . 61
5.2 The Signal Process . . . 61
5.2.1 Low Energy Signal Events . . . 62
5.3 The Background Processes . . . 63
5.4 The Event Simulation and Reconstruction . . . 64
5.4.1 Processes in this Analysis . . . 65

6 The Event Selection **67**
6.1 Selection of Hadronic Events at High Energies . . . 67
6.2 Treatment of Low Energy Background . . . 70
6.3 Results of the Hadronic Event Selection . . . 71
6.4 B-tagging in L3 . . . 76
6.4.1 Decay Length Significance . . . 77
6.4.2 Impact Parameter Significance . . . 78
6.5 Results of the B-tagging . . . 80

7 The Measurement of the Total Hadronic Cross Section **87**
7.1 The Measurement of σ_{had} . . . 87
7.1.1 The Selection Efficiency . . . 87
7.1.2 The Trigger Efficiency . . . 88
7.2 Systematic Uncertainties . . . 89
7.3 Final Results . . . 91

8 The Measurement of R_b **95**
8.1 The Measurement of R_b . . . 95
8.1.1 The Tagging Efficiencies . . . 97
8.2 Statistical and Systematic Uncertainties . . . 98
8.3 Correlation between R_b and R_c . . . 104
8.4 Final Results . . . 104

9 Interpretation **109**
9.1 Analysis Method . . . 109
9.2 The Effective Vector and Axial Vector Couplings in the SM . . . 110
9.3 New Physics . . . 118
9.3.1 Contact Interactions . . . 118
9.3.2 Fermion Sizes . . . 119
9.3.3 Extra Z Bosons . . . 120
9.3.4 Graviton Exchange . . . 121

10 Conclusions and Outlook **123**
10.1 Conclusions 125

A Jet Clustering Algorithm **127**

B Efficiency Calculation **129**

C Correlation Coefficients **131**

Bibliography **133**

Acknowledgements **137**

List of Figures

2.1 The hadronization process as described in the text. After the production of a quark pair, the parton shower is produced and the hadronization starts. The heavy and unstable hadrons resulting from the hadronization decay to stable hadrons like pions and kaons and leptons like electrons and muons and real photons. 24
2.2 The Feynman diagram for electron-positron annihilation and fermion pair production. 26
2.3 The Feynman diagram for electron-positron annihilation and fermion pair production including higher order corrections. 29
2.4 Example diagrams for electroweak corrections with fermion loops, modifying the W- and the Z-propagator. 30
2.5 The vertex correction of the process $Z \to b\bar{b}$ due to virtual top quark exchange. 31
2.6 Example diagram for QED corrections: virtual fermion loops in the photon propagator contribute to the running of α. 32
2.7 Example diagrams for QCD corrections due to gluon radiation in the final state (right) and virtual gluon exchange between the final state quarks (left). 34
2.8 Example diagram with initial state radiation. At least one of the initial state leptons radiates a photon before the annihilation. 35
2.9 The dependence of A_{fb}^{b} (left) and R_b (right) on the centre–of–mass energy. The dashed curve is the Standard Model prediction without a selection criterion on the effective centre–of–mass energy, s'. The solid curve depicts the Standard Model prediction with a selection criterion on the effective centre–of–mass energy, $\sqrt{s'} > 0.85\sqrt{s}$. 38
2.10 The dependence of σ_{had} on the centre–of–mass energy, depicted like in Figure 2.9. 38
2.11 The diagram for four-fermion contact interaction. 40

3.1 A general view on the LEP storage ring and the locations of the experiments ALEPH, DELPHI, L3 and OPAL. 46
3.2 A perspective view on the L3 detector. 48
3.3 An inner SMD ladder. The $r - \phi$ side and the $r - z$ side are shown. 49
3.4 A perspective and a front-end view of the SMD. 49

3.5 The r $-$ ϕ view of the central tracker. 50
3.6 The shape of the electric fields in the TEC with a charged particle passing through. 51
3.7 Perspective view on the Z-Chamber surrounding the other parts of the central tracker. 51
3.8 Side view on the BGO and a detailed description of one of the crystals. . 52
3.9 BGO shower for a photon/electron and a hadron. 53
3.10 A perspective view on the hadron calorimeter. One can see the 9 rings with 16 modules each for the barrel and the three rings (2 inner and 1 outer ring) of the endcaps. Furthermore one sees the position relative to the other subdetectors described above. 54
3.11 The P-chamber structure in the octants. 54
3.12 One part of the luminosity monitor. SLUM is the silicon track detector. . 55

5.1 A dijet event in the L3 detector. A view along the beamline with the cross section of the L3 detector is shown. The particle tracks and energy depositions in the different subdetector shells are recognisable. 62
5.2 The signal event process $e^+e^- \rightarrow q\bar{q}(\gamma)$. 62
5.3 Example diagrams for the listed background processes are shown. a) is a corresponding diagram for the process $e^+e^- \rightarrow W^+W^-(\gamma)$. The process $e^+e^- \rightarrow We\nu$ is among others described by b), where the W boson decays hadronically. In c) the process $e^+e^- \rightarrow ZZ$ is shown, where at least one of the pair-produced Z bosons decays hadronically. In d) a Z boson is radiated and decays hadronically. e) shows the τ pair-production, where τ leptons decay and produce two low multiplicity jets. The process $e^+e^- \rightarrow e^+e^-$hadrons yields two high multiplicity quark jets, that are produced back-to-back in the rϕ-plane but not at full energy. 64

6.1 The distribution of s$'$ shown for $\sqrt{s} = 206.7$GeV. The black dots represent the data, the open histogram represents the generated signal events and the hatched histogram represents the generated background events. The selection criterion $\sqrt{s'} > 0.85\sqrt{s}$ is indicated by the arrow. 68
6.2 The distribution of the visible energy is shown for $\sqrt{s} = 206.7$GeV. The visible energy normalised to the centre–of–mass energy, $\sqrt{s}$, after the cut on on the effective centre–of–mass energy, s$'$. The selection criterion $E_{vis} > 0.6\sqrt{s}$ is indicated by the arrow. 69
6.3 The collinearity between two jets. The left picture shows the jets as seen in the detector with the collinearity for this event. The right picture shows the collinearity distribution for $\sqrt{s} = 206.7$GeV for data events (black dots) compared to generated events (histogram). The open histogram are the signal events and the hatched histogram are the background events. The selection criterion Collinearity > 2.7 is indicated by the arrow. 70

6.4 The collision of electrons and positrons and the production of a pair of bottom quarks is shown. The innermost part is shown zoomed on the right. The coordinate system of LEP is depicted as reference frame. . . . 76

6.5 The left plot shows a jet where the reconstructed tracks point into the same hemisphere where decay vertex is situated (positive sign). On the right is shown an event where the reconstructed tracks imply that the decay vertex is apparently situated in the other hemisphere (negative sign). IP is the interaction point. 78

6.6 The impact parameter significance for tracks. 79

6.7 The distribution of the discriminant variable obtained for Monte Carlo simulated $q\bar{q}$ events. 81

6.8 Discriminant distributions for the analysed centre–of–mass energies. The black dots are the data, the open histograms represent all generated events and the hatched histograms are the charm and light quark flavours and the background contributions. 85

7.1 The pictures show the deviation of σ_{had} due to the variation of the selection criteria as explained in the text. 91

7.2 The pictures show the measurements of $\sigma_{\mathrm{had}}^{\mathrm{measured}}$ as listed in Table 7.5 (squares) compared to the Standard Model prediction, $\sigma_{\mathrm{had}}^{\mathrm{SM}}$ (curve). . . . 93

8.1 The total uncertainty of R_b as a function of $D_{\mathrm{threshold}}$, here shown as an example for $\sqrt{s} = 206.7\mathrm{GeV}$. The total uncertainty becomes minimal in the range of $D_{\mathrm{threshold}} = 1.7 - 2.3$, for the different centre–of–mass energies listed in Table 4.1. The threshold value is chosen to be $D_{\mathrm{threshold}} = 2.3$ for the analysed centre–of–mass energies, because the value of the total uncertainty is almost constant in the range of $D_{\mathrm{threshold}} = 1.7 - 2.3$. 96

8.2 The upper picture shows the total uncertainty of R_b as a function of the selection criterion for the visible energy, $E_{\mathrm{vis}}/\sqrt{s}$. The resulting uncertainty is almost constant because of the range of the variation (see Figure 6.2). The lower picture shows the fluctuation of R_b, as a function of the selection criterion for the visible energy, $E_{\mathrm{vis}}/\sqrt{s}$, with respect to the measured value of R_b. This is an example picture for $\sqrt{s} = 206.7\mathrm{GeV}$. The resulting systematic uncertainty is listed in Table 8.6 for the individual centre–of–mass energies. 99

8.3 The upper picture shows the total uncertainty of R_b as a function of the selection criterion for the collinearity. The lower picture shows the fluctuation of R_b, as a function of the selection criterion for the collinearity, with respect to the measured value of R_b. This is an example picture for $\sqrt{s} = 206.7\mathrm{GeV}$. The resulting systematic uncertainty is listed in Table 8.6 for the individual centre–of–mass energies. 100

8.4 The distribution of $-\log(y_{34})$. The dots represent the data, the open histogram represents the generated signal events and the hatched histogram represents the generated W^+W^- events. 103
8.5 The matching between data and simulated events for the selected W^+W^- sample as a function of the correction factor. Zero denotes a perfect matching. 104
8.6 The measurement of R_b compared to the Standard Model prediction. The black dots represent the published results from 130 GeV to 189 GeV [72]. The squares represent the results of this analysis. 105

9.1 The Measurement of the effective couplings $\bar{g}_V^b$ and $\bar{g}_A^b$. The circle defined by R_b^0 and the straight lines defined by $A_{fb}^{0,b}$ measured at L3 at the Z-resonance. The intersection defines the possible regions for the allowed values of $\bar{g}_V^b$ and $\bar{g}_A^b$. The asterisk denotes the Standard Model prediction. In addition the results from the low energy e^+e^--experiments at PEP, PETRA and KEK are also shown [80]. 114
9.2 The left picture shows the results for $\bar{g}_V^b$ and $\bar{g}_A^b$ from the fit to the L3 measurements at 68% and 95% confidence level. The right picture shows the results for $\bar{g}_V^b$ and $\bar{g}_A^b$ from the fit to the LEP I and SLD measurements at 68%, 95% and 99%. The asterisk indicates the Standard Model prediction. 117
9.3 The picture shows the results for $\bar{g}_L^b$, $\bar{g}_R^b$ as for the effective vector and axial vector couplings in Figure 9.2. 117
9.4 The left picture shows the lower limits on Λ_- and Λ_+ at 95% confidence level obtained for bottom quarks only (see second column in Table 9.10). The right picture shows the lower limits on Λ_- and Λ_+ at 95% confidence level obtained from the hadronic cross section and the $b\bar{b}$ cross section. The solid bars correspond to the results obtained from the hadronic cross section only (see first column in Table 9.10) and the hatched bars correspond to the results taking also into account the $b\bar{b}$ cross section (see third column in Table 9.10). 120
9.5 The results of the fit to the L3 measurements at 95% confidence level. The left picture shows the lower limit on $m_{Z'}^{limit}$ as function of Θ_6 including only the R_b measurement (dashed curve) and including the measurement of σ_{had}, R_b, the leptonic cross sections and asymmetries (solid curve). The right picture shows the two curves for $m_{Z'}^{limit}$ as function of α_{LR}. 122

A.1 A four jet event in the L3 detector. The front-view of the cross section of the L3 detector is shown. The particle tracks and energy depositions in the different subdetector shells are clustered in four jets. 128

List of Tables

2.1 The fundamental fermions are listed separately as leptons and quarks considering neutrinos as massless. The left-handed fermions are grouped to iso-spin doublets indicated with L. The right-handed fermions are iso-spin singlets indicated with R. The fermions are characterised by their quantum numbers of the weak iso-spin T and its third component T_3, their weak hypercharge Y, their electric charge Q and their colour charge C. . . 23

2.2 The electric charge Q and the colour charge C of the gauge bosons. The index a corresponds to the colour charge of the corresponding gluon. 23

2.3 B hadrons and charmed hadrons and their masses and lifetimes [22]. The quark content is given in parenthesis. The parameter, c, denotes the light-speed. 26

4.1 The centre–of–mass energies and integrated luminosities with their total errors that have been used for this analysis. 59

5.1 The production cross sections, $\sigma_{\mathrm{gen}}^{\mathrm{prod}}$, of the simulated processes given in pico barn. 63

5.2 The processes and corresponding Monte Carlo event generators considered in this analysis. 65

6.1 Selection criteria for high energy hadronic events as discussed in the text. . 71

6.2 $\mathrm{N}_{\mathrm{bkg}}^{\mathrm{gen}}$(before), is the number of generated background events that are analysed for the listed processes. $\mathrm{N}_{\mathrm{bkg}}^{\mathrm{gen}}$(after), is the number of generated background events that remain after the selection is carried out described in section 6.1 $\varepsilon_{\mathrm{bkg}}$, is the selection efficiency calculated from $\mathrm{N}_{\mathrm{bkg}}^{\mathrm{gen}}$(before) and $\mathrm{N}_{\mathrm{bkg}}^{\mathrm{gen}}$(after) according to equation 6.5. 73

6.3 $\mathrm{N}_{\mathrm{signal}}^{\mathrm{gen}}$(before), is the number of generated signal events that are analysed. $\mathrm{N}_{\mathrm{ISR}}^{\mathrm{gen}}$(after), is the number of generated ISR-background events that remain after the selection is carried out described in section 6.1 $\varepsilon_{\mathrm{ISR}}$, is the selection efficiency calculated from $\mathrm{N}_{\mathrm{signal}}^{\mathrm{gen}}$(before) and $\mathrm{N}_{\mathrm{ISR}}^{\mathrm{gen}}$(after) according to equation 6.5. The numbers are not normalised to the number of events in the data. 74

6.4 Numbers of high energy events selected from the data and the expected numbers of generated events for the different centre–of–mass energies. The number of expected events is normalised to the number of selected events in data according to equation 6.2. 74

6.5 The numbers of selected events, background events, ISR-background events are listed. The number of background and ISR-background events are normalised to the number of selected events in data according to equation 6.2. 74

6.6 The composition of the generated event sample according to the simulation normalised to the number of selected events in the data. 75

6.7 The composition of the selected signal events is listed. The numbers are not normalised to the number of events in the data. 75

6.8 The composition of the selected ISR-background events is listed. The numbers are not normalised to the number of events in the data. 75

6.9 B hadrons and charmed hadrons and their masses and lifetimes [22]. c, denotes the light-speed. 77

6.10 N_{bkg}^{gen}(before), is the number of generated background events that are analysed for the listed processes. $N_{bkg}^{gen,t}$(after), is the number of generated background events that remain after the selection is carried out described in section 6.1 and the additional selection criterion, $D_{threshold} \geq 2.3$, is applied. ε_{bkg}^{t}, is the selection efficiency calculated from N_{bkg}^{gen}(before) and $N_{bkg}^{gen,t}$(after) according to equation 6.5. 82

6.11 N_{signal}^{gen}(before), is the number of generated signal events that are analysed. $N_{ISR}^{gen,t}$(after), is the number of generated ISR-background events that remain after the selection is carried out described in section 6.1 ε_{ISR}^{t}, is the selection efficiency calculated from N_{signal}^{gen}(before) and $N_{ISR}^{gen,t}$(after) according to equation 6.5. 83

6.12 Numbers of tagged high energy events selected from the data and the expected numbers of tagged generated events for the different centre–of–mass energies. The number of tagged events expected is normalised to the number of selected events in data according to equation 6.2. 83

6.13 The numbers of tagged selected events, tagged background events and tagged ISR-background events are listed. The number of tagged background and tagged ISR-background events are normalised to the number of tagged events in data according to equation 6.2. 83

6.14 The composition of the tagged generated event sample according to the simulation normalised to the number of selected events in the data.. . . . 84

6.15 The composition of tagged selected signal events is listed. The numbers are not normalised to the number of events in the data. 86

6.16 The composition of ISR-background events is listed. The numbers are not normalised to the number of events in the data. 86

7.1 The numbers of selected events in data, N_{sel}, generated background events, N_{bkg}, generated ISR-background events, N_{ISR}, and the total efficiency, ε, are listed. The background events and ISR-background events are normalised to the data by the integrated luminosity. 88
7.2 The selection efficiency with the total error derived from generated signal events. 89
7.3 The number of events with TEC trigger information, energy trigger information and with TEC trigger and energy trigger information. The last column contains the trigger efficiencies for trigger level-1 with statistical uncertainties. 90
7.4 Systematic uncertainty contributions from the investigated sources. The uncertainties of each individual source are added in quadrature and form the total systematic uncertainty of σ_{had}. 92
7.5 The results of the measurement of the hadronic cross section compared to the combined LEP measurements, σ_{had}^{LEP}, and the Standard Model prediction, σ_{had}^{SM}. The quoted uncertainties on the combined LEP measurements contain the statistical and the systematic uncertainties added in quadrature. The Standard Model prediction is calculated with ZFITTER V6.35 [43] taking into account QCD and QED corrections and weak corrections. The ZFITTER flags for the final state radiation and initial-final state radiation interference, FINR=0 and INTF=0, are set to zero according to the LEP Electroweak Working Group (LEPEWWG) for the treatment of hadronic final states [47]. 93

8.1 The numbers of tagged data events, tagged background events and tagged ISR-background events. 96
8.2 The numbers of selected events, background events, ISR-background events are listed. The number of background and ISR-background events are normalised to the number of selected events in data according to equation 6.2. 97
8.3 The tagging efficiencies for bottom, charm and the combined light quark events and their statistical uncertainties are listed. 98
8.4 The modelling parameters to simulate signal events. 101
8.5 The systematic uncertainties resulting from the quark modelling. The numbers are the corresponding deviations from the measured value and the positive(negative) sign indicates the correlation(anti-correlation) between the parameter and R_b. 106
8.6 The systematic uncertainties of the investigated sources. 107
8.7 The coefficients $a(R_c)$ and the corresponding values for R_c^{SM} calculated by ZFITTER V6.35 taking into account QED corrections, QCD corrections and weak corrections. The ZFITTER flags for the final state radiation and initial-final state radiation interference are set to FINR=0 and INTF=1. The therotical uncertainty on R_c^{SM} is obtained by varying the input parameters by their quoted uncertainties as listed in section 2.7. 107

8.8 The results of the measurement of R_b compared to the combined LEP measurements, $R_b{}^{LEP}$, and the Standard Model prediction, R_b^{SM}. The quoted uncertainties on the combined LEP measurements contain the statistical and the systematic uncertainties added in quadrature. The Standard Model predictions are calculated with ZFITTER V6.35 [43] taking into account QED corrections, QCD corrections and weak corrections. The ZFITTER flags for the final state radiation and initial-final state radiation interference are set to FINR=0 and INTF=1. The theoretical uncertainties as quoted for σ_{had} due to the variation of the input parameters as discussed in section 2.7 are much smaller than the Standard Model prediction of R_b and basically caused by the large uncertainty on the mass of the Standard Model Higgs boson. 108

9.1 The input parameters from the Z-resonance measured at L3. The mass of the Z boson, m_Z, the total width of the Z boson, Γ_Z, determines the width of the Z-resonance the total hadronic cross section, σ^0_{had}, the ratio of the hadronic and the leptonic branching fractions of the Z boson, R^0_l, and the total leptonic forward-backward asymmetry, $A^{0,l}_{fb}$ [75]. The correlation matrix is listed in section C in Table C.1. 111

9.2 The results of σ^{tot}_{had}, R_b and A^b_{fb} used in the χ^2-fit. The measurements are performed at L3 [72, 73, 76–79]. 112

9.3 The results of the free parameters obtained from the fit to the L3 measurements. The Standard Model predictions are calculated with ZFITTER V6.35 taking into account QED corrections, QCD corrections and weak corrections. The correlation matrix is listed in section C in Table C.2. . . . 113

9.4 The results for left- and right-handed couplings of the Z boson extracted from the fit to the L3 measurements compared to the Standard Model predictions calculated with ZFITTER V6.35 [43]. 113

9.5 The input parameters from the Z-resonance from combined LEP measurements [47]. The correlation matrix is listed in section C in Table C.3. . . . 115

9.6 Additional input parameters measured at the Z-resonance from LEP I and SLD measurements [47]. The correlation matrix is listed in section C in Table C.4. 115

9.7 The results of the free parameters obtained from the fit to the LEP I and SLD measurements. The Standard Model predictions are calculated with ZFITTER V6.35 taking into account QED corrections, QCD corrections and weak corrections [47]. The correlation matrix is listed in section C in Table C.5. 116

9.8 The results for left- and right-handed couplings of the Z boson extracted from the fit to the LEP I and SLD measurements and listed together with the Standard Model predictions. 116

9.9 The parameters η_{ik} $(i, k = L, R)$ define to which helicity amplitudes the contact interactions contribute and hence determine the model. 118

9.10 The lower limits of Λ_- and Λ_+ in TeV at 95% confidence level. The first column contains the limits obtained from the hadronic cross section measured at L3. The second column contains the limits achieved from the $b\bar{b}$ cross section measurement at L3 only. The first column contains the limits in TeV obtained from the hadronic cross section and $b\bar{b}$ cross section measured at L3. The fourth column contains the limits in TeV achieved from the combined LEP measurements of the $b\bar{b}$ cross section [22]. Λ_- and Λ_+ refer to a destructive and constructive interference with the Standard Model, respectively. They correspond to the upper and lower signs of η_{ik} in Table 9.9. 119
9.11 The upper limits at 95% confidence level of the quark radius obtained from a fit to hadronic cross section measurements of L3 and the LEP combined analyses. 120
9.12 The lower limits of the Z′ mass for the χ, ψ, η and LR model at 95% confidence level achieved from a fit to the L3 measurements with R_b and the combined LEP measurements, respectively. Note that the lower limits on $m_{Z'}^{limit}$(LEP) are obtained for a mixing angle θ_M fixed to zero (see also [81]). 121
9.13 The lower limits of the mass scale M_s at 95% confidence level obtained from a fit to hadronic cross section measurements of L3 and the LEP combined analyses. 121

10.1 The measured hadronic cross sections, σ_{had}. 123
10.2 The measurement of R_b for the corresponding centre–of–mass energies. . . 123
10.3 The comparison with the Standard Model prediction of the vector and axial-vector couplings and the left- and right-handed couplings obtained from the fit to the L3 measurements and to the combined LEP measurements, respectively. 124
10.4 The lower limits of Λ_- and Λ_+ at 95% confidence level [82]. 126
10.5 The upper limits on the radius of the quarks at 95% confidence level obtained from a fit to hadronic cross section measurements of L3 and the LEP combined analyses and the upper limit on the radius of the bottom quarks from L3 measurements. 126
10.6 The lower limits of the Z′ mass for the χ, ψ, η and LR model at 95% confidence level achieved from a fit to the L3 measurements. 126
10.7 The lower limits of the mass scale M_s at 95% confidence level obtained from a fit to hadronic cross section measurements of L3 and the LEP combined analyses. 126

B.1 The comparison of the efficiency calculation and its standard deviation according to the binomial probability distribution and the standard way. . 130

C.1 The correlations between the five input parameters from the L3 measurements presented in Table 9.1. 131

C.2 The correlations between the free parameters of the fit to the L3 measurements. 131
C.3 The correlations between the five input parameters from combined LEP measurements and SLD measurements as presented in Table 9.5. 132
C.4 The correlations between the combined LEP measurements and SLD measurements used in the fit. 132
C.5 The correlations between the free parameters of the fit to the combined LEP measurements and SLD measurements. 132

Chapter 1

Introduction

In all the vast variety of our world, everything is build up from a set of fundamental constituents. These constituents are bound tightly together by fundamental forces, forming atoms and finally moulding us and the matter that surrounds us. The fundamental constituents of matter are called fermions (spin-$\frac{1}{2}$ particles). The fermions split up in leptons and quarks. The quarks form atomic nuclei. The fermions are bound by fundamental forces. Four fundamental forces are known, acting between the fermions. The four fundamental forces are the electromagnetic force, the weak force, the strong force and gravitation. The electromagnetic force describes the behaviour of electrically charged particles in electric and magnetic fields. The weak force causes radioactivity and drives the nuclear processes in our sun. The strong force describes the interaction of quarks and gravitation describes the mutual attraction of massive objects.
After decades of studies, it turned out that a minimal theory is able to describe the electromagnetic, weak and strong interactions. This theory is referred to as the Standard Model of elementary particle physics [1–4]. The Standard Model is based on the idea of keeping certain features of fermions conserved in spacetime. The electromagnetic, the weak and the strong force are mediated by bosons (spin-1 particles). Gravitation is not described in this way. The electromagnetic and the weak force are unified and known as the electroweak interaction. This interaction is mediated by four bosons, the Z, $W^{\pm}$ and the photon. It is widely believed that all forces are of the same strength at a very large energy scale ($\approx 10^{19}$GeV). The theory describing the four forces at the same time is called Grand Unified Theory (GUT). It would unify the Standard Model and gravitation and furthermore open a wide field of predictions on yet undiscovered particles and forces.
The exploration of particles and their interactions means to travel back in time to the beginning of our universe. This enables us to understand the world as seen by us. The conditions in the early universe are simulated in particle accelerators. One of them is the Large Electron Positron Collider (LEP) at the European Centre for Particle Physics (CERN) near Geneva.
In the last decade, Standard Model predictions were tested and basically confirmed at LEP at centre–of–mass energies from 89 GeV up to 210 GeV. One possibility to probe the Standard Model is to test the couplings of the bosons to the fermions, in particular

the vector and axial vector couplings of the Z boson to the heaviest quark, the bottom quark. The vector and axial vector couplings of the Z boson to the quarks are of particular interest because they are relatively poorly known in comparison to the couplings to the leptons. The bottom quark is the heaviest quark flavour that can be produced in pairs at LEP. The measurement of a set of parameters sensitive to the couplings of the Z boson to the bottom quark will enable us to probe the couplings predicted by the Standard Model. Nevertheless, open questions remain and deviations from the Standard Model predictions might be caused by new phenomena in elementary particle physics. Hence, it is desirable to probe the Standard Model at higher energies. Possible extensions of the Standard Model towards a GUT will reveal its deeper structure and hence lead to a deeper understanding of the laws of nature and our universe. The extensions of the Standard Model that will be discussed are in particular four-fermion contact interactions, the existence of more fundamental forces in terms of an extra heavy boson, Z', the spatial extension of the nominally 'point-like' fermions and the exchange of gravitons as the mediator of gravitation.
Hence, this work is devoted to the study of the vector and axial vector couplings of the Z boson to the bottom quark to probe the Standard Model and to search for new phenomena in elementary particle physics beyond the Standard Model.

Chapter 2

Theory

The Theory to describe elementary particles and their interactions is based on the fundamental idea of local gauge invariance [5]. The particles and forces, acting between them, are the constituents of the matter surrounding us. The particles, the basic principles of their interaction and the observables measured in experiment are described in further detail in this chapter.

2.1 Quantum Field Theory and Gauge Invariance

In general fermions are described by complex matter fields $\psi(\mathrm{x})$ depending on the space-time coordinate x. The kinematic behaviour and the interaction between different fermions is described by the Lagrangian:

$$\mathcal{L}(\psi, \partial_\mu \psi). \tag{2.1}$$

The Lagrangian contains the fields $\psi(\mathrm{x})$ and their partial derivatives $\partial_\mu \psi$. The equations of motion of the fermions are derived from the Lagrangian.
The local gauge transformation

$$\psi(\mathrm{x}) \rightarrow \psi'(\mathrm{x}) = \mathrm{U}(\mathrm{x})\psi(\mathrm{x}), \tag{2.2}$$

of the fermion fields reveals a certain symmetry of the theory, if the equations of motion remain invariant. The transformations $\mathrm{U}(\mathrm{x})$ are expressed as:

$$\mathrm{U}(\mathrm{x}) = \exp\left[-\mathrm{i}\sum_{\mathrm{j}=1}^{\mathrm{n}} \theta_{\mathrm{j}}(\mathrm{x})\mathrm{T}_{\mathrm{j}}\right], \tag{2.3}$$

where $\theta_{\mathrm{j}}(\mathrm{x})$ are real functions specifying the local transformation and T_{j} are the n generators of the underlying Lie algebra and obey:

$$[\mathrm{T}_{\mathrm{j}}, \mathrm{T}_{\mathrm{k}}] = \mathrm{T}_{\mathrm{j}}\mathrm{T}_{\mathrm{k}} - \mathrm{T}_{\mathrm{k}}\mathrm{T}_{\mathrm{j}} = \mathrm{i}\sum_{\mathrm{l}=1}^{\mathrm{n}} \mathrm{f}_{\mathrm{jkl}}\mathrm{T}_{\mathrm{l}}, \tag{2.4}$$

where f_{jkl} are the structure constants of the Lie algebra. They are totally antisymmetric and vanish if the group is abelian.
The Lagrangian, and hence the equations of motion are invariant under local gauge transformation, if one introduces a covariant derivative, $\mathcal{D}_\mu$, that transforms according to:

$$\mathcal{D}'_\mu = U\mathcal{D}_\mu U^\dagger. \tag{2.5}$$

The covariant derivative is formed by adding terms to the partial derivative:

$$\mathcal{D}_\mu = \partial_\mu + ig\sum_{j=1}^{n} T_j A^j_\mu(x). \tag{2.6}$$

The n fields $A^j_\mu(x), j = 1, \ldots, n$, are gauge fields. They couple to the fermion fields with coupling strength, g. Thus the interactions between the formerly free fermions are introduced. The value of g is not predicted by the theory. The gauge fields $A^j_\mu(x)$ transform under the same local gauge transformation U(x) like:

$$A^j_\mu(x) \to A^{j'}_\mu(x) = A^j_\mu(x) - \frac{1}{g}\partial_\mu\theta_j(x) - \sum_{k,l}^{n} f_{jkl}\theta_k(x)A^l_\mu(x). \tag{2.7}$$

The particles corresponding to the matter fields and the gauge fields are called fermions and gauge bosons, respectively. The gauge bosons, the carriers of forces, are added to the lagrangian in equation 2.1. In non-abelian gauge theories they also interact between each other.

2.2 The Standard Model

The Standard Model of elementary particles is based on the invariance of the Lagrangian under local gauge transformations. The electroweak Standard Model, established by Glashow, Salam and Weinberg [1–3], is a gauge theory which unifies the electromagnetic force described by Quantum Electrodynamics (QED) and the weak force. In the case of the electroweak interactions the equations of motion must be invariant under transformations of the $SU(2)_L \otimes U(1)_Y$ symmetry group of the weak iso-spin and the weak hypercharge, respectively. The three fields $\vec{W}_\mu = (W^1_\mu, W^2_\mu, W^3_\mu)$ are the generators of the weak iso-spin and B_μ denotes the generator of the weak hypercharge. The fermion fields $\psi(x)$ are expressed as the sum of fermion states of definite chirality, called left-handed and right-handed. These components are obtained, applying left- and right-handed projection operators, to the fermion fields:

$$\psi = \psi_L + \psi_R \quad \psi_L = \frac{1-\gamma_5}{2}\psi \quad \psi_R = \frac{1+\gamma_5}{2}\psi. \tag{2.8}$$

The projection operators contain the Dirac matrix γ_5. The transformations according to the $SU(2)_L$ group affect only the left-handed parts of the fermion fields. The left-handed fermions form iso-spin doublets and the right-handed fermions iso-spin singlets.

The fermions carry quantum numbers of the weak iso-spin $\vec{\mathrm{T}} = (\mathrm{T}_1, \mathrm{T}_2, \mathrm{T}_3)$ and the weak hypercharge Y. The electromagnetic charge Q is given by the Gell-Mann-Nishijima relation, which is the sum of the third component of the weak iso-spin, T_3, and the weak hypercharge, Y:

$$\mathrm{Q} = \mathrm{T}_3 + \mathrm{Y}. \tag{2.9}$$

The Lagrangian of the electroweak theory is given by:

$$\mathcal{L}_{\mathrm{EW}} = \mathcal{L}_{\mathrm{Fermion}} + \mathcal{L}_{\mathrm{Yang-Mills}} + \mathcal{L}_{\mathrm{Higgs}} + \mathcal{L}_{\mathrm{Yukawa}} \tag{2.10}$$

The covariant derivative for the left-handed and right-handed fermions is:

$$\begin{aligned} \mathrm{left-handed}: \quad \mathcal{D}_\mu^{\mathrm{L}} &= \partial_\mu + \mathrm{i}g_1 \mathrm{Y} \mathrm{B}_\mu + \mathrm{i}g_2 \sum_{\mathrm{j}=1}^{3} \mathrm{T_j} \mathrm{W}_\mu^{\mathrm{j}} \\ \mathrm{right-handed}: \quad \mathcal{D}_\mu^{\mathrm{R}} &= \partial_\mu + \mathrm{i}g_1 \mathrm{Y} \mathrm{B}_\mu, \end{aligned} \tag{2.11}$$

according to section 2.1. The coupling constants, g_1 and g_2, denote the different coupling strengths of the gauge bosons to the fermion fields.
The generators of the $\mathrm{SU(2)_L}$ group are the Pauli matrices. The fermionic part of the Lagrangian, $\mathcal{L}_{\mathrm{Fermion}}$, describes the dynamics of fermions and their interactions with the gauge fields via the covariant derivative as given above:

$$\mathcal{L}_{\mathrm{Fermion}} = \sum_{\psi_{\mathrm{L}}} \bar{\psi}_{\mathrm{L}} \mathrm{i} \gamma_\mu \mathcal{D}_\mu^{\mathrm{L}} \psi_{\mathrm{L}} + \sum_{\psi_{\mathrm{R}}} \bar{\psi}_{\mathrm{R}} \mathrm{i} \gamma_\mu \mathcal{D}_\mu^{\mathrm{R}} \psi_{\mathrm{R}}. \tag{2.12}$$

The matrices γ_μ are the Dirac matrices. $\mathcal{L}_{\mathrm{Yang-Mills}}$ describes the dynamics of the gauge bosons and possible interactions between them

$$\mathcal{L}_{\mathrm{Yang-Mills}} = -\frac{1}{4} \vec{\mathrm{W}}_{\mu\nu} \vec{\mathrm{W}}^{\mu\nu} - \frac{1}{4} \mathrm{B}_{\mu\nu} \mathrm{B}^{\mu\nu} \tag{2.13}$$

$$\vec{\mathrm{W}}_{\mu\nu} = \partial_\mu \vec{\mathrm{W}}_\nu - \partial_\nu \vec{\mathrm{W}}_\mu - g_2 \vec{\mathrm{W}}_\mu \times \vec{\mathrm{W}}_\nu \tag{2.14}$$

$$\mathrm{B}_{\mu\nu} = \partial_\mu \mathrm{B}_\nu - \partial_\nu \mathrm{B}_\mu. \tag{2.15}$$

$\mathcal{L}_{\mathrm{Higgs}}$ [6] describes the dynamics of the Higgs boson:

$$\mathcal{L}_{\mathrm{Higgs}} = (\mathcal{D}_\mu \Phi)^+ (\mathcal{D}^\mu \Phi) + \mathrm{V}(\Phi) \tag{2.16}$$

$$\mathrm{V}(\Phi) = -\mu^2 \Phi^+ \Phi + \frac{\lambda}{4} (\Phi^+ \Phi)^2 \tag{2.17}$$

The Higgs field self-interaction $\mathrm{V}(\Phi)$ is constructed in such a way that it has a non-vanishing **V**acuum **E**xpectation **V**alue (VEV) v, related to the coefficients of the potential $\mathrm{V}(\Phi)$ by:

$$\mathrm{v} = \frac{2\lambda}{\sqrt{\mu}}. \tag{2.18}$$

In the unitary gauge the Higgs field has the simple form:

$$\Phi(\mathrm{x}) = \frac{1}{\sqrt{2}}\begin{pmatrix} 0 \\ \mathrm{v} + \mathrm{H}(\mathrm{x}) \end{pmatrix}, \tag{2.19}$$

where H(x) the field of a neutral spin-0 particle, the Higgs boson. The introduction of the Higgs boson is due to a spontaneous symmetry breaking of a symmetry group of higher dimensionality down to the observed $\mathrm{SU(2)_L} \otimes \mathrm{U(1)_Y}$ structure [7]. A local gauge transformation, that does not leave the ground state of a transformed field invariant, can be solved by introducing a spin-0 particle. The gauge fields $\vec{\mathrm{W}}_\mu$ and B_μ transform in a way that the unphysical transformation fields vanish from the Lagrangian. This is called Higgs-mechanism. The Higgs-mechanism provides masses to the fermions and the gauge bosons, because $\mathrm{v} \neq 0$. The fermion masses are given in $\mathcal{L}_{\mathrm{Yukawa}}$ by:

$$\mathcal{L}_{\mathrm{Yukawa}} = -\sum_{\mathrm{f}} \frac{\mathrm{g_f v}}{\sqrt{2}} \bar{\psi}_{\mathrm{f}} \psi_{\mathrm{f}} - \sum_{\mathrm{f}} \frac{\mathrm{g_f}}{\sqrt{2}} \bar{\psi}_{\mathrm{f}} \psi_{\mathrm{f}} \mathrm{H}, \tag{2.20}$$

where the Yukawa couplings $\mathrm{g_f} = \sqrt{2}\mathrm{m_f}/\mathrm{v}$ depend on the fermion masses and are not predicted by the Standard Model. The second sum in $\mathcal{L}_{\mathrm{Yukawa}}$ describes the interaction of massive fermions and the Higgs boson with coupling constants proportional to the fermion masses. A detailed study of the search for the Standard Model Higgs boson can be found elsewhere [8].
Due to $\mathcal{L}_{\mathrm{Higgs}}$, mixed terms of W^3_μ and B_μ appear in the Lagrangian. They can be disentangled by a rotation in Hilbert space leaving a massive and a massless physical state Z_μ and A_μ, respectively. The massless state A_μ is identified to be the photon, the carrier of the electromagnetic force. The mass eigenstates of the gauge bosons Z_μ, $\mathrm{W}^\pm_\mu$ and A_μ are given as:

$$\begin{aligned} \mathrm{W}^\pm_\mu &= \frac{1}{\sqrt{2}}[\mathrm{W}^1_\mu \mp \mathrm{i}\mathrm{W}^2_\mu] \\ \mathrm{Z}_\mu &= -\sin\theta_{\mathrm{W}}\mathrm{B}_\mu + \cos\theta_{\mathrm{W}}\mathrm{W}^3_\mu \\ \mathrm{A}_\mu &= \cos\theta_{\mathrm{W}}\mathrm{B}_\mu + \sin\theta_{\mathrm{W}}\mathrm{W}^3_\mu. \end{aligned} \tag{2.21}$$

The rotation angle is the electroweak mixing angle θ_{W}, a fundamental parameter of the Standard Model. $\mathrm{W}^\pm_\mu$ and Z_μ are the massive gauge bosons of the electroweak Standard Model. The masses of $\mathrm{W}^\pm_\mu$ and Z_μ are related by:

$$\rho = \frac{\mathrm{m_W^2}}{\mathrm{m_Z^2}\cos^2\theta_{\mathrm{W}}} = 1. \tag{2.22}$$

The ρ-parameter is 1 only at Born level [9]. The electroweak mixing angle θ_{W} depends on the couplings $\mathrm{g_1}$ and $\mathrm{g_2}$:

$$\mathrm{e} = \frac{\mathrm{g_1 g_2}}{\sqrt{\mathrm{g_1^2} + \mathrm{g_2^2}}} = \mathrm{g_1}\cos\theta_{\mathrm{W}} = \mathrm{g_2}\sin\theta_{\mathrm{W}}, \tag{2.23}$$

where e denotes the electric fundamental charge. It is related to the electromagnetic coupling constant $\alpha = e^2/4\pi$ which will be used further on. The masses and the electroweak mixing angle are not predicted by the Standard Model and have to be determined by experiment.
Hence, the fermion Lagrangian can be expressed in terms of the kinetic part of the fermion fields containing again the partial derivative, ∂_μ, and the interaction terms describing the coupling of the particle currents to the gauge bosons via the corresponding coupling constants:

$$\begin{aligned}\mathcal{L}_{\text{Fermion}} &= \bar{\psi} i \gamma_\mu \partial_\mu \psi \\ &- \frac{g_1 g_2}{\sqrt{g_1^2 + g_2^2}} A_\mu J^\mu_{\text{EM}} \\ &- \sqrt{g_1^2 + g_2^2} Z_\mu J^\mu_{\text{NC}} \\ &- \frac{g_2}{\sqrt{2}} (W^+_\mu J^{\mu+}_{\text{CC}} + W^-_\mu J^{\mu-}_{\text{CC}}).\end{aligned} \tag{2.24}$$

The terms J^μ_{EM}, J^μ_{NC} and $J^{\mu\pm}_{\text{CC}}$ are the electromagnetic, the weak neutral and the weak charged current, respectively. They can be written as:

$$J^\mu_{\text{EM}} = \bar{\psi} \gamma_\mu (\mathbf{T_3} + \mathbf{Y}) \psi \tag{2.25}$$
$$J^\mu_{\text{NC}} = \bar{\psi} \gamma_\mu \mathbf{T_3} \psi - \sin^2\theta_{\text{W}} J^\mu_{\text{EM}} \tag{2.26}$$
$$J^{\mu\pm}_{\text{CC}} = \bar{\psi} \gamma_\mu (\mathbf{T_1} \pm i\mathbf{T_2}) \psi. \tag{2.27}$$

Here, $\mathbf{T_{1,2,3}}$ and $\mathbf{Y}$ are matrices of the dimension of the fermion fields. As in the one-dimensional case, $\mathbf{T_3}$ and $\mathbf{Y}$ are related by equation 2.9. For a specific fermion pairing the currents are given by:

$$J^\mu_{\text{EM}} = Q_{\text{f}} \bar{f} \gamma_\mu f \tag{2.28}$$
$$J^\mu_{\text{NC}} = \frac{1}{2} \bar{f} \gamma_\mu (g^{\text{f}}_{\text{V}} - g^{\text{f}}_{\text{A}} \gamma_5) f \tag{2.29}$$
$$J^{\mu\pm}_{\text{CC}} = \frac{1}{2} \bar{f} \gamma_\mu (1 - \gamma_5) f. \tag{2.30}$$

g^{f}_{V} and g^{f}_{A} are the vector and axial vector couplings, respectively. They are given as:

$$g^{\text{f}}_{\text{V}} = T^{\text{f}}_3 - 2Q_{\text{f}} \sin^2\theta_{\text{W}} \tag{2.31}$$
$$g^{\text{f}}_{\text{A}} = T^{\text{f}}_3. \tag{2.32}$$

In the limit of massless fermions, i.e. unbroken SU(2)_{L} symmetry, only left-handed fermions couple to the $W^\pm$ bosons. The charged current interactions can be decomposed in two parts of equal strength with transformation properties of a vector and an axial vector, respectively. This is known as the V-A structure of weak interactions. The weak neutral current is a linear superposition of the SU(2)_{L} and U(1)_{Y} generators. The contributions of the vector and axial vector parts are different in their relative strength.

The difference denoted by the vector and axial vector couplings g_V and g_A, reflects the admixture of the $U(1)_Y$ generator B_μ. In the Standard Model these coupling constants are universal for all fermions of a given electric charge, Q_f. The relative couplings of the Z to the left- and right-handed fermions, g_L and g_R, are given by:

$$g_L^f = \frac{1}{2}(g_V^f + g_A^f) = T_3^f - Q_f \sin^2\theta_W \tag{2.33}$$

$$g_R^f = \frac{1}{2}(g_V^f - g_A^f) = -Q_f \sin^2\theta_W. \tag{2.34}$$

The strong interactions are described by the theory of Quantum Chromodynamics (QCD). In QCD the equations of motion are invariant under transformations of the $SU(3)_C$ symmetry group, introducing an extra charge called colour charge. The strong force couples with equal strength to left- and right-handed fermions that carry a colour charge. They are called quarks. The covariant derivative is expressed as:

$$\mathcal{D}_\mu = \partial_\mu + ig_3 \sum_{a=1}^{8} \frac{\lambda_a}{2} G_\mu^a. \tag{2.35}$$

The gauge bosons G_μ^a, $a = 1, \ldots, 8$ are the massless gluons of QCD. The coupling constant, g_3, describes the coupling strength of the gluons to the quarks. It corresponds to the coupling constants, g_1 and g_2 described earlier and is related to the strong coupling constant, $\alpha_s = g_3^2/4\pi$.
The generators of the $SU(3)_C$ group, λ_a, are the Gell-Mann matrices [10]. In the current understanding of elementary particle physics, fermions are the fundamental building blocks of matter. The fermions are subdivided into leptons and quarks. All fundamental fermions are point-like objects, which is verified down to distances of $\mathcal{O}(10^{-17}$ cm) [11]. For each fermion exists an anti-particle with the same mass but opposite electric charge and colour charge. The Standard Model does not predict the number of generations. The down type quarks (d′, s′, b′) denote the eigenstates of the weak interactions. They are obtained by a unitary transformation V_{CKM}, the Cabbibo-Kobayashi-Maskawa mixing matrix [12], from the mass eigenstates.

$$\begin{pmatrix} d' \\ s' \\ b' \end{pmatrix} = V_{CKM} \begin{pmatrix} d \\ s \\ b \end{pmatrix} \tag{2.36}$$

In the general case of massive neutrinos there will be a unitary mixing matrix relating weak and mass eigenstates of the leptons as for the quarks. The fermions and the gauge bosons are listed in Table 2.1 and Table 2.2 together with their corresponding quantum numbers.

fermion generation I	II	III	T	T_3	Y	Q	C
leptons							
$\begin{pmatrix}\nu_e\\ e\end{pmatrix}_L$	$\begin{pmatrix}\nu_\mu\\ \mu\end{pmatrix}_L$	$\begin{pmatrix}\nu_\tau\\ \tau\end{pmatrix}_L$	$\begin{pmatrix}+\frac{1}{2}\\ +\frac{1}{2}\end{pmatrix}$	$\begin{pmatrix}+\frac{1}{2}\\ -\frac{1}{2}\end{pmatrix}$	$\begin{pmatrix}-\frac{1}{2}\\ -\frac{1}{2}\end{pmatrix}$	$\begin{pmatrix}0\\ -1\end{pmatrix}$	$\begin{pmatrix}0\\ 0\end{pmatrix}$
e_R	μ_R	τ_R	0	0	-1	-1	0
quarks							
$\begin{pmatrix}u\\ d'\end{pmatrix}_L$	$\begin{pmatrix}c\\ s'\end{pmatrix}_L$	$\begin{pmatrix}t\\ b'\end{pmatrix}_L$	$\begin{pmatrix}+\frac{1}{2}\\ +\frac{1}{2}\end{pmatrix}$	$\begin{pmatrix}+\frac{1}{2}\\ -\frac{1}{2}\end{pmatrix}$	$\begin{pmatrix}+\frac{1}{6}\\ +\frac{1}{6}\end{pmatrix}$	$\begin{pmatrix}+\frac{2}{3}\\ -\frac{1}{3}\end{pmatrix}$	$\begin{pmatrix}r,g,b\\ r,g,b\end{pmatrix}$
u_R	c_R	t_R	0	0	$+\frac{2}{3}$	$+\frac{2}{3}$	r,g,b
d'_R	s'_R	b'_R	0	0	$-\frac{1}{3}$	$-\frac{1}{3}$	r,g,b

Table 2.1: The fundamental fermions are listed separately as leptons and quarks considering neutrinos as massless. The left-handed fermions are grouped to iso-spin doublets indicated with L. The right-handed fermions are iso-spin singlets indicated with R. The fermions are characterised by their quantum numbers of the weak iso-spin T and its third component T_3, their weak hypercharge Y, their electric charge Q and their colour charge C.

gauge boson	Q	C
γ	0	0
Z	0	0
$W^\pm$	±1	0
G^a	0	yes

Table 2.2: The electric charge Q and the colour charge C of the gauge bosons. The index a corresponds to the colour charge of the corresponding gluon.

2.3 Hadronization

QCD predicts the existence of only colourless objects in nature. Hence, particles that carry a colour charge appear only in colourless bound states. This characteristic is called confinement.
Quarks in contrast to leptons do participate in strong interactions. After the production of a quark pair, gluons are radiated by the quarks that themself produce gluon pairs or quark pairs. This is called parton shower. Due to the confinement, the quarks hadronize and form colourless bound states, called hadrons. The hadrons exist in two classes:

- **Mesons:** quark content, $q\bar{q}$
- **Baryons:** quark content, qqq

The formation of colourless objects from a quark in a scattering process is called hadronization or fragmentation. The hadronization/fragmentation process is shown in Figure 2.1. The hadronization of quarks is not described by the Standard Model. The existing models

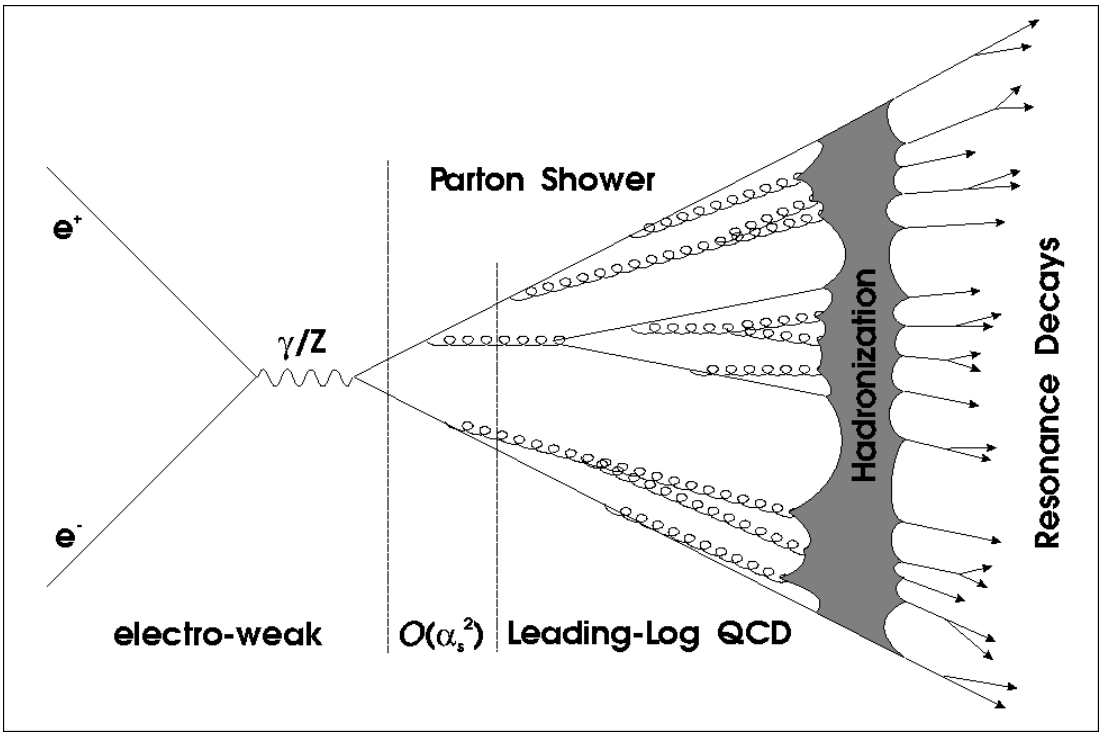

Figure 2.1: The hadronization process as described in the text. After the production of a quark pair, the parton shower is produced and the hadronization starts. The heavy and unstable hadrons resulting from the hadronization decay to stable hadrons like pions and kaons and leptons like electrons and muons and real photons.

are obtained empirically, based on measurements from different experiments. Two models are: string fragmentation [13, 14] and cluster fragmentation [15–18]. The string fragmentation scheme considers the colour field between the partons, i.e., quarks and gluons, to

be the fragmenting entity rather than the partons themselves. The string can be viewed as a colour flux tube formed by gluon self-interaction as two coloured partons move apart. When the energy in the string is sufficient, a quark pair is created from the vacuum. Thus the string breaks up repeatedly into colour singlet systems as long as the invariant mass of the string pieces exceed the on-shell mass of a hadron.
In cluster fragmentation the remaining gluons at the end of the parton shower evolution are split into quark-anti-quark pairs. Colour singlet clusters of masses of a few GeV are then formed from the quark and anti-quark of colour-connected splittings. These clusters decay directly into two hadrons unless they are either too heavy, then they decay into two clusters, or too light, in which case a cluster decays into a single hadron.
Hadrons containing heavy quarks retain a larger fraction of energy and momentum of the primordial heavy quark than lighter flavoured hadrons. In order to parametrise the fragmentation, fragmentation functions are introduced. For instance the Peterson fragmentation function [19] and the Kartvelishvili fragmentation function [20]:

$$\begin{aligned} \text{Peterson } \textit{et al.} \quad &: \quad \mathrm{f_P(z)} \propto \frac{1}{\mathrm{z}}\Big(1 - \frac{1}{\mathrm{z}} - \frac{\epsilon}{1-\mathrm{z}}\Big)^{-2} \\ \text{Kartvelishvili } \textit{et al.} \quad &: \quad \mathrm{f_K(z)} \propto \mathrm{z}^{\alpha}(1-\mathrm{z}), \end{aligned} \tag{2.37}$$

where the parameters ϵ and α depend on the heavy hadron. The variable z is given by:

$$\mathrm{z} = \frac{(\mathrm{E} + \mathrm{p}_{\parallel})_{\mathrm{hadron}}}{(\mathrm{E} + \mathrm{p}_{\parallel})_{\mathrm{quark}}}. \tag{2.38}$$

$\mathrm{p}_{\parallel}$ is the momentum component parallel to the direction of the fragmenting quark. The fragmentation of heavy quarks such as bottom and charm quarks is described by the widely used Peterson fragmentation function. In the limit of a very heavy hadron, the fragmentation function is much harder and peaks nearer to one. Unfortunately, as this quantity is not directly accessible, experiments typically use other scaling variables which are close approximations of z. One possibility is the fragmentation parameter, $\mathrm{x_E} = \mathrm{E_{had}}/\mathrm{E_{beam}}$, which approximates the Peterson variable z, but is not identical to it. The average value of the fragmentation parameters for bottom and charm quarks are found to be [21]:

$$\begin{aligned} \langle \mathrm{x_E(b)} \rangle &= 0.702 \pm 0.008 \\ \langle \mathrm{x_E(c)} \rangle &= 0.484 \pm 0.008. \end{aligned} \tag{2.39}$$

The final state bottom quarks form then B hadrons, charm quarks form charmed hadrons and up, down and strange quarks form light hadrons. The full information about hadrons can be found in [22]. A fraction of different B hadrons and charmed hadrons and their characteristics are listed in Table 2.3. These hadrons decay into stable mesons and baryons like pions and kaons and protons and/or leptons like electrons and muons and real photons as introduced in section 2.2. At energies of a few GeV the decay products are equally spread in all directions, whereas at centre–of–mass energies as discussed here, the decay products are boosted in one direction and clustered to jets (see appendix A).

Particle	Mass(MeV/c^2)	$\tau(10^{-12}\mathrm{s})$	c$\tau(\mu\mathrm{m})$
$B^+(u\bar{b})$	5278.9 ± 1.8	1.65 ± 0.04	495
$B^0_d(b\bar{d})$	5279.2 ± 1.8	1.56 ± 0.04	468
$B^0_s(b\bar{s})$	5369.3 ± 2.0	1.54 ± 0.07	462
$D^+(c\bar{d})$	1869.3 ± 0.5	1.057 ± 0.015	317
$D^0(c\bar{u})$	1864.5 ± 0.5	0.415 ± 0.004	124
$D_s(c\bar{s})$	1968.5 ± 0.6	0.447 ± 0.017	134

Table 2.3: B hadrons and charmed hadrons and their masses and lifetimes [22]. The quark content is given in parenthesis. The parameter, c, denotes the light-speed.

2.4 Fermion Pair Production

Electron-positron annihilation into a fermion-anti-fermion pair as derived from the Standard Model Lagrangian (equation 2.24) is described in lowest order by the exchange of a photon and a Z boson, depicted in Figure 2.2.

The differential cross section as a function of the phase space Φ for this scattering process

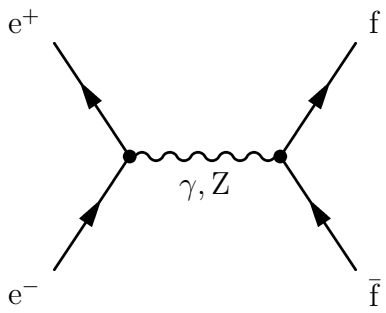

Figure 2.2: The Feynman diagram for electron-positron annihilation and fermion pair production.

is proportional to the square of the absolute value of the corresponding matrix element derived from the Standard Model Lagrangian:

$$\frac{\mathrm{d}\sigma_{\mathrm{f\bar{f}}}}{\mathrm{d}\Phi} \propto |\mathcal{M}|^2 = |\mathcal{M}_\gamma + \mathcal{M}_\mathrm{Z}|^2. \tag{2.40}$$

The matrix elements $\mathcal{M}_\gamma$ and $\mathcal{M}_\mathrm{Z}$ denote the photon and Z boson exchange, respectively. The differential cross section is given by [23]:

$$\frac{\mathrm{d}\sigma_{\mathrm{f\bar{f}}}}{\mathrm{d}\cos\Theta} = \frac{\mathrm{d}\sigma^{\gamma\gamma}_{\mathrm{f\bar{f}}}}{\mathrm{d}\cos\Theta} + \frac{\mathrm{d}\sigma^{\gamma\mathrm{Z}}_{\mathrm{f\bar{f}}}}{\mathrm{d}\cos\Theta} + \frac{\mathrm{d}\sigma^{\mathrm{ZZ}}_{\mathrm{f\bar{f}}}}{\mathrm{d}\cos\Theta} \tag{2.41}$$

$$\frac{\mathrm{d}\sigma_{\mathrm{f\bar{f}}}^{\gamma\gamma}}{\mathrm{d}\cos\Theta} = \mathrm{N_c^f}\frac{\pi\alpha^2}{2\mathrm{s}}\mathrm{Q_e^2Q_f^2}(1+\cos^2\Theta) \tag{2.42}$$

$$\frac{\mathrm{d}\sigma_{\mathrm{f\bar{f}}}^{\gamma\mathrm{Z}}}{\mathrm{d}\cos\Theta} = \mathrm{N_c^f}\frac{\pi\alpha^2}{2\mathrm{s}}\mathrm{Q_eQ_f}[2\mathrm{g_V^e g_V^f}(1+\cos^2\Theta)+4\mathrm{g_A^e g_A^f}\cos\Theta]\mathcal{R}\mathrm{e}\{\chi\} \tag{2.43}$$

$$\begin{aligned}\frac{\mathrm{d}\sigma_{\mathrm{f\bar{f}}}^{\mathrm{ZZ}}}{\mathrm{d}\cos\Theta} &= \mathrm{N_c^f}\frac{\pi\alpha^2}{2\mathrm{s}}([(\mathrm{g_V^e})^2+(\mathrm{g_A^e})^2][(\mathrm{g_V^f})^2+(\mathrm{g_A^f})^2](1+\cos^2\Theta) \\ &+ \mathrm{N_c^f}\frac{\pi\alpha^2}{2\mathrm{s}}8\mathrm{g_V^e g_A^e g_V^f g_A^f}\cos\Theta)|\chi|^2.\end{aligned} \tag{2.44}$$

The integration over $\cos\Theta$ from -1 to 1 provides the total cross section. χ is the propagator of the Z boson:

$$\chi = \frac{1}{4\sin^2\theta_{\mathrm{W}}\cos^2\theta_{\mathrm{W}}}\frac{\mathrm{s}}{\mathrm{s}-\mathrm{m_Z^2}+\mathrm{i}\Gamma_{\mathrm{Z}}\mathrm{m_Z}}. \tag{2.45}$$

$\alpha = \mathrm{e}^2/4\pi$ is the electromagnetic coupling constant and $\mathrm{s} = \mathrm{E_{CM}^2}$ is the squared centre–of–mass energy. $\mathrm{N_c^f}$ is the colour factor arising from QCD; $\mathrm{N_c^f} = 1$ for leptons and $\mathrm{N_c^f} = 3$ for quarks. $\mathrm{m_Z}$ is the mass of the Z boson and Γ_{Z} is the total decay width of the Z boson:

$$\Gamma_{\mathrm{Z}} = \textstyle\sum_{\mathrm{f}}\Gamma_{\mathrm{f\bar{f}}} \quad (\mathrm{m_f} < \mathrm{m_Z}/2) \tag{2.46}$$

$$\Gamma_{\mathrm{f\bar{f}}} = \mathrm{N_c^f}\frac{\alpha\mathrm{m_Z}}{12\sin^2\theta_{\mathrm{W}}\cos^2\theta_{\mathrm{W}}}\left[(\mathrm{g_V^f})^2+(\mathrm{g_A^f})^2\right] \tag{2.47}$$

The terms proportional to $\cos\Theta$ in the differential cross section (see equation 2.43 and 2.44) lead to a difference in the number of fermions scattered in the forward hemisphere and the number of fermions scattered in the backward hemisphere, with respect to the direction of the initial state electron. Thus, the forward-backward asymmetry is defined as:

$$A_{\mathrm{fb}} = \frac{\mathrm{N_f}-\mathrm{N_b}}{\mathrm{N_f}+\mathrm{N_b}} \tag{2.48}$$

with $\mathrm{N_f}$ and $\mathrm{N_b}$ given as:

$$\mathrm{N_f} = \int_0^1 \frac{\mathrm{d}\sigma_{\mathrm{f\bar{f}}}}{\mathrm{d}\cos\Theta}\cdot\mathcal{L}\cdot\varepsilon\cdot\mathrm{d}\cos\Theta \tag{2.49}$$

$$\mathrm{N_b} = \int_{-1}^0 \frac{\mathrm{d}\sigma_{\mathrm{f\bar{f}}}}{\mathrm{d}\cos\Theta}\cdot\mathcal{L}\cdot\varepsilon\cdot\mathrm{d}\cos\Theta, \tag{2.50}$$

where $\mathcal{L}$ is the integrated luminosity and ε is the detection efficiency. At the Z-resonance ($\sqrt{\mathrm{s}} = \mathrm{m_Z}$) for pure Z boson exchange, the forward-backward asymmetries of the different fermion flavours are given by:

$$A_{\mathrm{fb}}^{\mathrm{f}} = \frac{3}{4}\mathcal{A}_{\mathrm{e}}\mathcal{A}_{\mathrm{f}}. \tag{2.51}$$

The coupling parameters, $\mathcal{A}_f$, where the index denotes the fermion flavour, is a function of the vector and axial vector couplings of the corresponding fermion:

$$\mathcal{A}_f = \frac{2g_V^f g_A^f}{\left(g_V^f\right)^2 + \left(g_A^f\right)^2}. \tag{2.52}$$

From the equations 2.42- 2.44, 2.48 and 2.49- 2.50 follows:

$$\frac{1}{\sigma_{f\bar{f}}}\frac{d\sigma_{f\bar{f}}}{d\cos\Theta} = \frac{3}{8}(1+\cos^2\Theta) + A_{fb}^f \cos\Theta. \tag{2.53}$$

An alternative approach is to express the differential cross section as a function of helicity amplitudes corresponding to the left- right-handed nature of the fermions. The differential cross section is then given by:

$$\frac{d\sigma_{f\bar{f}}}{d\cos\Theta} = \frac{N_c}{128\pi s}\sum_{i,k=L,R}\rho_{ik}\left|\mathcal{A}_{ik}^{ef}\right|^2 \tag{2.54}$$

The parameters ρ_{ik} are given by:

$$\rho_{RR} = \rho_{LL} = s^2(1+\cos\Theta)^2 \tag{2.55}$$

$$\rho_{RL} = \rho_{LR} = s^2(1-\cos\Theta)^2. \tag{2.56}$$

The helicity amplitudes are expressed as [11, 24, 25]:

$$\mathcal{A}_{ik}^{ef} = \frac{4\pi\alpha^2}{s}Q_e Q_f + \frac{\pi\alpha^2 g_i^e g_k^f}{\sin^2\theta_W\cos^2\theta_W(s - m_Z^2 + i\Gamma_Z m_Z)}, \tag{2.57}$$

with $g_{i,k} = g_{L,R}$ as given in equation 2.33 and 2.34. The integration over the scattering angle leads to:

$$\sigma_{f\bar{f}} = \frac{N_c}{48\pi s}\left[\left|\mathcal{A}_{RR}^{ef}\right|^2 + \left|\mathcal{A}_{LL}^{ef}\right|^2 + \left|\mathcal{A}_{RL}^{ef}\right|^2 + \left|\mathcal{A}_{LR}^{ef}\right|^2\right]. \tag{2.58}$$

With $\sigma_{ef}^{ij} = N_c/(48\pi s)|A_{ij}^{ef}|^2$, $i,j = L,R$ one finds a set of linearly independent cross sections:

$$\begin{aligned}
\sigma_{f\bar{f}} &= \sigma_{e\bar{f}}^{LL} + \sigma_{e\bar{f}}^{LR} + \sigma_{e\bar{f}}^{RR} + \sigma_{e\bar{f}}^{RL} \\
\sigma_{f\bar{f}}^{pol} &= \sigma_{e\bar{f}}^{LL} - \sigma_{e\bar{f}}^{LR} - \sigma_{e\bar{f}}^{RR} + \sigma_{e\bar{f}}^{RL} \\
\sigma_{f\bar{f}}^{LR} &= \sigma_{e\bar{f}}^{LL} + \sigma_{e\bar{f}}^{LR} - \sigma_{e\bar{f}}^{RR} - \sigma_{e\bar{f}}^{RL} \\
\sigma_{f\bar{f}}^{fb} &= \sigma_{e\bar{f}}^{LL} - \sigma_{e\bar{f}}^{LR} + \sigma_{e\bar{f}}^{RR} - \sigma_{e\bar{f}}^{RL}.
\end{aligned} \tag{2.59}$$

The left-right asymmetry and the forward-backward asymmetry are expressed as the ratio of $\sigma_{f\bar{f}}$ and $\sigma_{f\bar{f}}^{LR}$ and $\sigma_{f\bar{f}}$ and $\sigma_{f\bar{f}}^{fb}$ respectively:

$$A_{LR}^f = \frac{\sigma_{f\bar{f}}^{LR}}{\sigma_{f\bar{f}}} \qquad A_{fb}^f = \frac{3}{4}\frac{\sigma_{f\bar{f}}^{fb}}{\sigma_{f\bar{f}}} \tag{2.60}$$

At $\sqrt{s} = m_Z$ for pure Z boson exchange, the left-right asymmetry is given by:

$$A_{LR}^f = \mathcal{A}_e. \tag{2.61}$$

The left-right asymmetries are measured for different final state fermion flavours at the SLD experiment and will be of interest later in this work.

2.5 Higher Order Corrections

The Standard Model calculations give rise to a more precise approach than the lowest order calculations, called tree-level calculations. Higher order calculations become important with higher precision of the analysed observables. The number of Feynman diagrams contributing to higher order corrections is infinite but their sum leads to a finite result with modified couplings and masses. This is called renormalization and a theory that fullfills the requirements is called renormalizable [26]. In the following the higher order corrections will be discussed in the on-shell renormalization scheme [27]. A general Feynman diagram for the corresponding higher order processes is depicted in Figure 2.3. The fermion loop in

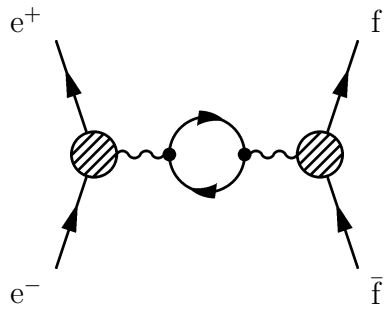

Figure 2.3: The Feynman diagram for electron-positron annihilation and fermion pair production including higher order corrections.

the middle of the propagator and the hatched blobs at the vertices denote loop corrections and vertex corrections, respectively, modifying couplings and masses. The corrections can be split into:

- **electroweak corrections -** vacuum polarisation insertions in the photon, the Z boson and the W boson including fermion loops and possible interactions with the Standard Model Higgs boson and vertex corrections
- **QCD corrections -** if the final state fermions are quarks, real gluon radiation and virtual gluon exchange in the final state
- **QED corrections -** radiation of real photons in the initial/final state and their interference and the exchange of virtual photons.

The higher order corrections modify the tree-level relation between the masses of the W boson and the Z boson (see equation 2.22).
An adequate way is to replace the mass of the W boson by the Fermi constant, G_F determined from muon lifetime measurements with much higher accuracy. The experimental result yields [22, 28, 29]:

$$G_F = 1.16637(1) \cdot 10^{-5}\ \mathrm{GeV}^{-2}. \tag{2.62}$$

The relation between m_W and G_F is given by:

$$G_F = \frac{\pi\alpha}{\sqrt{2}} \frac{1}{m_W^2 \sin^2\theta_W} \frac{1}{1-\Delta r}. \tag{2.63}$$

It contains a term Δr, that can be split into the running of the QED coupling constant $\Delta\alpha$ and weak corrections Δr_w. At leading one-loop order [30] the corrections are given by:

$$\Delta r = \Delta\alpha - \Delta r_w + \Delta r_{rem}. \tag{2.64}$$

The remaining contributions, Δr_{rem}, are smaller than the main contributions discussed below.

2.5.1 Electroweak Corrections

A set of Feynman diagrams for weak corrections is depicted in Figure 2.4. The vacuum polarisation of the W boson and the Z boson propagator is absorbed into the renormalised masses of the bosons. In equation 2.22 the relation between the W boson mass, Z boson

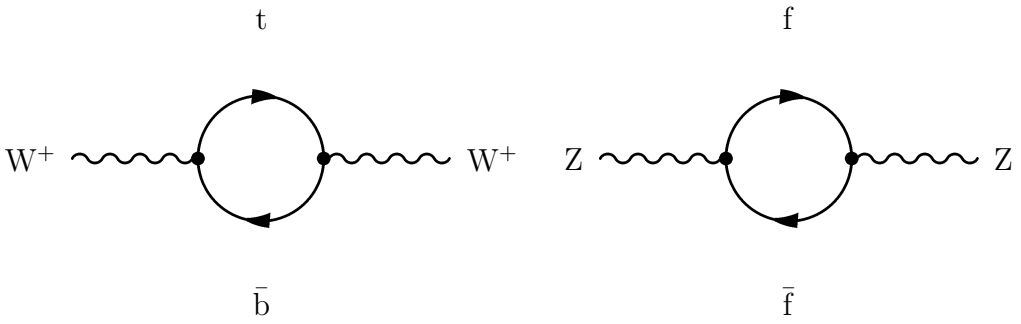

Figure 2.4: Example diagrams for electroweak corrections with fermion loops, modifying the W- and the Z-propagator.

mass and the electroweak mixing angle is expressed by the ρ-parameter which is equal to one at Born level. In the on-shell normalisation scheme where m_W and m_Z are the observed pole masses of the W and Z bosons, the electroweak mixing angle is defined as:

$$\sin^2\theta_W \equiv 1 - \frac{m_W^2}{m_Z^2} \tag{2.65}$$

The weak corrections modify the ρ-parameter and the electroweak mixing angle. This is taken into account by a term, $\Delta\rho_f$, and a form factor, κ_f, dependent on the fermion flavour. The parameters, ρ and $\sin^2\theta_W$, are modified to

$$\rho_f = 1 + \Delta\rho_f \tag{2.66}$$

$$\Delta r_w = \frac{\cos^2\theta_W}{\sin^2\theta_W}\Delta\rho_f \tag{2.67}$$

$$\kappa_f = 1 + \Delta\kappa_f \tag{2.68}$$

$$\sin^2\theta_W \rightarrow \sin^2\theta_{eff}^f = \kappa_f \sin^2\theta_W. \tag{2.69}$$

In particular, loop corrections to the W-propagator that contain top quarks contribute essentially to the ρ-parameter because of the significant difference between the top quark

mass and the bottom quark mass.
Further electroweak corrections are vertex corrections. They are implemented by ρ_f and the effective electroweak mixing angle, $\sin^2\theta^f_{eff}$, modifying the vector and axial vector couplings. The vertex corrections of $Z \to b\bar{b}$ is depicted in Figure 2.5. It provides an essential contribution, due to the large top quark mass. The corrections are the same for

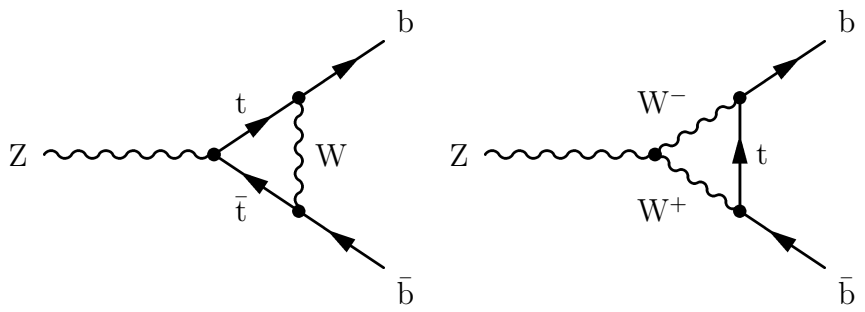

Figure 2.5: The vertex correction of the process $Z \to b\bar{b}$ due to virtual top quark exchange.

all fermion flavours, except for bottom quarks. The complete one-loop order corrections are given by [31]:

$$\Delta\rho_f = \frac{G_F}{8\pi^2\sqrt{2}}\left\{3m_t^2(1+\xi_f) - \frac{22m_W^2(m_Z^2-m_W^2)}{3m_Z^2}\left[\log\frac{m_H}{m_W} - \frac{5}{12}\right]\right\} \tag{2.70}$$

$$\xi_f = 0,\ f \neq b;\ \xi_b = -\frac{4}{3}$$

$$\begin{aligned}\Delta\kappa_f &= \frac{-G_F m_W^2}{4\pi^2\sqrt{2}(2m_W^2-m_Z^2)}\times \\ &\times \left\{\frac{3m_t^2}{2} - \frac{1}{3}\left[(10m_Z^2-9m_W^2)\log\frac{m_H}{m_Z} - 2m_Z^2\log\frac{m_t}{m_Z}\right]\right\} + \Delta\kappa_f^r\end{aligned} \tag{2.71}$$

$$\Delta\kappa_f^r = 0,\ f \neq b;\ \Delta\kappa_b^r = \frac{G_F m_t^2}{4\pi^2\sqrt{2}}$$

The remaining corrections denoted by Δr_{rem} consist of

$$\Delta r_{rem}^{top} = -\frac{G_F}{\pi^2\sqrt{2}(m_Z^2-m_W^2)}\left[\frac{3m_W^2m_t^2}{8} - \frac{m_W^2(2m_Z^2+m_W^2)}{6}\log\frac{m_t}{m_W}\right] \tag{2.72}$$

$$\Delta r_{rem}^{H} = \frac{11G_F m_W^2}{12\pi^2\sqrt{2}}\left[\log\frac{m_H}{m_Z} - \frac{5}{12}\right]. \tag{2.73}$$

The remaining corrections arising from a virtual exchange of a Higgs boson are smaller than the remaining corrections arising from virtual top quark exchange. Because the top quark contribution is primarily proportional to the square of the top mass, m_t, while the contribution of the Standard Model Higgs boson is proportional to the logarithm of the Higgs mass, m_H.
The electroweak corrections result in effective coupling constants, $\bar{g}_V^f$, $\bar{g}_A^f$ [32]:

$$\begin{aligned} \bar{g}_V^f &= g_A^f \sqrt{\rho_f}(1 - 4|Q_f|\sin^2\theta_{eff}^f) \\ \bar{g}_A^f &= g_A^f \sqrt{\rho_f}. \end{aligned} \tag{2.74}$$

The effective couplings are different for different fermions because of the flavour dependent corrections resulting in slightly different values for ρ_f and κ_f as can be seen in equation 2.70 and 2.71.

2.5.2 The running QED coupling constant

Important corrections arise from the vacuum polarisation of the photon propagator which results in the running of the electromagnetic coupling constant, α. The coupling constant becomes dependent on the centre–of–mass energy at which the scattering process takes place:

$$\alpha(s) = \frac{\alpha_0}{1 - \Delta\alpha}. \tag{2.75}$$

At low momentum transfer ($P^2 \to 0$) it is defined to become consistent with the Thomson-limit, $\alpha_0 = 1/137.03599976(50)$ [22]. This can be pictured as the change in the electron charge when approaching it from large distances. The calculation of $\alpha(m_Z)$ requires the calculation of photon vacuum polarisation (see Figure 2.6). The contributions to $\Delta\alpha$ are summed:

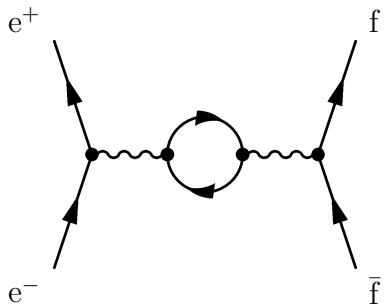

Figure 2.6: Example diagram for QED corrections: virtual fermion loops in the photon propagator contribute to the running of α.

$$\Delta\alpha = \Delta\alpha_{lep} + \Delta\alpha_{top} + \Delta\alpha_{had}^{(5)}. \tag{2.76}$$

$\Delta\alpha_{\mathrm{lep}}$ is the contribution of loops including virtual leptons. $\Delta\alpha_{\mathrm{top}}$ is small because of the large top quark mass and hence has only minor influence on $\Delta\alpha$.
$\Delta\alpha^{(5)}_{\mathrm{had}}$ yields the loop contributions of the remaining five quark flavours [33–41]. The single contributions are:

$$\begin{aligned} \mathrm{m_f} \ll \mathrm{m_Z}: \quad \Delta\alpha_{\mathrm{f}} &= \frac{\alpha}{3\pi}\mathrm{Q_f^2 N_c^f}\left[\log\left(\frac{\mathrm{m_Z}}{\mathrm{m_f}}\right)^2 - \frac{5}{3}\right] \\ \mathrm{m_f} \gg \mathrm{m_Z}: \quad \Delta\alpha_{\mathrm{top}} &= \frac{\alpha}{3\pi}\frac{4}{15}\left(\frac{\mathrm{m_Z}}{\mathrm{m_f}}\right)^2 \end{aligned} \tag{2.77}$$

As a consequence of the confinement in QCD, quarks exist only in bound states. Hence, the masses of the lighter quarks ($\mathrm{m_q} \ll \mathrm{m_Z}$) are not precisely measurable in contrast to the lepton masses. Since the masses enter the equation for running α logarithmically, $\Delta\alpha^{(5)}_{\mathrm{had}}$ provides the largest uncertainty to $\Delta\alpha$.
The graph in Figure 2.6 can be cut at the fermion loop, this provides a dispersion relation between the tree-level quark pair-production and $\Delta\alpha^{(5)}_{\mathrm{had}}$. Hence, the value of $\Delta\alpha^{(5)}_{\mathrm{had}}$ is derived from perturbative QCD calculations for centre–of–mass energies above 5 GeV and from experimental data on $\mathrm{e^+e^-} \to$ hadrons below 5 GeV using the dispersion relation:

$$\Delta\alpha^{(5)}_{\mathrm{had}} = \frac{\alpha \mathrm{s}}{3\pi}\mathcal{R}\mathrm{e}\int\limits_{4\mathrm{m}_\pi^2}^{\infty} \mathrm{ds}'\frac{\mathrm{R(s')}}{\mathrm{s'(s'-s-i\varepsilon)}}. \tag{2.78}$$

The function R(s′) is the experimental input measured in the lower energy range, where perturbative QCD is no longer applicable:

$$\mathrm{R(s')} = \frac{\sigma(\mathrm{e^+e^-} \to \mathrm{hadrons})}{\sigma(\mathrm{e^+e^-} \to \mu^+\mu^-)}. \tag{2.79}$$

Recent measurements of R(s′) carried out by the BES collaboration in the range of 2 GeV to 5 GeV yield the result $\Delta\alpha^{(5)}_{\mathrm{had}} = 0.02761 \pm 0.00036$ [42].

2.5.3 QCD Radiative Corrections

Due to the fact that the final state fermions can be a pair of quarks, also gluon radiation in the final state has to be taken into account (see Figure 2.7). The gluons are exchanged between or radiated from the final state quark. The rate of events where one or two

gluons are radiated in the final state, depends on the QCD coupling constant $\alpha_{\mathrm{s}} = \mathrm{g_3^2}/4\pi$ introduced in equation 2.35. As the hadronic width is the largest fraction of the total width of the Z the latter also depends on these corrections and thus indirectly all cross sections.

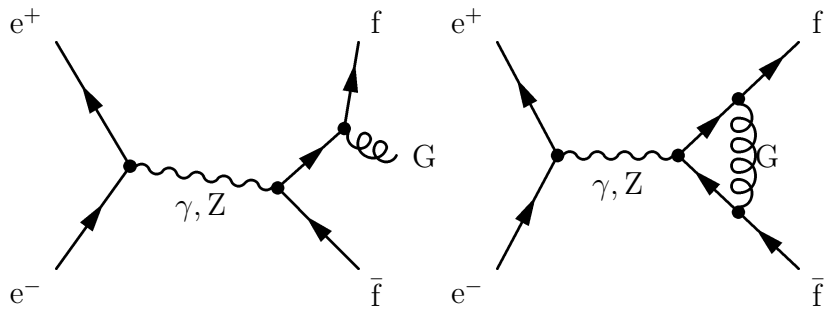

Figure 2.7: Example diagrams for QCD corrections due to gluon radiation in the final state (right) and virtual gluon exchange between the final state quarks (left).

2.5.4 Improved Born Approximation

The changes due to electroweak and QCD corrections lead to modifications in the observables. Hence, the lowest order equations can be rewritten replacing the couplings, the electroweak mixing angle and the mass of the W by effective couplings, the effective electroweak mixing angle and the Fermi constant 2.63. This is the so called **Improved Born Approximation**. Furthermore, the QED and QCD related corrections are taken into account. For example the decay width of the Z into fermions is modified. In case of leptons the decay width can be expressed by [32, 43–45]:

$$\Gamma_{\bar{l}l} = \frac{G_F m_Z^3}{6\pi\sqrt{2}}\sqrt{1-\frac{4m_l^2}{m_Z^2}}\left[\left(1+\frac{2m_l^2}{m_Z^2}\right)\left((\bar{g}_V^f)^2+(\bar{g}_A^f)^2\right)-\frac{6m_l^2}{m_Z^2}(\bar{g}_A^f)^2\right]\left(1+\frac{3\alpha(m_Z^2)Q_f^2}{4\pi}\right) \quad (2.80)$$

In of case quarks ($f = u, d, c, s, b$) the decay width is modified to

$$\Gamma_{f\bar{f}} = N_c^f\frac{G_F m_Z^3}{6\pi\sqrt{2}}\left[R_V^f(m_Z^2)(\bar{g}_V^f)^2+R_A^f(m_Z^2)(\bar{g}_A^f)^2\right]+\Delta_{EW/QCD}. \quad (2.81)$$

The radiator factors, $R_{V,A}^f(m_Z^2)$, describe the final state QED and QCD vector and axial vector corrections for quarkonic decay modes [43, 46]. The non-factorizable EW $\otimes$ QCD corrections, $\Delta_{EW/QCD}$, have a relative order of magnitude of less than one per mill. In case of bottom quarks $\Delta_{EW/QCD} = -0.040$ MeV. The corrections modify the total decay width of the Z boson, the height of the Z-resonance and its nominal position.

2.6 QED corrections

Apart from the running of the coupling constant α, initial state bremsstrahlung contributes to higher order effects (see Figure 2.8). This contribution is different from the running of α in the sense, that the photon is real and hence observable. In order

to be consistent with the measurement and the Standard Model prediction at a certain centre–of–mass energy, the initial state radiation has to be taken into account.

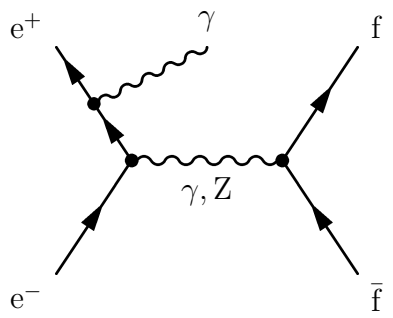

Figure 2.8: Example diagram with initial state radiation. At least one of the initial state leptons radiates a photon before the annihilation.

The squared centre–of–mass energy, s, can be expressed as the four-momenta of the colliding initial state electrons:

$$s = (p_{e^-} + p_{e^+})^2 \tag{2.82}$$

where p_{e^-} and p_{e^+} are the four-momenta of the initial state electron and positron, respectively.
The energy losses due to bremsstrahlung lead to collisions at a reduced effective centre–of–mass energy, called s' ($s' \leq s$) [43]:

$$s' = (p'_f + p'_{\bar{f}})^2 \tag{2.83}$$

The four-momenta, p'_f, $p'_{\bar{f}}$ are the momenta of the final state fermions. If there is no photon radiated before the collision, the electron and positron collide at the nominal centre–of–mass energy. The radiation of one or more initial state photons changes the configuration of four-momenta. Taking the square of the nominal set centre–of–mass energy, s, into account, s' can be expressed as:

$$s' = s - 2E_\gamma\sqrt{s} + M^2_{\gamma\gamma}. \tag{2.84}$$

E_γ is the sum of the energies of the radiated photons. $M_{\gamma\gamma}$ is the invariant mass of the photon system, which is different from zero only in case when more than one photon was radiated. Hence, the improved Born cross section is convoluted by a function $R^{ini}(s', s)$ in an integral [43]:

$$\sigma_{f\bar{f}}(s) = \int_{\frac{4m_f^2}{s}}^{1} \frac{ds'}{s}\sigma_{f\bar{f}}(s')R^{ini}(s', s). \tag{2.85}$$

The function $R^{ini}(s', s)$ is called radiation function.
The initial state bremsstrahlung reduces the cross section at the Z resonance by a factor of ≈ 0.74. Moreover, the shape of the resonance becomes asymmetric due to the radiative tails and the nominal position of the resonance is shifted towards higher values by 89 MeV [30].

The final state radiation and the initial-final state radiation interference are treated in a similar manner with functions $R^{fin}(s', s)$ and $R^{int}(s', s)$, respectively [43]. In case of the hadronic cross section the contribution from final state radiation correction is of the order of 1%-2% and less than 1% for the contribution from initial-final state radiation interference at centre–of–mass energies of $\sqrt{s} \approx 200$ GeV.
In case of hadronic final states the final state radiation photons are not separable from other final state particles and hence are treated as belonging to the resulting jet. This fact is taken into account and properly corrected for using ZFITTER V6.35 [43].

2.7 The Process $e^+e^- \rightarrow$ Hadrons

The branching ratio of the Z boson decaying into a pair of quarks is 69%. Among the five possible pair-produced quark flavours, the bottom quark is the heaviest quark flavour and can be best distinguished. Hence, apart from the total hadronic cross section, σ_{had}, R_b and A_{fb}^b are further useful observables to study the vector and axial vector couplings of the Z boson to the bottom quark. The total hadronic cross section, σ_{had}, R_b and A_{fb}^b are defined as:

$$\sigma_{had} = \sum_q \sigma_{q\bar{q}} \tag{2.86}$$

$$R_b = \frac{\sigma_{b\bar{b}}}{\sigma_{had}} \tag{2.87}$$

$$A_{fb}^b = \frac{\sigma_{b\bar{b}}^{fb}}{\sigma_{b\bar{b}}}. \tag{2.88}$$

At the Z-resonance ($\sqrt{s} = m_Z$) the $\gamma - Z$-interference term is zero. After the correction for phtoton exchange, σ_{had}, R_b and A_{fb}^b can be expressed by pseudo-observables denoted with an extra index (zero) which depend on the effective vector and axial vector couplings as:

$$\sigma_{had}^0 = \frac{4\pi\alpha^2}{\Gamma_Z^2 \sin^4\bar{\theta}_W \sin^2\bar{\theta}_W^2}[(\bar{g}_V^e)^2 + (\bar{g}_A^e)^2] \sum_q [(\bar{g}_V^q)^2 + (\bar{g}_A^q)^2] \tag{2.89}$$

$$R_b^0 = \frac{(\bar{g}_V^b)^2 + (\bar{g}_A^b)^2}{\sum_q (\bar{g}_V^q)^2 + (\bar{g}_A^q)^2} \tag{2.90}$$

$$A_{fb}^{0,b} = \frac{3}{4}\mathcal{A}_e\mathcal{A}_b, \tag{2.91}$$

where $\mathcal{A}_f$ is the coupling parameter of the corresponding fermion given in equation 2.52. These equations are obtained by integrating the term in the differential cross section of equation 2.42- 2.44 due to Z boson exchange. The effects due to the masses of the contributing fermions are not explicitely given in the equations but they are not negligible and taken into account in the calculations. A measurement of σ_{had}, R_b and A_{fb}^b at the Z-resonance still depends on the contribution of photon exchange. This contribution is

less than one per mill for σ_{had} and R_b and of the order of 30% for A_{fb}^b (computed with ZFITTER V6.35).
At centre–of–mass energies above the Z-resonance the interference term in the cross section (see equation 2.42- 2.44) is different from zero and becomes more important with the rising centre–of–mass energy. Thus, to obtain σ_{had}, R_b and A_{fb}^b at centre–of–mass energies above the Z-resonance the entire cross section definition in equation 2.42- 2.44 has to be integrated. Hence, the $\gamma - Z$-interference term provides further constraints on the effective vector and axial vector couplings of the Z boson to the bottom quark:

$$\sigma_{had} = \frac{4\pi\alpha^2}{s}\sum_{q=u}^{b} Q_e^2 Q_q^2 + 2Q_e Q_q \bar{g}_V^e \bar{g}_V^q \mathcal{R}e\{\chi\} \tag{2.92}$$

$$+ \; ((\bar{g}_V^e)^2 + (\bar{g}_A^e)^2)((\bar{g}_V^q)^2 + (\bar{g}_A^q)^2)|\chi|^2 \tag{2.93}$$

$$R_b = \frac{Q_e^2 Q_b^2 + 2Q_e Q_b \bar{g}_V^e \bar{g}_V^b \mathcal{R}e\{\chi\} + ((\bar{g}_V^e)^2 + (\bar{g}_A^e)^2)((\bar{g}_V^b)^2 + (\bar{g}_A^b)^2)|\chi|^2}{\sum_{q=1}^{5} Q_e^2 Q_q^2 + 2Q_e Q_q \bar{g}_V^e \bar{g}_V^f \mathcal{R}e\{\chi\} + ((\bar{g}_V^e)^2 + (\bar{g}_A^e)^2)((\bar{g}_V^q)^2 + (\bar{g}_A^q)^2)|\chi|^2}$$

$$A_{fb}^b = \frac{2}{3}\frac{Q_e Q_b \bar{g}_A^e \bar{g}_A^b \mathcal{R}e\{\chi\} + 2\bar{g}_V^e \bar{g}_V^b \bar{g}_A^e \bar{g}_A^b |\chi|^2}{Q_e^2 Q_b^2 + 2Q_e Q_b \bar{g}_V^e \bar{g}_V^b \mathcal{R}e\{\chi\} + ((\bar{g}_V^e)^2 + (\bar{g}_A^e)^2)((\bar{g}_V^b)^2 + (\bar{g}_A^b)^2)|\chi|^2}. \tag{2.94}$$

In Figure 2.9 and 2.10, σ_{had}, R_b and A_{fb}^b are depicted as a function of the centre–of–mass energy. The dashed curves describe the Standard Model prediction for σ_{had}, R_b and A_{fb}^b without a selection criterion on the effective centre–of–mass energy, s', and the solid curves with a selection criterion on $\sqrt{s'} > 0.85\sqrt{s}$. The selection criterion makes sure that only collisions well above the Z-resonance are studied and hence the measurements of σ_{had}, R_b and A_{fb}^b are sensitive to the $\gamma - Z$-interference term in the cross section of the processes $e^+e^- \to b\bar{b}$ and $e^+e^- \to$ hadrons which yield additional constraints on the effective vector and axial vector couplings (see equation 2.42- 2.44).

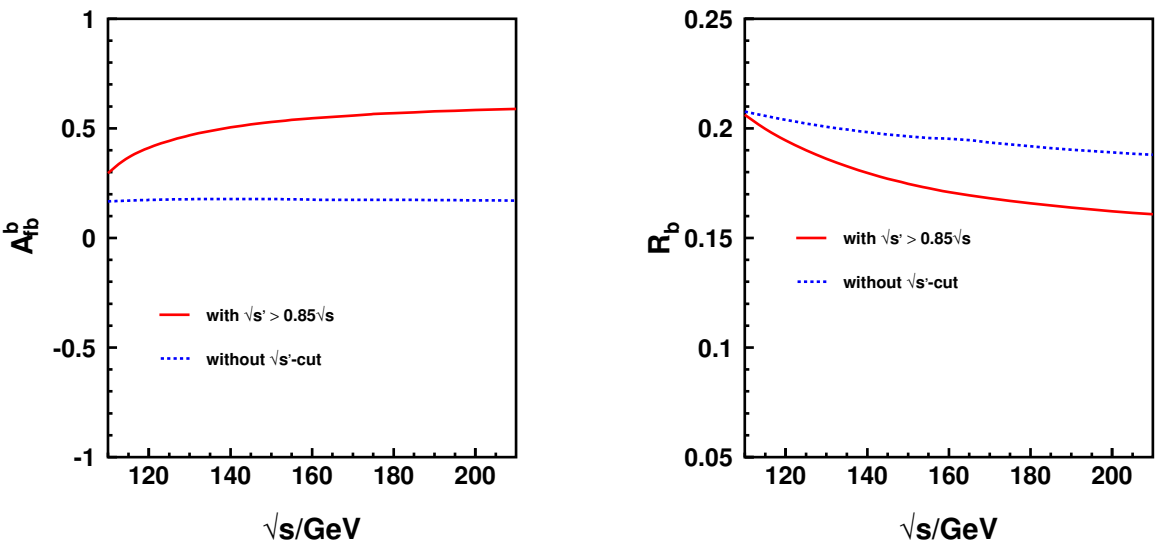

Figure 2.9: The dependence of $A_{\mathrm{fb}}^{\mathrm{b}}$ (left) and $\mathrm{R_b}$ (right) on the centre–of–mass energy. The dashed curve is the Standard Model prediction without a selection criterion on the effective centre–of–mass energy, s′. The solid curve depicts the Standard Model prediction with a selection criterion on the effective centre–of–mass energy, $\sqrt{\mathrm{s}'} > 0.85\sqrt{\mathrm{s}}$.

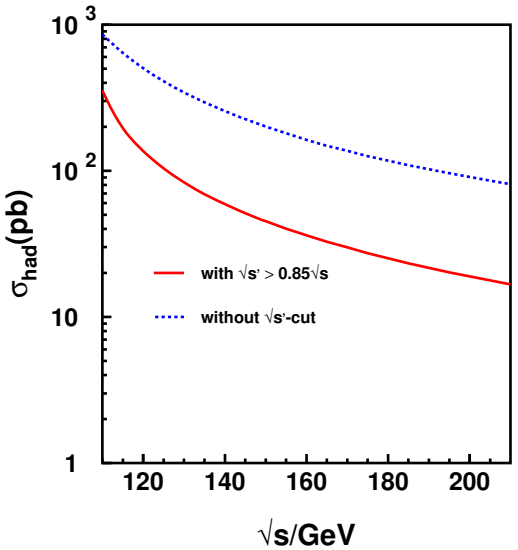

Figure 2.10: The dependence of σ_{had} on the centre–of–mass energy, depicted like in Figure 2.9.

Moreover, the measurement of σ_{had}, $\mathrm{R_b}$ and $A_{\mathrm{fb}}^{\mathrm{b}}$ at centre–of–mass energies above the Z-resonance improves the sensitivity to new effects compared to the Z-resonance, where those effects could only appear in higher order corrections.
The Standard Model contains 18 free parameters, whose values are not predicted and must be determined by experiment. These are:

- the coupling constants (α, α_{s})
- the masses of fermions and bosons
- the numbers in the CKM matrix

Since this work focusses on neutral current processes where the CKM matrix is not involved and the fermion masses are included from reference [22], the Standard Model is represented by a minimal set of six linearly independent parameters. The parameters are obtained from the Standard Model fits to the combined LEP electroweak measurements carried out by the LEP Electroweak Working Group (LEPEWWG see [47]):

- the hadronic contribution to the running electromagnetic coupling constant, $\Delta\alpha_{\mathrm{had}}^{(5)} = 0.02761 \pm 0.00036$
- the strong coupling constant, $\alpha_{\mathrm{s}}(\mathrm{m_Z^2}) = 0.1183 \pm 0.0026$
- the mass of the Z boson, $\mathrm{m_Z} = 91.1875 \pm 0.0021$ GeV
- the mass of the top quark, $\mathrm{m_t} = 174.3 \pm 5.1$ GeV
- the mass of the Standard Model Higgs boson, $\mathrm{m_H} = 300^{+700}_{-186}$ GeV
- the Fermi constant, $\mathrm{G_F} = 1.16639(1) \cdot 10^{-5}$ GeV^{-2}.

The Standard Model Higgs boson is not discovered and the mass is set to a value between the lower limit of $\mathrm{m_H} = 114.1$ GeV [48] obtained by direct searches and the theoretically allowed upper limit of $\mathrm{m_H} = 1000$ GeV. These six parameters determine what is referred to as the Standard Model. Every value in this work denoted as Standard Model prediction is computed on the basis of the numbers of these six parameters.

2.8 Beyond the Standard Model

Deviations of observables from the Standard Model prediction might be caused by physics phenomena not described by the Standard Model. In case of an extra gauge boson, the matrix element given in equation 2.40 will be modified to:

$$\begin{aligned} |\mathcal{M}|^2 &= |\mathcal{M}_\gamma + \mathcal{M}_{\mathrm{Z}} + \mathcal{M}_{\mathrm{X}}|^2 \\ &= |\mathcal{M}_\gamma|^2 + |\mathcal{M}_{\mathrm{Z}}|^2 + 2\underbrace{\mathcal{R}e\{\mathcal{M}_\gamma\mathcal{M}_Z^* + \mathcal{M}_\gamma\mathcal{M}_X^* + \mathcal{M}_Z\mathcal{M}_X^*\}}_{\text{interference}} + |\mathcal{M}_{\mathrm{X}}|^2. \end{aligned} \tag{2.95}$$

The parts of the cross section corresponding to $\mathcal{M}_\gamma$ and $\mathcal{M}_{\mathrm{Z}}$ resulting from pure photon and pure Z exchange are precisely measured. The pure new physics term $\mathcal{M}_{\mathrm{X}}$ must be very small. Otherwise, deviations from the Standard Model prediction would have been

already detected. As a consequence, the interference term will enable the search for new effects in High Energy Physics.
A set of possible Standard Model extensions are listed:

- Contact Interactions (CI)
- fermion sizes
- models with an additional neutral heavy gauge boson (Z′)
- low scale gravity with extra dimensions.

Apart from the Standard Model parameters, there will be other, further parameters to describe the new phenomena and to determine their strength. These can be scales, form factors and additional coupling constants. If no significant deviation from the Standard Model is obtained, limits are set on the new parameters.

2.8.1 Contact Interactions

A general ansatz of Standard Model extensions is the model independent extension of the Lagrangian by a contact interaction term [49] shown in Figure 2.11. Analogous to the

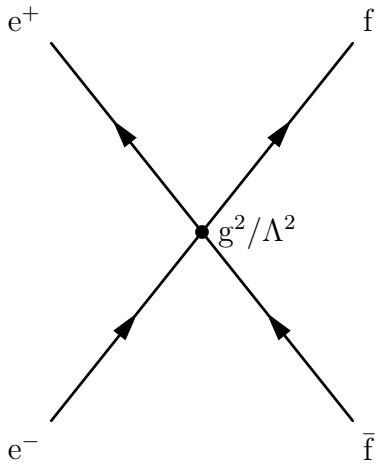

Figure 2.11: The diagram for four-fermion contact interaction.

concept of Fermi [50] concerning the muon decay, a new kind of interaction is introduced as a contact interaction. This concept is valid as long as the scale Λ is much larger than the centre–of–mass energy at which the corresponding final states are studied ($\sqrt{s} \ll \Lambda$). The additional term in the Lagrangian, called effective Lagrangian is expressed by:

$$\begin{aligned} \mathcal{L} &= \mathcal{L}_{\mathrm{EW}} + \mathcal{L}_{\mathrm{eff}} \qquad (2.96) \\ \mathcal{L}_{\mathrm{eff}} &\sim \frac{1}{1+\delta_{\mathrm{ef}}} \sum_{\mathrm{i,k=L,R}} \eta_{\mathrm{ik}} \frac{g^2}{\Lambda^2} (\bar{e}_i \gamma^\mu e_i)(\bar{f}_k \gamma^\mu f_k), \end{aligned}$$

where e_i and f_k denote the left- and right-handed initial-state electrons and final-state fermions. The Kronecker symbol, δ_{ef}, is zero except for the e^+e^- final state, where it is

one. The parameter η_{ik} defines the contact interaction model by choosing the helicity amplitudes which contribute to the reaction $e^+e^- \to f^+f^-$. The value g^2/Λ^2 determines the size of the expected effects. By convention $g^2/4\pi$ is chosen to be 1 and $|\eta_{ik}| = 1$ or $|\eta_{ik}| = 0$, leaving the energy scale Λ as only free parameter.
The new interaction terms resulting from the effective Lagrangian will modify the cross section by extending the helicity amplitudes in equation 2.58:

$$\mathcal{A}^{ef}_{ik} = \frac{4\pi\alpha^2}{s} Q_e Q_f + \frac{\pi\alpha^2 g^e_i g^f_k}{\sin^2\theta_W \cos^2\theta_W (s - m_Z^2 + i\Gamma_Z m_Z)} + \frac{\eta_{ik}}{\Lambda^2}. \tag{2.97}$$

The differential cross section:

$$\frac{d\sigma_{f\bar{f}}}{d\cos\Theta} = \frac{d\sigma^{SM}_{f\bar{f}}}{d\cos\Theta} + C_2(s, \cos\Theta)\frac{1}{\Lambda^2} + C_4(s, \cos\Theta)\frac{1}{\Lambda^4}, \tag{2.98}$$

contains, beside the Standard Model term denoted by SM, terms that depend on functions C_2 and C_4 and the energy scale Λ. The additional term proportional to C_2 describes the interference of the new interaction with the Standard Model while C_4 is the pure new physics contribution.
In case of quarks, the hadronic cross section σ_{had}, R_b and A^b_{fb} could be modified and deviate from the Standard Model prediction.

2.8.2 Fermion Sizes

A specific ansatz for Contact Interactions is the introduction of form factors to the boson-fermion vertices assuming the fermions to have a measurable size. In the Standard Model fermions are considered to be point-like objects. Nevertheless, a substructure of the fermions, in particular the quarks, cannot be excluded. Once again referring to the differential cross section in equation 2.54, the helicity amplitudes are modified by additional form factors $f_e(s)$ and $f_f(s)$ depending on the centre–of–mass energy and the fermion size [11]:

$$|\mathcal{A}^{ef}_{ik}|^2 \to |\mathcal{A}^{ef}_{ik}|^2 f_e^2(s) f_f^2(s) \tag{2.99}$$

$$f_i(s) = 1 + \frac{1}{6} R^2 s. \tag{2.100}$$

The total cross section changes to:

$$\sigma_{f\bar{f}}(s) = \sigma^{SM}_{f\bar{f}}(s) \cdot f_e^2(s) \cdot f_q^2(s), \tag{2.101}$$

for each process where quarks are involved. $f_e(s)$ and $f_q(s)$ are the structure functions of the electrons and quarks, respectively. R is here regarded as the fermion radius.

2.8.3 Extra Z Bosons

The introduction of contact interactions is a widely model independent approach to new interactions. A model dependent extension assuming a specific structure of the new

interaction is the introduction of a new gauge boson, Z′ [51]. The introduction of a new interaction arises from the idea to unify all known interaction in one Grand Unified Theory (GUT), based on a gauge group with higher dimensionality. The group E_6 is a possible candidate for a gauge group of the GUT, which breaks down to:

$$E_6 \rightarrow SU(3)_C \otimes SU(2)_L \otimes U(1)_Y \otimes U(1)_\chi \otimes U(1)_\psi \tag{2.102}$$

$$E_6 \rightarrow \underbrace{SU(3)_C \otimes SU(2)_L \otimes U(1)_Y}_{\text{Standard Model}} \otimes SU(2)_R \otimes U(1)_{B-L}. \tag{2.103}$$

Each of the groups is connected with a set of gauge bosons as carrier of the interaction force. Hence, the new groups will introduce at least one new gauge boson. The gauge group $SU(2)_R$ introduces right-handed doublets, which do not exist in the Standard Model (see Table 2.1), and hence a left-right symmetric model. $U(1)_{B-L}$ introduces the conservation of baryon and lepton number simultaneously.
The new interaction modifies the part of the Lagrangian, that describes the neutral current interaction given in equation 2.24:

$$\mathcal{L}_{NC} = -\frac{g_1 g_2}{\sqrt{g_1^2 + g_1^2}} A_\mu J^\mu_{EM} + \sqrt{g_1^2 + g_1^2} Z_\mu J^\mu_{NC} + g' J^\mu_{Z'} Z'_\mu, \tag{2.104}$$

containing the interaction of the fermions with a new gauge boson Z′. In addition to the neutral current, given in equation 2.30, one obtains neutral currents of the form:

$$J^\mu_{Z'} = J^\mu_\chi \cos\Theta_6 + J^\mu_\psi \sin\Theta_6 \tag{2.105}$$

$$J^\mu_{Z'} = \alpha_{LR} J^\mu_{3R} - \frac{1}{2\alpha_{LR} J^\mu_{B-L}}, \tag{2.106}$$

arising from $U(1)_\chi \otimes U(1)_\psi$ or $SU(2)_R \otimes U(1)_{B-L}$, respectively. The angle Θ_6 describes a possible mixing scenario of the gauge bosons coming from $U(1)_\chi$ and $U(1)_\psi$. Specific cases are $\Theta_6 = 0; \pi/2; -\arctan\sqrt{5/3}$ describing the χ, ψ and η model, respectively.
α_{LR} is the coupling constant introduced for a left-right symmetric model. The left-right symmetric models with a coupling constant in the range $\sqrt{2/3} \leq \alpha_{LR} \leq \sqrt{\cot^2\theta_W - 1}$ are favoured. J^μ_{B-L} arises from $U(1)_{B-L}$; J^μ_{3R} is the third component of the fermion current arising from $SU(2)_R$.
A possible ZZ′ mixing would modify the couplings of the Z boson to the fermions. Precision measurements on the Z resonance are sensitive to the couplings and, hence to the ZZ′ mixing angle, θ_M:

$$\begin{pmatrix} Z \\ Z' \end{pmatrix} = \begin{pmatrix} \cos\theta_M & \sin\theta_M \\ \cos\theta_M & -\sin\theta_M \end{pmatrix} \begin{pmatrix} Z_0 \\ Z'_0 \end{pmatrix}, \tag{2.107}$$

where Z_0 and Z'_0 denote the unmixed states and Z and Z′ denote the mass eigenstates. Z_0 is the weak gauge boson introduced earlier in equation 2.22. Z is to be identified with m_Z

measured at LEP I.
If the ZZ′ mixing angle is zero, the vector and axial vector couplings to the Z to the fermions are:

$$g_V^f(Z) = \cos\theta_M g_V^f(Z_0) + \frac{g'}{g}\sin\theta_M g_V^f(Z_0') \quad (2.108)$$

$$g_A^f(Z) = \cos\theta_M g_A^f(Z_0) - \frac{g}{g'}\sin\theta_M g_A^f(Z_0'). \quad (2.109)$$

The coupling constant $g = \sqrt{g_1^2 + g_2^2}$ corresponds to the coupling constants introduced in equation 2.24.
Since the electroweak mixing angle θ_W is related to the W and Z boson masses (see equation 2.22), a small mixing angle leads to a term $\Delta\rho_{Z'}$:

$$\Delta\rho_{Z'} = \sin^2\theta_M\left(\frac{m_{Z'}^2}{m_Z^2} - 1\right). \quad (2.110)$$

This contribution to the ρ-parameter also affects the effective vector and axial vector couplings. In this case the effective vector and axial vector couplings (see equation 2.74) of the Z boson in presence of a Z′ boson are given by:

$$\begin{aligned}
\bar{g}_V^f &= g_A^f\sqrt{\rho_f^M}(1 - 4|Q_f|\sin^2\bar{\theta}_W) \quad (2.111)\\
\bar{g}_A^f &= g_A^f\sqrt{\rho_f^M}\\
\sin^2\bar{\theta}_W &= \kappa_f^M\sin^2\theta_W\\
\rho_f^M &= (1 + \Delta\rho_{Z'})(1 - y_f)^2\rho_f\\
\kappa_f^M &= (1 - x_f)\kappa_f,
\end{aligned}$$

where x_f and y_f are functions of the mixing angle, the couplings constants g and g′ and the vector and axial vector couplings of Z and Z′ without ZZ′ mixing [52]. The measurements carried out LEP I give a strict limit on the ZZ′ mixing angle of [53]:

$$|\theta_M| < 2\cdot 10^{-3}, \quad (2.112)$$

which is compatible with vanishing ZZ′ mixing ($\theta_M = 0$).
At high energies the vector and axial vector couplings and hence σ_{had}, R_b and A_{fb}^b will be modified due to $\gamma - Z'$ and $Z - Z'$ interference as pointed out in 2.96.

2.8.4 Graviton Exchange

A Grand Unified Theory, as mentioned above, would also include a theory of quantum-gravity. Nowadays, the understanding of particle physics is based on different energy scales at which particle interactions take place. The electroweak scale is of the order of $M_{EW} \approx 1$ TeV, while quantum-gravity effects appear only to be measurable at an energy scale near the Planck mass $M_P = 1.2\cdot 10^{19}$ GeV and are therefore undetectable at present

or future collider experiments.
Arkani-Hamed, Dimopoulos and Dvali [54, 55] have made the proposal that gravity can propagate in a higher-dimensional space, while Standard Model particles propagate in the Minkowski space of 3+1 dimensions. The relative weakness of gravity with respect to the other fundamental forces is related to the size of compactified extra dimensions. The Newtonian constant, G_N measured in the 3+1-dimensional space can be expressed as:

$$G_N^{-1} = 8\pi M_P^2 = 8\pi R^\delta M_{EW}^{\delta+2}. \tag{2.113}$$

Hence, the Planck scale is related to the electroweak scale by:

$$M_p^2 = R^\delta M_{EW}^{\delta+2}. \tag{2.114}$$

δ is the number of extra dimensions and R is the radius of the compactified space.
The introduced graviton, a spin-2 boson, propagates in $4+\delta$ dimensions and interacts with Standard Model particles in 4 dimensions. The interaction is of the strength $\approx M_{EW}^{-1}$. The additional interaction modifies the total cross section [56]:

$$\begin{aligned}
\frac{d\sigma_{f\bar{f}}}{dx}(s) &= \frac{d\sigma_{f\bar{f}}^{SM}}{dx}(s) + \frac{N_c \pi s^3}{64\Lambda_T^8}(1 - 3x^2 + 4x^4) \qquad (2.115)\\
&- \frac{N_c \alpha \pi}{2\Lambda_T^4}\left[3Q_e Q_f x^3\right]\\
&- \frac{N_c \alpha \pi}{2\Lambda_T^4}\left[\frac{1}{2\sin^2 2\theta_W}\frac{s(s-m_Z^2)}{(s-m_Z^2)^2 + \Gamma_Z^2 m_Z^2}[6 g_V^e g_V^f + g_A^e g_A^f (3x^2 - 6x - 1)]\right]\\
\sigma_{f\bar{f}}(s) &= \sigma_{f\bar{f}}^{SM}(s) + \frac{N_c s^3 \pi}{32\Lambda_T^8}, \qquad (2.116)
\end{aligned}$$

with $x = \cos\Theta$. The energy scale Λ_T can be transformed into a mass scale M_s:

$$\Lambda_T^4 = \frac{\pi}{2} M_s^4 \tag{2.117}$$

$$\sigma_{f\bar{f}}(s) = \sigma_{f\bar{f}}^{SM}(s) + \frac{N_c s^3}{20\pi M_s^8}. \tag{2.118}$$

The cross section becomes dependent on the mass scale which may hence be experimentally determined.

Chapter 3

The L3 Experiment at LEP

3.1 The e^+e^- Collider LEP

The **L**arge **E**lectron **P**ositron Collider LEP is situated at the European Laboratory for Particle Physics (CERN) near Geneva. LEP was designed and built to measure electroweak interactions in high energy physics from the Z-resonance up to 210 GeV centre–of–mass energy.
The LEP machine is a circular collider of about 27 km circumference. Electrons and positrons are accelerated in opposite directions and are brought to collision in four different interaction regions. The four experiments ALEPH, DELPHI, L3 and OPAL are located at these intersection points to record the annihilation products of the initial e^+e^-pair and measure their energies and momenta. A map of the LEP area is shown in Figure 3.1.
LEP was running in two phases. At LEP I, from 1989 until 1995, colliding beams of a centre–of–mass energy around the Z resonance were delivered to study the properties of the Z boson. At LEP II, from 1995 until 2000, the centre–of–mass energy was continuously increased in order to study known processes of the Standard Model at higher energies and to search for new phenomena in high energy physics. One of the most important topics was the search for the Standard Model Higgs boson.
The collider ring consists of eight bending and eight straight sections. The experiments are located at four of the straight sections. The electron and positron beam each contain four bunches. At LEP I these bunches were replaced by trains of up to four smaller bunchlets, the so called LEP bunch train regime. Electrons and positrons are delivered and injected via a complex system of smaller storage rings. After the filling of LEP electrons and positrons are accelerated by a set of superconducting cavities. In the year 2000 LEP delivered about 230 pb^{-1} integrated luminosity to each of the experiments and reached 210 GeV centre–of–mass energy. This was the most outstanding performance of the LEP machine.

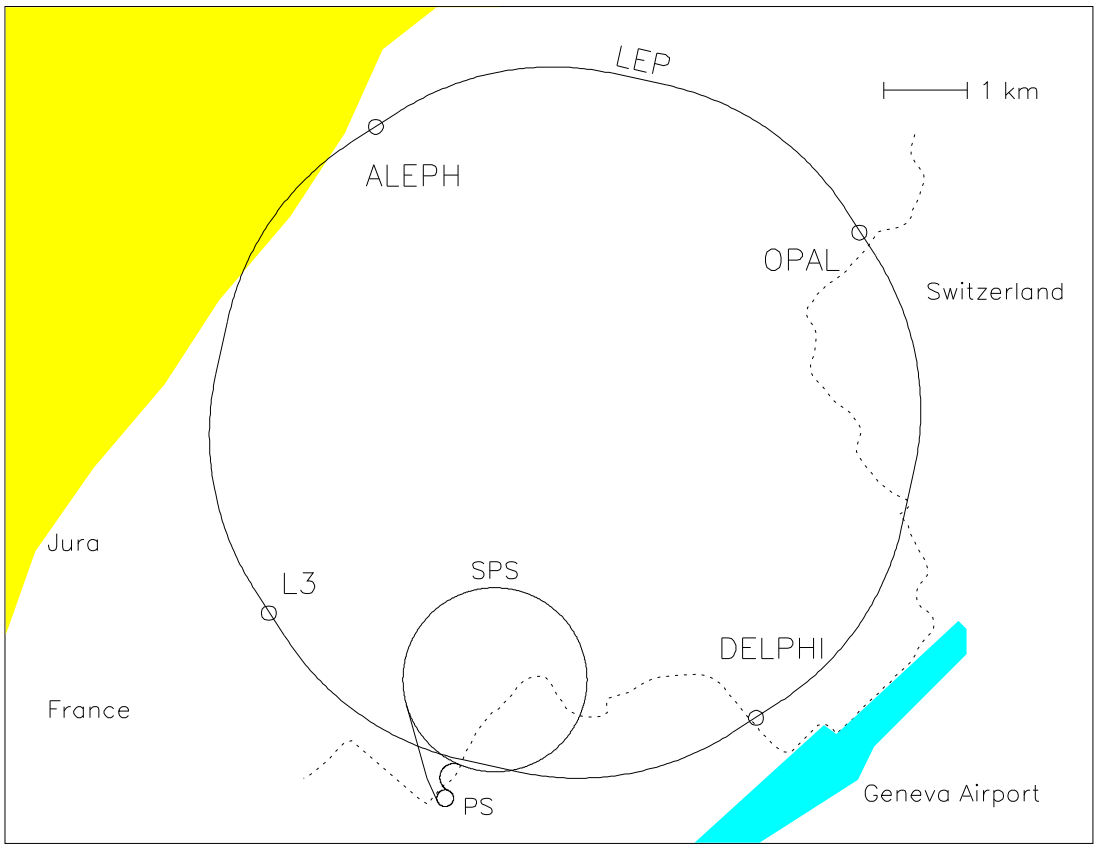

Figure 3.1: A general view on the LEP storage ring and the locations of the experiments ALEPH, DELPHI, L3 and OPAL.

3.2 The L3 coordinate system

In order to combine geometric information of the detector components, a standard coordinate system is introduced:

- the origin of the coordinate system is the nominal interaction point of the colliding electrons and positrons
- the z axis points along the incoming electron beam
- the x axis points from the centre of the LEP ring to the interaction point
- the y axis points vertically upwards.

The cartesian coordinates can be transferred into polar coordinates expressed as radius r, the azimuthal angle ϕ and the polar angle θ:

- the polar angle, θ, is defined w.r.t. the z axis
- the azimuthal angle, ϕ, is defined in the xy-plane w.r.t. the x axis

- the radius, r, is defined as radial distance from the interaction point.

3.3 The L3 Detector

The L3 detector (Figure 3.2) is a general purpose detector with particular emphasis on the precise measurement of energy and momentum of photons, electrons and muons. The detector is housed in a 12 m inner diameter magnet of a height of about 15 m and a weight of about 7800 tons. The magnet provides a solenoidal magnetic field of 0.5 T along the beams. The different subdetector components are subdivided into barrel and endcap parts. These components are enumerated as follows starting with the most inner subdetector:

1. the Silicon Microvertex Detector (SMD)
2. the Central Tracking Chambers (TEC, Z-chamber)
3. the Electromagnetic Calorimeter (BGO)
4. the Scintillation Counters
5. the Hadron Calorimeter (HCAL)
6. the Muon Chambers
7. the Luminosity Monitor
8. the Trigger System

A 32 m long and 4.45 m diameter support tube runs concentric to the beam line through the detector housing the inner subdetectors. This support tube can be adjusted by micromovers to allow the alignment of the inner subdetectors with respect to the electron and positron beam. A technically detailed description of the L3 detector can be found elsewhere [57].

3.3.1 The Silicon Microvertex Detector

The Silicon Microvertex Detector (SMD) (Figure 3.4) is the innermost subdetector. It is located on the beam pipe of LEP at a radius of 5.5 cm around the beams and with an active length of 30 cm. It is cooled with water in order to gain stable working conditions. The SMD is designed, built and installed to improve the central tracking capability of the L3 detector, using the existing silicon technology. The detector design is specialised to measure charged particle tracks with high spatial precision. The SMD is built from two radial layers of double-sided silicon strip detectors and provides $r - \phi$ and $r - z$ coordinate measurements over the polar angle range $|\cos\theta| \leq 0.93$ and over the full azimuth. The total area of instrumented silicon is $2 \times 0.25 m^2$. Each layer consists of 12 modules (ladders). Each ladder is built from two separate half-ladders that, in turn, is built from two electrically and mechanically joined double-sided silicon sensors. The silicon sensors (Figure 3.3) are 70 mm long and 40 mm wide and made from 300 μm thick high purity n-type silicon. The junction side has an implantation strip every 25 μm and a readout

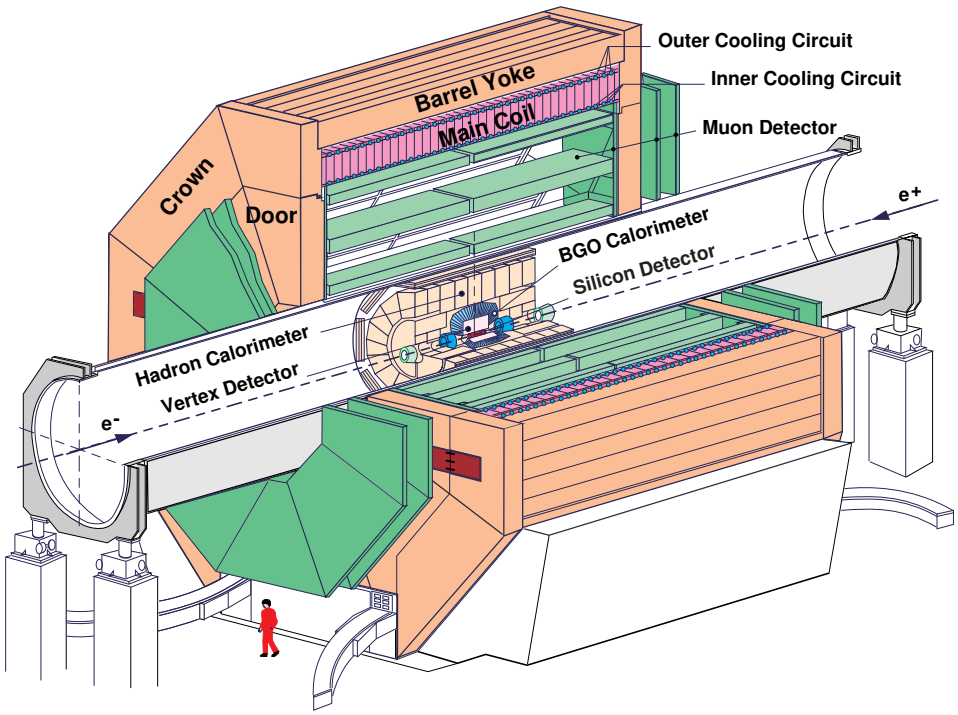

Figure 3.2: A perspective view on the L3 detector.

pitch of 50 μm. These strips run parallel to the long side of each sensor (beam direction) to measure the r $-$ ϕ coordinate. The implantation strips on the opposite side run perpendicular to the strips on the junction side. The separation of the strips is 50 μm. The readout pitch is 200 μm over the polar angle range $|\cos\theta| = 0.93 \rightarrow 0.53$ and 150 μm over the range $|\cos\theta| = 0.53 \rightarrow 0$. The polar angle θ is measured with respect to the e^- beam direction. The expected and obtained resolution is 7 μm in r $-$ ϕ and 14 μm in r $-$ z.

3.3.2 The Central Tracking Chambers

The L3 tracking detector is designed and built to perform vertex detection and particle tracking. This part of the detector consists of three components, the Time Expansion Chamber (TEC), the Plastic Scintillating Fibres (PSF) and the Z-chamber. The tasks of the tracking system are the measurement of the transverse momentum and the determination of the sign of the particle charge, the measurement of the polar angle of charged tracks, the determination of the charge multiplicity (number of charged particle tracks) of the event and the determination of the entrance point of a particle to the electromagnetic calorimeter in order to distinguish electrons and photons.

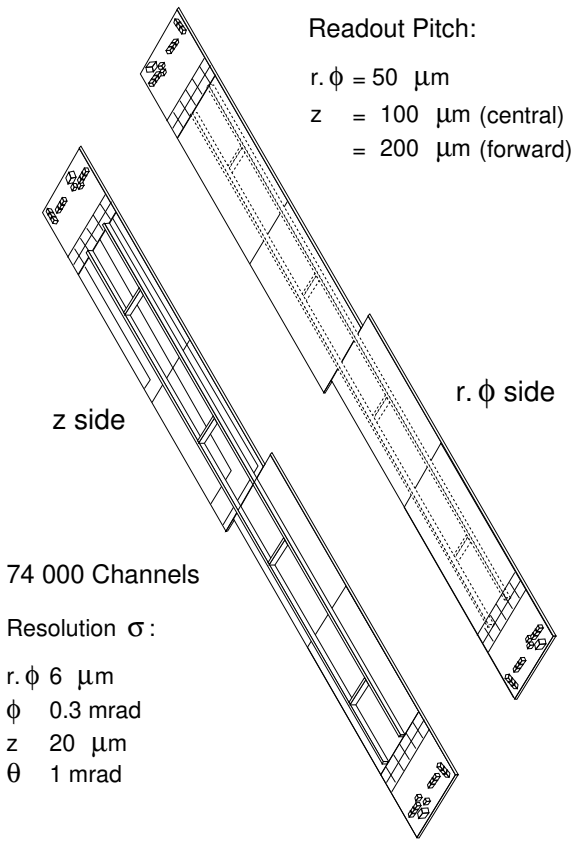

Figure 3.3: An inner SMD ladder. The r $-$ ϕ side and the r $-$ z side are shown.

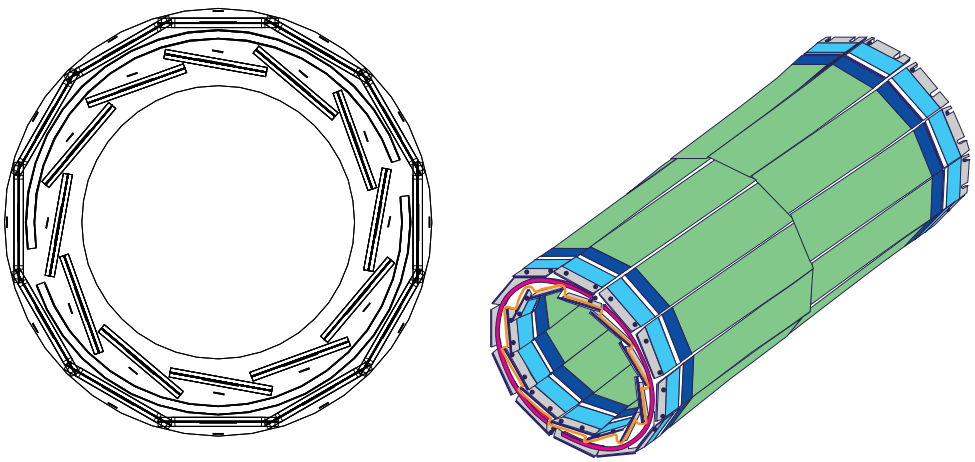

Figure 3.4: A perspective and a front-end view of the SMD.

The Time Expansion Chamber

The Time Expansion Chamber (TEC) is a high resolution drift chamber with an average single wire resolution of 50 μm and a double track resolution of 650 μm in $r - \phi$. It is built as a cylindrical structure around the beam line (Figure 3.5). The TEC is subdivided

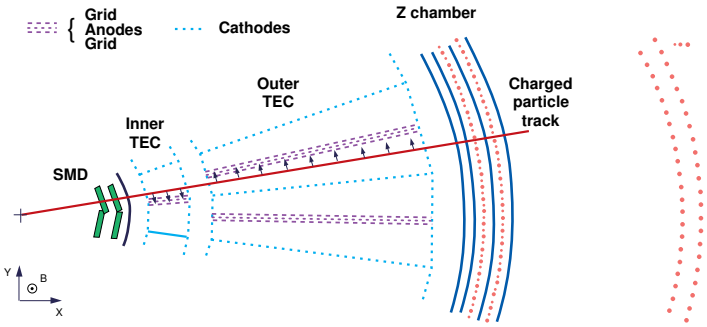

Figure 3.5: The $r - \phi$ view of the central tracker.

into two parts. The inner region consists of 12 sectors with 8 anode wires each. The outer region consists of 24 sectors with 54 anode wires each. The total length of the TEC is 126 cm with a sensitive length of 98 cm. The diameter for the inner and the outer region is 17 cm and 93.7 cm respectively.
The chamber works with a low diffusion gas mixture of 80% of CO_2 and 20% of iso-butane at a pressure of 1.2 bar(abs). This provides a low drift velocity of 6 μm/ns. The drift region has a low and homogeneous electric field whereas the amplification or detection region has a high electric field (Figure 3.6). These regions are separated by grid wire planes at zero potential. The anode wires alternate with the focus wires.

The Z-Chamber

The Z-Chamber consists of two thin cylindrical multiwire proportional chambers with cathode strip readout. It covers a polar angle range between 42° and 138°. The two chambers contain two cathode layers each (Figure 3.7). Each layer consists of 240 strips. In both chambers one of the layers runs perpendicular to the beam axis (z-direction) while the other runs at ±69° for the inner and for the outer chamber respectively. The gas mixture consists of 80% Argon, 16% CO_2 and 4% iso-butane. The resolution varies depending on the polar angle. At $\cos\theta = 0$ it is 200 μm whereas at $|\cos\theta| = 0.74$ it is 1000 μm.

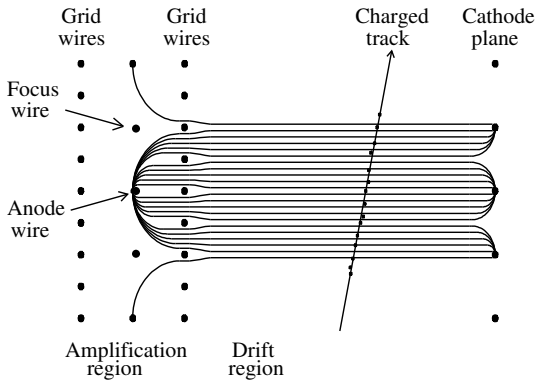

Figure 3.6: The shape of the electric fields in the TEC with a charged particle passing through.

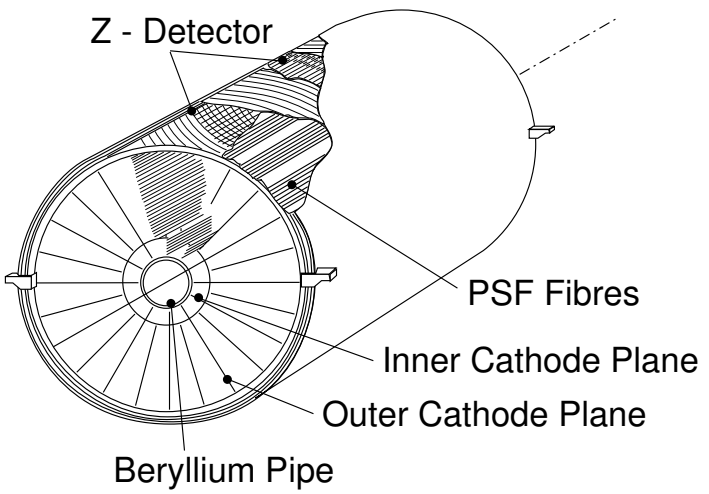

Figure 3.7: Perspective view on the Z-Chamber surrounding the other parts of the central tracker.

3.3.3 The Electromagnetic Calorimeter (BGO)

The electromagnetic calorimeter allows for measurement, with precise energy and spatial resolution, of electrons and photons in the range of 100 MeV up to 100 GeV (Figure 3.8). It is subdivided into two parts, the barrel and the endcaps. The detector consists of bismuth germanium oxide ($Bi_4Ge_3O_{12}$) crystals (BGO) pointing to the interaction region. There are 7680 crystals in the barrel and 1527 crystals in each of the endcaps. The

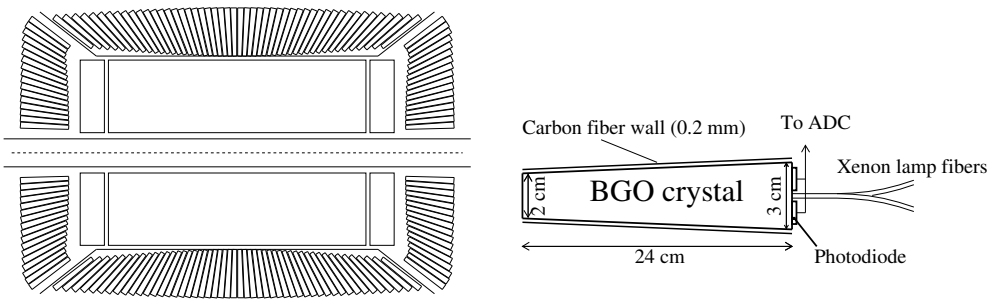

Figure 3.8: Side view on the BGO and a detailed description of one of the crystals.

barrel covers a polar angle region of $42^o < \theta < 138^o$ whereas the endcaps cover a region of $11.6^o < \theta < 38^o$ and $\pi - 11.6^o < \theta < \pi - 38^o$. Each crystal is 24 cm long with a front face of $2{\times}2$ cm^2 and a rear face of $3{\times}3$ cm^2. The polished crystals are coated with a 40 to 50 μm thick layer of high reflectivity paint to obtain a nearly uniform light collection efficiency. The energy resolution is 5% at 100 MeV and about 1.4% at high energies. The spatial resolution is better than 2 mm. A typical shower shape of a photon/electron and hadron can be seen in Figure 3.9. The height corresponds to the amount of energy deposited in the crystal.

3.3.4 The Scintillation Counters

The scintillation counter system is located between the electromagnetic and the hadronic calorimeter. It consists of 30 single plastic scintillators. The polar and azimuthal angles cover $|\cos\theta| < 0.83$ and 93% of 2π respectively. The scintillator hit multiplicity is used to trigger hadronic events. Furthermore, it records the particle's time-of-flight to distinguish dimuon events from cosmic ray background. The time difference between opposite scintillation counters is greater than 4 ns for cosmic muons whereas it is zero for muon pairs.

3.3.5 The Hadron Calorimeter

The hadron calorimeter modules consist of depleted uranium sheets interleaved with multiwire proportional chamber planes. It is subdivided into a barrel and an endcap part. The barrel covers the central polar angle region of $35^o < \theta < 145^o$. This calorimeter acts as a filter as well as a calorimeter. The barrel part has modular structure and contains 9 rings with 16 modules each.
The endcaps cover a polar angle region of $5.5^o < \theta < 35^o$ and $145^o < \theta < 174.5^o$. Each endcap consists of three rings; an inner ring and two outer rings containing 12 modules (Figure 3.10). The cathode read-out pads are grouped to form read-out towers. One tower

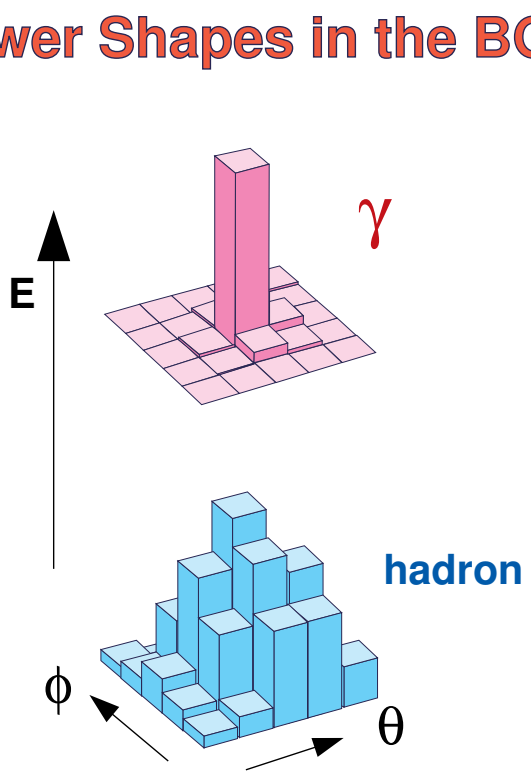

Figure 3.9: BGO shower for a photon/electron and a hadron.

covers 2° in θ and ϕ respectively. Particles originating from the interaction point have to traverse 6 to 7 nuclear absorption lengths depending on the polar angle. A muon filter is installed on the inside wall of the support tube adding an additional nuclear absorption length to prevent secondary particles produced in the hadron calorimeter from entering the muon chambers.
The jet energy resolution of this subdetector is $(55/\sqrt{\mathrm{E}}+8)\%$ where E is measured in GeV. The angular resolution is about 2.5°.

3.3.6 The Muon Chambers

The muon chambers are the outermost part of the L3 detector, surrounding all other subdetectors. They are designed to measure precisely the momentum for muons coming from e^+e^-annihilations. They consist of barrel and endcaps covering a polar angle range of $44° < \theta < 136°$ for the barrel and $24° < \theta < 44°$ and $136° < \theta < 156°$ for the endcaps. The barrel is subdivided into two halves with a gap at $z = 0$. Each half consists of eight parts (octants). The octants contain three layers of drift chambers (P-chambers); two chambers in the outer layer (MO) with 16 signal wires, two chambers in the middle layer (MM) with 24 signal wires and 1 chamber in the inner layer (MI) with 16 signal wires

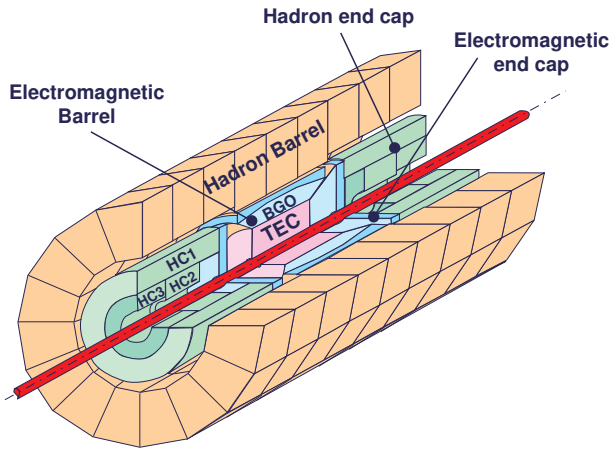

Figure 3.10: A perspective view on the hadron calorimeter. One can see the 9 rings with 16 modules each for the barrel and the three rings (2 inner and 1 outer ring) of the endcaps. Furthermore one sees the position relative to the other subdetectors described above.

each (Figure 3.11). In addition to the signal wires, every P-chamber contains field shaping wires and guard wires. Drift chambers are installed, covering the top and and the bottom

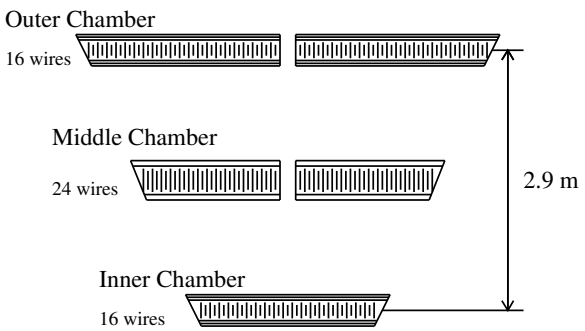

Figure 3.11: The P-chamber structure in the octants.

of MO and MI respectively, to measure the z coordinate along the beam. The single wire resolution has been measured to be better than 200 μm. Taking this into account for the sagitta measurement of the muon track in the bending plane, this gives a momentum resolution $\Delta p_T/p_T$ of about 2.5% at $p = 45$ GeV which is close to the design resolution.

3.3.7 The Luminosity Monitor

The luminosity monitor consists of two electromagnetic calorimeters and two silicon track detectors situated symmetrically on either side of the interaction point (Figure 3.12). The polar angle coverage is $24.93\text{mrad} < \theta < 69.94\text{mrad}$. Its calorimetric part consists of 304 BGO crystals each. Every crystal is read out by a photodiode. The precise measurement of the luminosity is described in chapter 4.

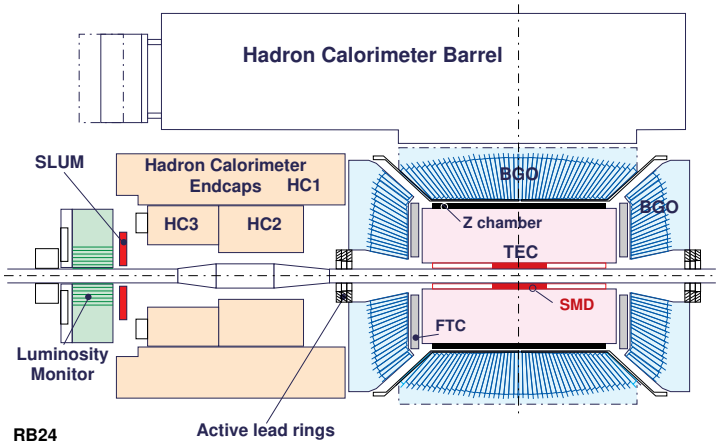

Figure 3.12: One part of the luminosity monitor. SLUM is the silicon track detector.

3.3.8 The Trigger System

The L3 trigger system is subdivided into three levels to distinguish physics events from background events like beam-gas or beam-wall reactions or detector noise.

- **Trigger level-1:** The level-1 trigger is based on five subdetector triggers: the TEC trigger, the scintillator trigger, the calorimetric triggers (electromagnetic and hadron calorimeter), the luminosity trigger and the muon trigger. Each is gated by the beam crossing signal ($\approx 1.7\mu$s before the electron and the positron bunches collide).
  - **Energy Trigger:** energy deposition of at least 10 GeV in the BGO or more than 15 GeV in the BGO and the barrel of the HCAL or more than 20 GeV in both calorimeters (barrel and/or endcaps)
  - **TEC trigger:** at least two tracks in the TEC with a transverse momentum of more than 0.15 GeV and $\phi(\text{track1}, \text{track2}) \geq 45^{\text{o}}$
  - **Scintillator trigger:** at least five scintillation counters out of thirty counters in total must give a result within $\pm$15ns w.r.t. the beam crossing signal

  - **Muon trigger:** one muon with more than 1.5 GeV transverse momentum or two muons.
  - **Luminosity trigger:** energy depositions in the luminosity monitor

- **Trigger level-2**: On a positive result from one of these five the event is considered for the next trigger level otherwise it is rejected. The level-2 trigger further reduces the amount of background events collected by the level-1 trigger. An event with two or more positive results from subdetectors of the level-1 trigger is accepted at the level-2 trigger. The level-2 trigger has a larger dead time to forward all input to an event builder memory that provides first rough information of the polar and azimuthal angle from the energy depositions in the calorimeters. Most of beam-gas or beam-wall reactions are rejected at this level.
- **Trigger level-3**: The level-3 trigger applies criteria from the complete digital information of the event. Each event has to pass more stringent cuts on the subdetector trigger information. Events with multiple positive trigger decisions on trigger level-1 or luminosity trigger are then written on tape.

Chapter 4

The Luminosity Measurement

The accurate measurement of the integrated luminosity $\mathcal{L}$ is crucial for precise cross section determinations. In principle, the integrated luminosity can either be calculated from machine specific parameters or measured by an experimental setup. The basic principles and the measurement of the integrated luminosity are described in the following chapter.

4.1 Basic Principles

The interaction rate of electrons and positrons in the detector, is related to the cross section by the luminosity. The luminosity is the collision rate of particles at the interaction point and is determined by technical features of the machine. For a collider experiment like LEP, the luminosity is calculated the following way:

$$\mathrm{L} = \frac{\mathrm{N_{e^+} N_{e^-} n_b f}}{4\pi\sigma_\mathrm{x}\sigma_\mathrm{y}}. \tag{4.1}$$

$\mathrm{N_{e^+}} \approx 10^{11}$ and $\mathrm{N_{e^-}} \approx 10^{11}$ are the number of positrons and electrons per bunch, $\mathrm{n_b} = 4$ is the number of bunches, f is the frequency of the particles circulating in the collider ($\mathrm{f} \approx 11.4$ kHz) and σ_x and σ_y ($\sigma_\mathrm{x} \approx 25\mu\mathrm{m}, \sigma_\mathrm{y} \approx 150\mu\mathrm{m}$) are the average sizes of the beam in x and y, assuming complete overlap with Gaussian beam profiles.
The specific luminosity L is a function of time and integrated over a time interval it is called integrated luminosity.

$$\mathcal{L} = \int \mathrm{L(t)dt} \tag{4.2}$$

However, for a precise calculation neither the average size of the beam and the complete overlap nor the number of particles per bunch is known with sufficient accuracy, i.e., on a permille level.

4.2 Measurement of the Integrated Luminosity

The integrated luminosity is also given by:

$$\mathcal{L} = \frac{\mathrm{N} - \mathrm{N_{Bkg}}}{\epsilon\sigma}, \tag{4.3}$$

where N is the number of collected data events from a certain process, $\mathrm{N_{Bkg}}$ the number background events of unwanted processes, ϵ is the selection efficiency and σ is the cross section of this process. At LEP the process of low angle Bhabha scattering $\mathrm{e^+e^-} \rightarrow \mathrm{e^+e^-}$ is used as a reference process to obtain the integrated luminosity. The polar scattering angle is of the order of 30 to 60 mrad [58]. These events are collected with the luminosity monitor described in subsection 3.3.7 and the cross section is calculated with the Monte Carlo program BHLUMI [59]. The usage of low angle Bhabha scattering has four basically advantages:

- the process is completely dominated by t-channel photon exchange and therefore is almost a pure QED process; contributions resulting from Z boson exchange are negligible small
- it is a high statistics process, so that the resulting statistical uncertainty propagated on the integrated luminosity is small
- the calculation of higher order terms in the perturbation theory provides only small, precisely calculable contributions [60]
- possible contributions of new physics phenomena are orders of magnitude smaller than the systematic error due to higher order terms.

The differential cross section of Bhabha scattering at small angles, Θ is:

$$\frac{\mathrm{d}\sigma}{\mathrm{d}\Theta} \approx \frac{32\pi\alpha^2}{\mathrm{s}}\frac{1}{\Theta^3}, \tag{4.4}$$

so that it becomes dominant at low scattering angles.
The t-channel exchange of bosons at low angles is characterised by low momentum transfer between the scattered particles. Hence, the exchange of virtual heavy bosons is suppressed due to their mass. Essentially, cross section measurements of processes used to search for new phenomena depend on the integrated luminosity. If an integrated luminosity is taken into account, that is affected by those phenomena themselves, it might scale the measured cross section down to the Standard Model prediction. Hence, a wrongly determined integrated luminosity prevents *a priori* the discovery of new effects.
Taking all this into account, the measurement of the integrated luminosity provides results at permille level accuracy. In Table 4.1 the energies and integrated luminosities analysed are listed together with total errors.

$\sqrt{s}$(GeV)	$\mathcal{L}_{\rm int}(\rm pb^{-1})$
191.6	29.719 ± 0.048
195.5	83.689 ± 0.082
199.5	83.314 ± 0.084
201.7	37.007 ± 0.056
205.2	76.298 ± 0.082
206.7	139.129 ± 0.137

Table 4.1: The centre–of–mass energies and integrated luminosities with their total errors that have been used for this analysis.

Chapter 5

Monte Carlo Event Simulation and Data Reconstruction

At LEP II centre–of–mass energies exist a vast variety of physics processes resulting from e^+e^-annihilations. However, only the fraction of events with final state pair-produced quarks are investigated in the presented analysis. These are considered to be the signal events. Other processes may cause a similar event shape in the detector and cannot necessarily be separated from the signal events. In order to understand which kinds of events may be contained in our data, we need to simulate them. This is described in the following.

5.1 The General Scheme

The reconstruction of events provides the necessary information such as the number of charged tracks (multiplicity), number of energy clusters in the BGO and the HCAL and the number of jets (for jet-clustering see appendix A).
The reconstructed events cannot *a priori* be distinguished as signal events or background events that have a similar event shape as seen in the detector (see Figure 5.1).

5.2 The Signal Process

The signal event process for this analysis are events with pair-produced quarks in the final state. The process $q\bar{q}(\gamma)$(Figure 5.2) describes s-channel photon and Z boson exchange where an electron and positron annihilate to a virtual Z boson or virtual photon and produce a pair of quarks. The signal process appears as events with a few jets per event,

due to gluon radiation and fragmentation in the final state. The jets stemming from gluon radiation are mostly close to the quark jets. The events can be forced into two jets. The signal events are well balanced in momentum and have a high fraction of energy deposited in the detector and the two jets point into opposite directions.

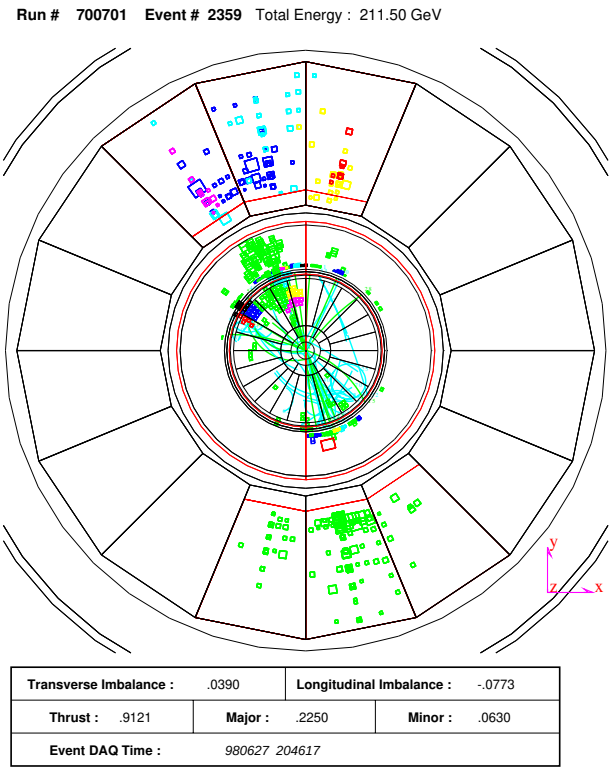

Figure 5.1: A dijet event in the L3 detector. A view along the beamline with the cross section of the L3 detector is shown. The particle tracks and energy depositions in the different subdetector shells are recognisable.

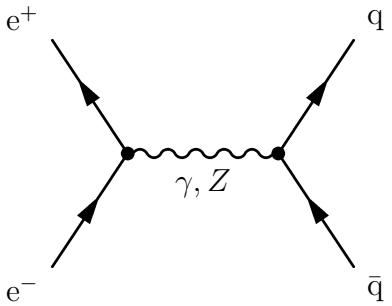

Figure 5.2: The signal event process $e^+e^- \rightarrow q\bar{q}(\gamma)$.

5.2.1 Low Energy Signal Events

A fraction of events is treated as low energy background. These events are based on the process $e^+e^- \rightarrow q\bar{q}$, but are at low energy due to initial state radiation (ISR) as described in subsection 2.6. In order to measure σ_{had}, R_b and A_{fb}^b at high centre–of–mass energies these events have to be distinguished and to be treated correctly. The signal events with initial state radiation are further on called ISR-background.

5.3 The Background Processes

Other processes with a similar event topology as seen in the detector are considered to be background processes. In Figure 5.3 a set of first order diagrams of contributing background processes are shown. The corresponding processes are:

- $e^+e^- \rightarrow W^+W^-(\gamma)$
- $e^+e^- \rightarrow ZZ$
- $e^+e^- \rightarrow Zee$
- $e^+e^- \rightarrow We\nu$
- $e^+e^- \rightarrow \tau^+\tau^-$
- $e^+e^- \rightarrow e^+e^-$hadrons.

The listed processes either produce one or two W bosons or one or two Z bosons, where at least one of them decays hadronically. In case of $e^+e^- \rightarrow \tau^+\tau^-$, a pair of τ leptons is produced. They decay and often produce a pair of low multiplicity jets. In the process $e^+e^- \rightarrow e^+e^-$hadrons the initial state electron and positron interact via a virtual photon system and produce two low energy quark jets.
The production cross sections for the background events are different from the cross section of the signal process. The production cross sections for the signal and the background processes are listed in Table 5.1.

Process	192 GeV	196 GeV	200 GeV	202 GeV	205 GeV	207 GeV
$e^+e^- \rightarrow q\bar{q}(\gamma)$	95.71	90.86	86.24	84.33	82.38	80.39
$e^+e^- \rightarrow ZZ$	1.14	1.19	1.26	1.28	1.32	1.33
$e^+e^- \rightarrow Zee$	3.40	3.55	3.52	3.54	3.58	3.61
$e^+e^- \rightarrow W^+W^-(\gamma)$	16.76	17.04	17.25	17.31	17.50	17.53
$e^+e^- \rightarrow \tau^+\tau^-$	7.69	7.46	7.35	7.11	6.69	6.22
$e^+e^- \rightarrow We\nu$	0.74	0.77	0.78	0.79	0.81	0.81
$e^+e^- \rightarrow e^+e^-$hadrons	$1.57 \cdot 10^4$	$1.59 \cdot 10^4$	$1.60 \cdot 10^4$	$1.61 \cdot 10^4$	$1.63 \cdot 10^4$	$1.64 \cdot 10^4$

Table 5.1: The production cross sections, $\sigma_{\text{gen}}^{\text{prod}}$, of the simulated processes given in pico barn.

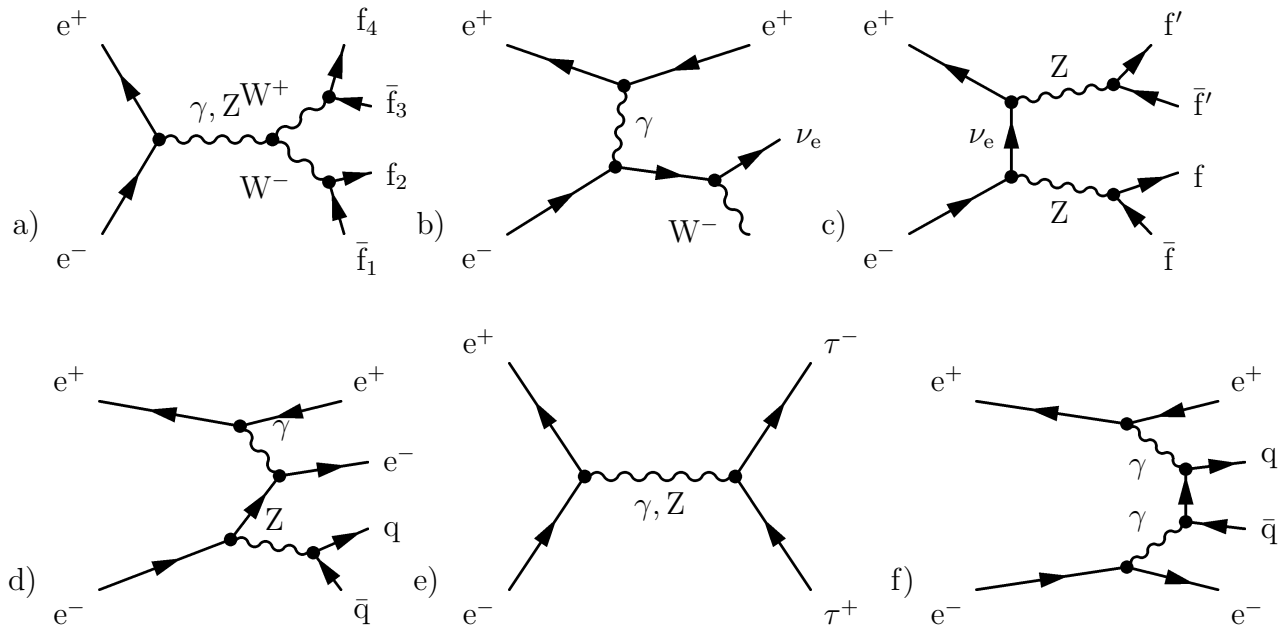

Figure 5.3: Example diagrams for the listed background processes are shown. a) is a corresponding diagram for the process $e^+e^- \to W^+W^-(\gamma)$. The process $e^+e^- \to We\nu$ is among others described by b), where the W boson decays hadronically. In c) the process $e^+e^- \to ZZ$ is shown, where at least one of the pair-produced Z bosons decays hadronically. In d) a Z boson is radiated and decays hadronically. e) shows the τ pair-production, where τ leptons decay and produce two low multiplicity jets. The process $e^+e^- \to e^+e^-$hadrons yields two high multiplicity quark jets, that are produced back-to-back in the rϕ-plane but not at full energy.

5.4 The Event Simulation and Reconstruction

The simulation of events is carried out by Monte Carlo event generators. Different generator programs are specialised to generate different kinds of processes. After the simulation is finished, we have the 4-momentum vector for every particle involved in the process. The second step is to simulate the detector response for every particle like showering in the detector, energy loss, multiple scattering effects and interactions with the magnetic field. These informations are provided by the programs GEANT [61] and GHEISHA [62] for every subdetector. The raw information is then available in the same format as for the real data. Now the reconstruction of the generated information is carried out with the detector response, the information of detector inefficiencies and imperfections as there are dead wires, or time dependent efficiency losses in different regions of the subdetectors. At the end of this procedure one obtains realistic generated events to be comparable with real data events.

5.4.1 Processes in this Analysis

The procedure described above is carried out for all, signal and background, physics process. The corresponding Monte Carlo event generators for signal and background processes are listed in Table 5.2. The signal event generator KK2F is using the string fragmentation as described in section 2.3.

Process	MC Generator
$e^+e^- \rightarrow q\bar{q}(\gamma)$	KK2F [63]
$e^+e^- \rightarrow ZZ$	PYTHIA [64]
$e^+e^- \rightarrow Zee$	PYTHIA
$e^+e^- \rightarrow \tau^+\tau^-$	KORALZ [65]
$e^+e^- \rightarrow e^+e^-$hadrons	PHOJET [66]
$e^+e^- \rightarrow We\nu$	EXCALIBUR [67]
$e^+e^- \rightarrow W^+W^-(\gamma)$	KORALW [68]

Table 5.2: The processes and corresponding Monte Carlo event generators considered in this analysis.

Chapter 6

The Event Selection

The measurement of σ_{had} and R_b requires to select hadronic events and to distinguish events of the process $e^+e^- \to b\bar{b}$ among them. In this chapter the selection of hadronic events at high centre–of–mass energies will be described. The data are collected with the L3 detector (see chapter 3) at centre–of–mass energies from 191.6 GeV to 206.7 GeV.
A set of discriminating variables is established to separate hadronic events from ISR-background events (see subsection 5.2.1) and background events from other processes as described in section 5.3.
In order to distinguish events of the process $e^+e^- \to b\bar{b}$, a procedure called B-tag is set up, exploiting the three-dimensional geometrical information of each event.

6.1 Selection of Hadronic Events at High Energies

Events with hadronic final states produce numerous tracks of charged particles in the central track detector (N_{Track}) and calorimetric clusters ($N_{Cluster}$) in both the electromagnetic and the hadron calorimeters. The selection of hadronic events requires therefore events with high multiplicity. This requirement rejects events with low multiplicity, e.g. from the process $e^+e^- \to \tau^+\tau^-$.
The quarks in the final state fragment and are forced into two jets (see appendix A). These jets must point into opposite directions in the detector and must carry a high fraction of the nominal beam energy. In case of ISR-background events and background events, the jets either do not point into opposite directions and/or have less energy deposited in the detector. The variables to select hadronic events are defined as:

- the effective centre–of–mass energy, $\sqrt{s'}$
- the energy deposited in the calorimeters (called visible energy), E_{vis}
- the collinearity.

The effective centre–of–mass energy, $\sqrt{s'}$:
Due to initial state bremsstrahlung, the electrons and positrons collide at an effective centre–of–mass energy, $\sqrt{s'}$, given in equation 2.84, which is below the nominal centre–of–mass,

$\sqrt{s}$. Most radiated photons escape along the beampipe and remain undetected. Nevertheless, the effective centre–of–mass energy can be calculated using the angular information of the jets. When either one initial state lepton radiates a photon, the observed quark pair is not produced in the rest frame of the virtual photon or Z boson and the jets do not point into opposite directions. Due to momentum conservation a fraction of momentum and energy is carried away by the radiated photon. The photon energy is calculated taking the polar angles of the jets into account:

$$E_\gamma = \sqrt{s} \cdot \frac{|\sin(\Theta_{j1} + \Theta_{j2})|}{\sin\Theta_{j1} + \sin\Theta_{j2} + |\sin(\Theta_{j1} + \Theta_{j2})|}, \tag{6.1}$$

Θ_{j1} and Θ_{j2} are the polar angles of the two quark jets. If photons from initial state radiation are detected, they are taken into account for the calculation of s', in particular for the calculation of $M_{\gamma\gamma}$ (see equation 2.84). In Figure 6.1 the $\sqrt{s'}$ distribution normalised to the nominal centre–of–mass energy, $\sqrt{s}$, is shown. The excess of generated events in the range of $0.1\sqrt{s} \leq \sqrt{s'} \leq 0.4\sqrt{s}$ is caused by $e^+e^- \rightarrow e^+e^-$hadrons events generated by the PHOJET generator. In a signal event where both electron and positron radiate a

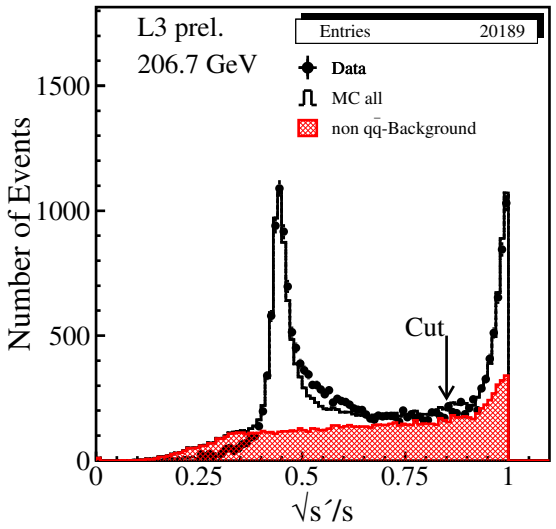

Figure 6.1: The distribution of s' shown for $\sqrt{s} = 206.7$ GeV. The black dots represent the data, the open histogram represents the generated signal events and the hatched histogram represents the generated background events. The selection criterion $\sqrt{s'} > 0.85\sqrt{s}$ is indicated by the arrow.

photon with about the same absolute value for energy and momentum but in opposite directions, the formed jets point into opposite directions, but the collision takes place at lower centre–of–mass energies.
This is also the case for the background process $e^+e^- \rightarrow e^+e^-$hadrons (see section 5.3).

The initial state electron and positron interact via a system of virtual photons, the photon system forms a pair of quarks and the initial state electron and positron escape undetected along the beampipe. This kind of event has less energy deposited in the calorimeters.

The energy deposition in the calorimeters, E_{vis}:

Hence, the energy deposited in both the electromagnetic and the hadron calorimeter is another variable to separate high energy signal events from low energy signal events and from background events. This variable is also called 'visible energy', E_{vis} (Figure 6.2). The excess of generated events in the range of $E_{vis}/\sqrt{s} \leq 0.3$ is again caused by $e^+e^- \rightarrow e^+e^-$hadrons events as explained above. Apart from the selection sample defined

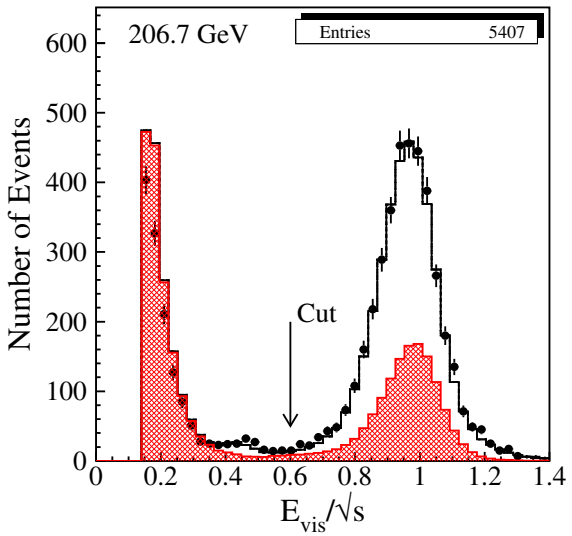

Figure 6.2: The distribution of the visible energy is shown for $\sqrt{s} = 206.7$ GeV. The visible energy normalised to the centre–of–mass energy, $\sqrt{s}$, after the cut on on the effective centre–of–mass energy, s′. The selection criterion $E_{vis} > 0.6\sqrt{s}$ is indicated by the arrow.

by $\sqrt{s'}$ and E_{vis}, the information of the spatial angle between the two jets is exploited.

The collinearity:

The corresponding variable to describe the balance, is the angle in three-dimensional space between the two jets, called collinearity (Figure 6.3). The collinearity enables direct access to the information whether the jets point into opposite directions. The angular range runs from zero to π. For high energy hadron events the collinearity should have a value close to π.

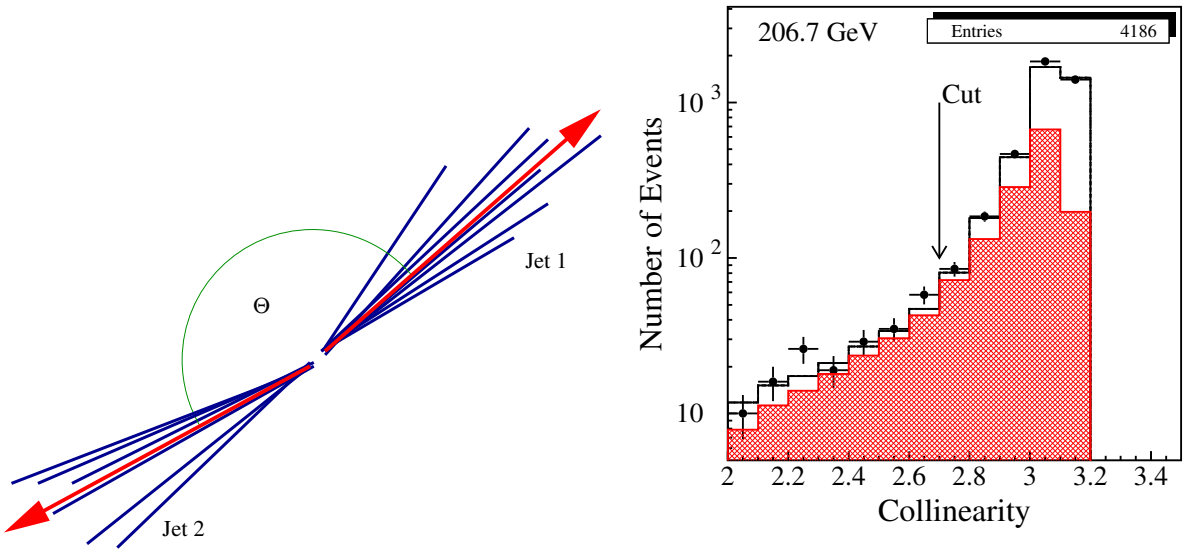

Figure 6.3: The collinearity between two jets. The left picture shows the jets as seen in the detector with the collinearity for this event. The right picture shows the collinearity distribution for $\sqrt{s} = 206.7$ GeV for data events (black dots) compared to generated events (histogram). The open histogram are the signal events and the hatched histogram are the background events. The selection criterion Collinearity > 2.7 is indicated by the arrow.

6.2 Treatment of Low Energy Background

In subsection 5.2.1 the low energy background is described as signal events that are not produced at the nominal centre–of–mass energy. Although, the selection of high energy events is carried out using especially the criteria of for the effective centre–of–mass energy and the visible energy, ISR-background events remain.
As described in section 5.4, the four-momenta of each generated particle at the generation level is obtained. The four-momenta of the particles, in particular of generated initial state radiation photons, are used to calculate the effective centre–of–mass energy according to equation 2.84. In order to distinguish the generated effective centre–of–mass from the reconstructed effective centre–of–mass energy as described in section 6.1, it is called s'_{gen}. The reconstructed effective centre–of–mass energy, s'_{reco}, is reconstructed for the data and the generated events while the generated effective centre–of–mass energy is only calculable for generated events where *a priori* the generated four-momenta of the particles are known.
Both, data events and generated events pass the hadronic event selection given in Table 6.1, where the selection criterion for the reconstructed effective centre–of–mass energy, $\sqrt{s'} = \sqrt{s'_{reco}} > 0.85\sqrt{s}$, is applied. The fraction of generated events, that pass the selection but have a generated effective centre–of–mass energy of $\sqrt{s'_{gen}/s} \leq 0.85$, is used to estimate the number of ISR-background events. This fraction is 9% to 9.8% of the number of generated signal events.

6.3 Results of the Hadronic Event Selection

The criteria of the event selection as described in section 6.1 are listed in Table 6.1. The

Criterion	Value
$N_{Cluster}$	> 10
N_{Track}	> 4
$\sqrt{s'/s}$	> 0.85
$E_{vis}/\sqrt{s}$	> 0.60
collinearity	> 2.7

Table 6.1: Selection criteria for high energy hadronic events as discussed in the text.

number of generated events is at least ten times larger than the number of recorded data events. Hence, in order to be able to compare the number of selected events from data and the number of expected events from the simulation, the number of generated events is normalised to the number of selected events by the production cross section, listed in Table 5.1, and the integrated luminosity, listed in Table 4.1,

$$N_{exp} = \varepsilon_{exp} \cdot \mathcal{L} \cdot \sigma_{gen}^{prod}, \tag{6.2}$$

where exp = signal, background, ISR − background stands for signal, background and ISR-background events. ε_{exp} denotes the selection efficiency for signal, background and ISR-background events, respectively. This efficiency is calculated according to appendix B by:

$$n = N_{exp}^{gen}(\text{after}) \tag{6.3}$$

$$N = N_{exp}^{gen}(\text{before}) \tag{6.4}$$

$$\varepsilon_{exp} = \frac{n+1}{N+2} \pm \sqrt{\frac{(n+1)(N-n+1)}{(N+3)(N+2)^2}}. \tag{6.5}$$

The notation 'before' and 'after' refers to the selection criteria for the visible energy and the collinearity as listed in Table 6.1:

- **before:** no selection applied
- **after:** selection criteria in Table 6.1 applied

The numbers of generated background events before and after the selection and the calculated selection efficiency of background events, ε_{bkg}, are listed in Table 6.2. Taking the numbers of generated background events that are analysed, $N_{bkg}^{gen}(\text{before})$, the selection efficiencies of background events, ε_{bkg}, both listed in Table 6.2, the integrated luminosity

listed in Table 4.1 and the production cross section listed in Table 5.1 one obtains according to equation 6.2 the background composition listed in Table 6.6.
The calculation of the selection efficiency of ISR-background events is carried out the same way. The numbers of generated signal events before the selection and generated ISR-background events after the selection and the calculated selection efficiency of ISR-background events, $\varepsilon_{\mathrm{ISR}}$, are listed in Table 6.3. Taking the numbers of generated signal events that are analysed, $\mathrm{N}^{\mathrm{gen}}_{\mathrm{signal}}$(before), the selection efficiencies for ISR-background events, $\varepsilon_{\mathrm{ISR}}$, both listed in Table 6.3, the integrated luminosity listed in Table 4.1 and the production cross section listed in Table 5.1 one obtains according to equation 6.2 the ISR-background events normalised to the data as listed in Table 6.5.
After the selection is carried out, approximately 30% of the entire sample of selected events are background events from other processes. The sample of generated events of the signal process, $\mathrm{e^+e^-} \rightarrow$ hadrons, contains 9.0% to 9.8% ISR-background events (see Table 6.5 and 6.6). The highest fraction of background events comes from the process $\mathrm{e^+e^-} \rightarrow \mathrm{W^+W^-}(\gamma)$. The other background processes give only minor contributions. The number of selected events in data compared to the number of expected generated events, are listed in Table 6.4. The number of background events and ISR-background events are compared to the number of selected events in data and listed in Table 6.5. The composition of the entire sample according to the simulation is listed in Table 6.6. The composition of the selected signal events and the selected ISR-background events in terms of different quark flavours is listed unnormalised in Table 6.7 and Table 6.8.

$\sqrt{s}$(GeV)	Process	N_{bkg}^{gen}(before)	N_{bkg}^{gen}(after)	$\varepsilon_{bkg} \pm \Delta\varepsilon_{bkg}$
191.6	$e^+e^- \to ZZ$	4998	2699	0.540 ± 0.007
	$e^+e^- \to Zee$	9975	482	0.048 ± 0.002
	$e^+e^- \to W^+W^-(\gamma)$	249566	125913	0.505 ± 0.001
	$e^+e^- \to \tau^+\tau^-$	3724	36	0.010 ± 0.002
	$e^+e^- \to We\nu$	99362	16789	0.169 ± 0.001
	$e^+e^- \to e^+e^-$hadrons	1116500	12	$1.2 \cdot 10^{-5} \pm 3.2 \cdot 10^{-6}$
195.5	$e^+e^- \to ZZ$	50000	27177	0.544 ± 0.002
	$e^+e^- \to Zee$	36000	1932	0.054 ± 0.001
	$e^+e^- \to W^+W^-(\gamma)$	489160	245941	0.5030 ± 0.0007
	$e^+e^- \to \tau^+\tau^-$	3755	30	0.008 ± 0.002
	$e^+e^- \to We\nu$	100000	16585	0.166 ± 0.001
	$e^+e^- \to e^+e^-$hadrons	1116500	12	$1.2 \cdot 10^{-5} \pm 3.2 \cdot 10^{-6}$
199.5	$e^+e^- \to ZZ$	9946	5223	0.525 ± 0.005
	$e^+e^- \to Zee$	19909	1026	0.052 ± 0.002
	$e^+e^- \to W^+W^-(\gamma)$	466900	230792	0.4943 ± 0.0007
	$e^+e^- \to \tau^+\tau^-$	4968	48	0.010 ± 0.001
	$e^+e^- \to We\nu$	100000	16492	0.165 ± 0.001
	$e^+e^- \to e^+e^-$hadrons	1404200	7	$5.7 \cdot 10^{-6} \pm 2.1 \cdot 10^{-6}$
201.7	$e^+e^- \to ZZ$	5000	2736	0.547 ± 0.007
	$e^+e^- \to Zee$	10000	558	0.056 ± 0.002
	$e^+e^- \to W^+W^-(\gamma)$	287555	143360	0.4990 ± 0.0009
	$e^+e^- \to \tau^+\tau^-$	5000	52	0.011 ± 0.001
	$e^+e^- \to We\nu$	99515	16671	0.168 ± 0.001
	$e^+e^- \to e^+e^-$hadrons	1404200	7	$5.7 \cdot 10^{-6} \pm 2.1 \cdot 10^{-6}$
205.2	$e^+e^- \to ZZ$	9948	5309	0.534 ± 0.005
	$e^+e^- \to Zee$	20000	961	0.048 ± 0.002
	$e^+e^- \to W^+W^-(\gamma)$	498391	246517	0.4946 ± 0.0007
	$e^+e^- \to \tau^+\tau^-$	4994	56	0.011 ± 0.002
	$e^+e^- \to We\nu$	39053	6340	0.162 ± 0.002
	$e^+e^- \to e^+e^-$hadrons	6998590	31	$4.6 \cdot 10^{-6} \pm 8.0 \cdot 10^{-7}$
206.7	$e^+e^- \to ZZ$	125791	67466	0.536 ± 0.001
	$e^+e^- \to Zee$	99728	4933	0.0495 ± 0.0007
	$e^+e^- \to W^+W^-(\gamma)$	660013	326686	0.4950 ± 0.0006
	$e^+e^- \to \tau^+\tau^-$	10000	94	0.0095 ± 0.0010
	$e^+e^- \to We\nu$	118652	19428	0.1637 ± 0.0011
	$e^+e^- \to e^+e^-$hadrons	9066498	46	$5.2 \cdot 10^{-6} \pm 8.0 \cdot 10^{-7}$

Table 6.2: N_{bkg}^{gen}(before), is the number of generated background events that are analysed for the listed processes. N_{bkg}^{gen}(after), is the number of generated background events that remain after the selection is carried out described in section 6.1 ε_{bkg}, is the selection efficiency calculated from N_{bkg}^{gen}(before) and N_{bkg}^{gen}(after) according to equation 6.5.

$\sqrt{s}$(GeV)	N^{gen}_{signal}(before)	N^{gen}_{ISR}(after)	$\varepsilon_{ISR} \pm \Delta\varepsilon_{ISR}$
191.6	99516	2257	0.0230 ± 0.0005
195.5	189499	4030	0.0213 ± 0.0003
199.5	193750	3923	0.0203 ± 0.0003
201.7	98750	2042	0.0207 ± 0.0005
205.2	497900	10448	0.0210 ± 0.0002
206.7	1402050	28165	0.0201 ± 0.0001

Table 6.3: N^{gen}_{signal}(before), is the number of generated signal events that are analysed. N^{gen}_{ISR}(after), is the number of generated ISR-background events that remain after the selection is carried out described in section 6.1 ε_{ISR}, is the selection efficiency calculated from N^{gen}_{signal}(before) and N^{gen}_{ISR}(after) according to equation 6.5. The numbers are not normalised to the number of events in the data.

$\sqrt{s}$(GeV)	selected/expected
191.6	949/946.9
195.5	2571/2577.0
199.5	2466/2430.1
201.7	1108/1083.0
205.2	2195/2159.9
206.7	3953/3842.1

Table 6.4: Numbers of high energy events selected from the data and the expected numbers of generated events for the different centre–of–mass energies. The number of expected events is normalised to the number of selected events in data according to equation 6.2.

$\sqrt{s}$(GeV)	N_{sel}	N_{bkg}	N_{ISR}
191.6	949	285.9	64.5
195.5	2571	818.1	161.6
199.5	2466	805.1	145.7
201.7	1108	363.7	64.6
205.2	2199	750.1	132.0
206.7	3953	1366.2	239.2

Table 6.5: The numbers of selected events, background events, ISR-background events are listed. The number of background and ISR-background events are normalised to the number of selected events in data according to equation 6.2.

Process	192 GeV	196 GeV	200 GeV	202 GeV	205 GeV	207 GeV
$e^+e^- \to q\bar{q}(\gamma)$	661.4	1759.1	1626.0	719.8	1410.6	2476.7
$e^+e^- \to ZZ$	18.2	54.2	55.1	25.9	53.8	98.9
$e^+e^- \to Zee$	4.9	15.5	15.1	7.3	13.1	24.8
$e^+e^- \to W^+W^-(\gamma)$	251.5	718.3	710.5	319.4	661.2	1205.0
$e^+e^- \to \tau^+\tau^-$	2.2	5.0	5.9	2.7	5.7	7.6
$e^+e^- \to We\nu$	3.7	10.6	10.8	4.9	10.0	18.6
$e^+e^- \to e^+e^-$hadrons	5.0	14.3	6.7	3.0	5.5	10.5

Table 6.6: The composition of the generated event sample according to the simulation normalised to the number of selected events in the data.

$\sqrt{s}$(GeV)	N_b	N_c	N_{uds}
191.6	4009	5749	13402
195.5	7285	10869	25707
199.5	7314	10949	25645
201.7	3775	5684	13315
205.2	18581	27872	65141
206.7	51445	78604	182275

Table 6.7: The composition of the selected signal events is listed. The numbers are not normalised to the number of events in the data.

$\sqrt{s}$(GeV)	$N_{b,ISR}$	$N_{c,ISR}$	$N_{uds,ISR}$
191.6	456	449	1352
195.5	736	810	2484
199.5	784	813	2326
201.7	411	384	1247
205.2	1874	2186	6388
206.7	5410	6012	18237

Table 6.8: The composition of the selected ISR-background events is listed. The numbers are not normalised to the number of events in the data.

6.4 B-tagging in L3

After the selection of hadronic events at high effective centre–of–mass energies, the events that contain bottom quarks have to be distinguished.
Hadrons containing bottom quarks are characterised by a relatively long lifetime compared to other quark flavours and a large fraction of energy retained from the initial bottom quark. Furthermore, the large mass of hadrons containing bottom quarks results in a smaller boost. The different characteristics are exploited to distinguish hadronic events containing bottom quarks from other hadronic final states. The procedure is called B-tag [69], exploiting these two features:

- the fragmentation of heavy hadrons results in a smaller boost, due to their larger mass
- because of the longer lifetime, it is possible to reconstruct decay vertices.

An example of bottom quark production is shown in Figure 6.4. The incoming electron and positron annihilate and produce a pair of bottom quarks. The decay length of heavy hadrons containing bottom quarks is of the order of 3 millimetres.
The long lifetime and the large mass of heavy hadrons are represented by a significantly

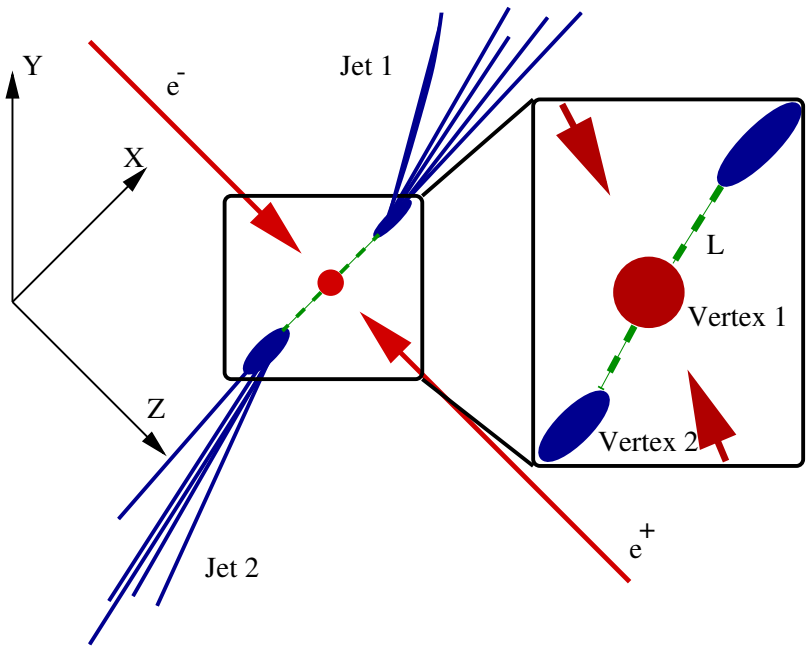

Figure 6.4: The collision of electrons and positrons and the production of a pair of bottom quarks is shown. The innermost part is shown zoomed on the right. The coordinate system of LEP is depicted as reference frame.

longer decay length and a larger average impact parameter as defined in section 6.4.2. The measurement of the decay length and the impact parameter requires the precise

reconstruction of the primary vertex. The primary vertex is the nominal interaction point of the initial state electrons. The reconstruction of the primary vertex is an iterative procedure. Each track of the event is fitted to a common vertex using the beam spot size and position as constraint. The track with the largest deviation is dropped and the procedure is repeated until no track deviates more than a certain threshold. The dropped tracks are used to reconstruct a secondary vertex; the decay vertex. The beam spot size and position are determined to an accuracy of $\mathcal{O}(10\mu\text{m})$ [70]. The high accuracy is obtained due to the high tracking resolution provided by the SMD (see subsection 3.3.1).

6.4.1 Decay Length Significance

The precise determination of the primary vertex and the decay vertex enables a precise measurement of the decay length. The decay length is the spatial distance between the primary and the decay vertex. It is assigned positive if the decay vertex and the associated jet lie in the same hemisphere, otherwise it is assigned negative. The hemispheres are defined by the jet directions and the position of the primary vertex. The decay length is calculated as:

$$\mathrm{L} \;=\; \beta\gamma \mathrm{c}\tau, \tag{6.6}$$

β and γ are the Lorentz boost factors, τ is the lifetime of the hadron and c is the speed of light. Taking the values of $\mathrm{c}\tau$ from Table 2.3 in section 2.3 and multiplying it with the typical boost factors $\beta\gamma = 7$ for B hadrons and $\beta\gamma = 12$ for charmed hadrons, one obtains the decay lengths listed in Table 6.9. The decay length significance, $\mathrm{L}/\sigma_{\mathrm{L}}$, is defined as

Particle	$\mathrm{c}\tau(\mu\text{m})$	$\beta\gamma\mathrm{c}\tau(\text{mm})$
$\mathrm{B}^{\pm}$	495	3.5
B^{0}	468	3.3
$\mathrm{B_s}$	462	3.2
$\mathrm{D}^{\pm}$	317	3.8
D^{0}	124	1.5
$\mathrm{D_s}$	134	1.6

Table 6.9: B hadrons and charmed hadrons and their masses and lifetimes [22]. c, denotes the light-speed.

the ratio of the decay length and its error. The decay length significance of a short-lived hadron fluctuates around zero, whereas for long-lived hadrons it tends to have a positive value.

6.4.2 Impact Parameter Significance

In case no secondary vertex is reconstructed, the impact parameter is used to tag heavy hadrons. The impact parameter is the distance of closest approach between a track and the primary vertex in space. It is assigned positive or negative analogously to the decay length. The impact parameter is characterised by the decay length, L, and the angle, α of the track with respect to the decay length (see Figure 6.5):

$$\delta = \mathrm{L} \sin \alpha. \tag{6.7}$$

Expressing $\sin \alpha$ in the rest frame of the decaying hadron, it obeys the relation

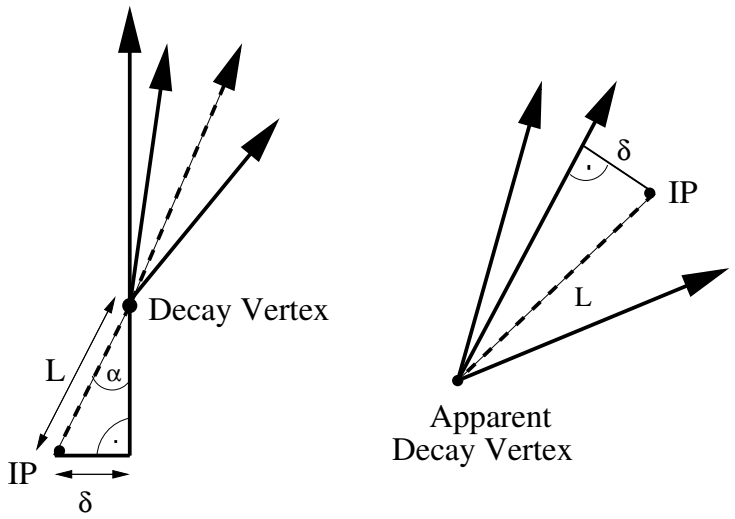

Figure 6.5: The left plot shows a jet where the reconstructed tracks point into the same hemisphere where decay vertex is situated (positive sign). On the right is shown an event where the reconstructed tracks imply that the decay vertex is apparently situated in the other hemisphere (negative sign). IP is the interaction point.

$\sin \alpha = \sin \alpha' / \gamma(1 + \beta \cos \alpha')$ and hence:

$$\delta = \frac{\beta c \tau \sin \alpha'}{1 + \beta \cos \alpha'}. \tag{6.8}$$

The great advantage is that the impact parameter, δ can be measured independently of the decay length L for every track. The impact parameter divided by its error provides the impact parameter significance, δ/σ_δ. The impact parameter significance is used to compute the probability of a track to come from the primary vertex. The distribution of the impact parameter significance is depicted in Figure 6.6. The distribution is asymmetric, caused by heavy hadrons, that tend to have positive values. The probability for a track to originate from the primary vertex, is computed by fitting a function to the part of the distribution, where the impact parameter significance is less than zero. The

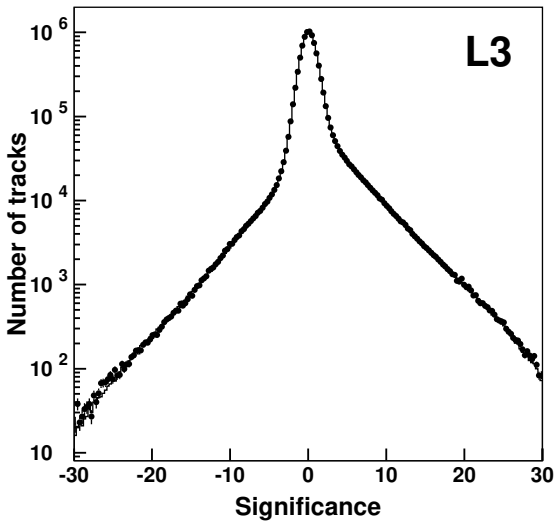

Figure 6.6: The impact parameter significance for tracks.

function obtained from the fit is integrated for every individual track taking its impact parameter significance as lower bound:

$$\begin{aligned} \mathrm{P_i(x)} &= \frac{\int_{\mathrm{x}}^{\infty} \mathrm{R_i(x')dx'}}{\int_{0}^{\infty} \mathrm{R_i(x')dx'}} \\ \mathrm{x} &= \frac{\delta}{\sigma_\delta}. \end{aligned} \tag{6.9}$$

$\mathrm{R_i(x)}$ is the resolution function obtained from the fit and x is the impact parameter significance for each individual track. After computing the probability for every track in the event, the probabilities are combined to an event probability, $\mathrm{P_{event}}$. A possible combination can be defined by $\prod_{\mathrm{i=1}}^{\mathrm{N_{track}}} \mathrm{P_i}$. This combination is highly correlated to the number of tracks per event. An appropriate combination is a modified probability, first proposed by the ALEPH collaboration [71]. The track probability is considered to be a point inside a n-dimensional hypercube with unit volume. The fractional hyper-volume defined by tracks having equal or less differential probability is calculated by:

$$\mathrm{P} = 1 - \int_{\prod_{\mathrm{i=1}}^{\mathrm{N}} \mathrm{x_i}}^{(1,1,\ldots,1)} \mathrm{dx_1 dx_2 \ldots dx_N} \tag{6.10}$$

The complicated multidimensional structure of the integral can be resolved:

$$\mathrm{P} = 1 - \int_{\prod}^{1} \int_{\prod/\mathrm{x_N}}^{1} \int_{\prod/\mathrm{x_N \cdot x_{N-1}}}^{1} \cdots \int_{\prod/\prod_{\mathrm{i=2}}^{\mathrm{N}} \mathrm{x_i}}^{1} \mathrm{dx_1 dx_2 \ldots dx_N} \tag{6.11}$$

In case of a single track (n = 1) the probability is given by $P = P_1$. The product $\prod$ is $\prod = \prod_{i=1}^{N_{track}} P_i$. It can be proven by total induction that the probability of a set of N tracks is consistent with the primary vertex, is given by:

$$P = \prod_{i=1}^{n} P_i \sum_{j=0}^{n-1} \frac{(-\ln \prod_{i=1}^{n} P_i)^j}{j!}. \tag{6.12}$$

P is distributed between zero and one. Events including tracks coming originally from decay vertices, causing a distribution peaking at low values of P. The pseudo-observable finally used is defined by:

$$D = -\log_{10} P \tag{6.13}$$

and further called **discriminant variable**. The individual distribution of events containing bottom quarks and events containing other quark flavours is shown in Figure 6.7. The B-tag has the highest discriminating power to separate events with bottom quarks in the final state from events with other quark flavours. The B-tag procedure is applied to the data and to the generated events, respectively.

6.5 Results of the B-tagging

The events that have a discriminant value, D, larger than a certain threshold value, $D_{threshold}$, are considered as tagged. The threshold value of the discriminant, $D_{threshold} \geq 2.3$, provides a B-purity, P_B, of the tagged events of more than 70%. The reason to choose $D_{threshold} \geq 2.3$ will be given in section 8.1. The B-purity, P_B, is obtained from the generated events by:

$$P_B = \frac{N^t_{b\bar{b}}}{N^t_{b\bar{b}} + N_c + N^t_{uds} + N^t_{bkg}}. \tag{6.14}$$

$N^t_{b\bar{b}}$, N^t_c, N^t_{uds} and N^t_{bkg} are the number of tagged $b\bar{b}$ events, the number of tagged charm quark events, the number of tagged light quark events and the number of tagged background events as listed in Table 6.16 and Table 6.13.
The discriminant distributions for the selected hadronic events are depicted in Figure 6.8. From the selected data, signal events, background and ISR-background events as described in section 6.1 the numbers in the following Tables are obtained by applying the additional selection criterion, $D_{threshold} \geq 2.3$.
The number of tagged selected events in data compared to the number of tagged generated events expected, are listed in Table 6.12. The number of tagged background events and tagged ISR-background events are compared to the number of tagged selected events in data and listed in Table 6.11. The composition of the entire tagged sample according to the simulation is listed in Table 6.14. The composition of the tagged selected signal events and the tagged selected ISR-background events in terms of different quark flavours is listed unnormalised in Table 6.15 and Table 6.16.

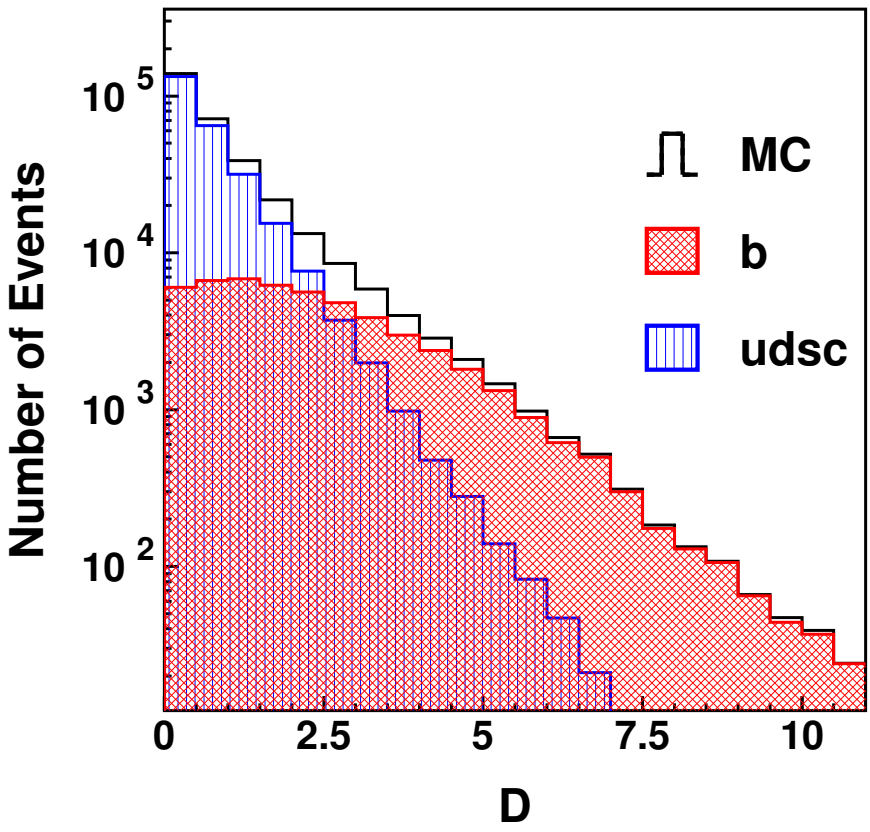

Figure 6.7: The distribution of the discriminant variable obtained for Monte Carlo simulated $q\bar{q}$ events.

$\sqrt{s}$(GeV)	Process	N_{bkg}^{gen}(before)	$N_{bkg}^{gen,t}$(after)	$\varepsilon_{bkg}^{t} \pm \Delta\varepsilon_{bkg}^{t}$
191.6	$e^+e^- \to ZZ$	4998	502	0.101 ± 0.004
	$e^+e^- \to Zee$	9975	47	0.0048 ± 0.0007
	$e^+e^- \to W^+W^-(\gamma)$	249566	6128	0.0246 ± 0.0003
	$e^+e^- \to \tau^+\tau^-$	3724	1	$5.4 \cdot 10^{-4} \pm 4.0 \cdot 10^{-4}$
	$e^+e^- \to We\nu$	99362	454	0.0046 ± 0.0002
	$e^+e^- \to e^+e^-$hadrons	1116500	0	$9.0 \cdot 10^{-7} \pm 9.0 \cdot 10^{-7}$
195.5	$e^+e^- \to ZZ$	50000	5242	0.105 ± 0.001
	$e^+e^- \to Zee$	36000	183	0.0051 ± 0.0004
	$e^+e^- \to W^+W^-(\gamma)$	489160	12372	0.0253 ± 0.0002
	$e^+e^- \to \tau^+\tau^-$	3755	1	$5.3 \cdot 10^{-4} \pm 4.0 \cdot 10^{-4}$
	$e^+e^- \to We\nu$	100000	446	0.0045 ± 0.0002
	$e^+e^- \to e^+e^-$hadrons	1116500	12	$9.0 \cdot 10^{-7} \pm 9.0 \cdot 10^{-7}$
199.5	$e^+e^- \to ZZ$	9946	957	0.096 ± 0.003
	$e^+e^- \to Zee$	19909	106	0.0054 ± 0.0005
	$e^+e^- \to W^+W^-(\gamma)$	466900	11601	0.0248 ± 0.0002
	$e^+e^- \to \tau^+\tau^-$	4968	0	$2.0 \cdot 10^{-4} \pm 2.0 \cdot 10^{-4}$
	$e^+e^- \to We\nu$	100000	393	0.0039 ± 0.0002
	$e^+e^- \to e^+e^-$hadrons	1404200	0	$7.0 \cdot 10^{-7} \pm 7.0 \cdot 10^{-7}$
201.7	$e^+e^- \to ZZ$	5000	512	0.103 ± 0.004
	$e^+e^- \to Zee$	10000	53	0.0054 ± 0.0007
	$e^+e^- \to W^+W^-(\gamma)$	287555	7162	0.0249 ± 0.0003
	$e^+e^- \to \tau^+\tau^-$	5000	0	$2.0 \cdot 10^{-4} \pm 2.0 \cdot 10^{-4}$
	$e^+e^- \to We\nu$	99515	469	0.0047 ± 0.0002
	$e^+e^- \to e^+e^-$hadrons	1404200	7	$7.0 \cdot 10^{-7} \pm 7.0 \cdot 10^{-7}$
205.2	$e^+e^- \to ZZ$	9948	998	0.100 ± 0.003
	$e^+e^- \to Zee$	20000	79	0.0040 ± 0.0005
	$e^+e^- \to W^+W^-(\gamma)$	498391	12309	0.0247 ± 0.0002
	$e^+e^- \to \tau^+\tau^-$	4994	0	$2.0 \cdot 10^{-4} \pm 2.0 \cdot 10^{-4}$
	$e^+e^- \to We\nu$	39053	163	0.0042 ± 0.0003
	$e^+e^- \to e^+e^-$hadrons	6998590	1	$2.9 \cdot 10^{-7} \pm 2.0 \cdot 10^{-7}$
206.7	$e^+e^- \to ZZ$	125791	12400	0.0986 ± 0.0008
	$e^+e^- \to Zee$	99728	420	0.0042 ± 0.0002
	$e^+e^- \to W^+W^-(\gamma)$	660013	16203	0.0246 ± 0.0002
	$e^+e^- \to \tau^+\tau^-$	10000	1	$2.0 \cdot 10^{-4} \pm 1.0 \cdot 10^{-4}$
	$e^+e^- \to We\nu$	118652	568	0.0048 ± 0.0002
	$e^+e^- \to e^+e^-$hadrons	9066498	2	$3.3 \cdot 10^{-7} \pm 1.9 \cdot 10^{-7}$

Table 6.10: N_{bkg}^{gen}(before), is the number of generated background events that are analysed for the listed processes. $N_{bkg}^{gen,t}$(after), is the number of generated background events that remain after the selection is carried out described in section 6.1 and the additional selection criterion, $D_{threshold} \geq 2.3$, is applied. ε_{bkg}^{t}, is the selection efficiency calculated from N_{bkg}^{gen}(before) and $N_{bkg}^{gen,t}$(after) according to equation 6.5.

$\sqrt{s}$(GeV)	N^{gen}_{signal}(before)	$N^{gen,t}_{ISR}$(after)	$\varepsilon^{t}_{ISR} \pm \Delta\varepsilon^{t}_{ISR}$
191.6	99516	235	0.0024 ± 0.0002
195.5	189499	423	0.0022 ± 0.0001
199.5	193750	401	0.0021 ± 0.0001
201.7	98750	221	0.0023 ± 0.0002
205.2	497900	1003	$2.03 \cdot 10^{-3} \pm 6.0 \cdot 10^{-5}$
206.7	1402050	2739	$1.95 \cdot 10^{-3} \pm 4.0 \cdot 10^{-5}$

Table 6.11: N^{gen}_{signal}(before), is the number of generated signal events that are analysed. $N^{gen,t}_{ISR}$(after), is the number of generated ISR-background events that remain after the selection is carried out described in section 6.1 ε^{t}_{ISR}, is the selection efficiency calculated from N^{gen}_{signal}(before) and $N^{gen,t}_{ISR}$(after) according to equation 6.5.

$\sqrt{s}$(GeV)	tagged selected/tagged expected
191.6	100/91.7
195.5	250/239.7
199.5	223/220.5
201.7	124/98.1
205.2	197/191.8
206.7	383/344.1

Table 6.12: Numbers of tagged high energy events selected from the data and the expected numbers of tagged generated events for the different centre–of–mass energies. The number of tagged events expected is normalised to the number of selected events in data according to equation 6.2.

$\sqrt{s}$(GeV)	N^{t}_{sel}	N^{t}_{bkg}	N^{t}_{ISR}
191.6	100	16.8	6.8
195.5	250	49.9	17.1
199.5	223	48.7	15.0
201.7	124	22.1	7.0
205.2	197	46.2	12.7
206.7	383	83.6	23.4

Table 6.13: The numbers of tagged selected events, tagged background events and tagged ISR-background events are listed. The number of tagged background and tagged ISR-background events are normalised to the number of tagged events in data according to equation 6.2.

Process	192 GeV	196 GeV	200 GeV	202 GeV	205 GeV	207 GeV
$e^+e^- \to q\bar{q}(\gamma)$	75.48	191.28	172.85	76.51	147.24	258.59
$e^+e^- \to ZZ$	3.34	10.38	10.07	4.83	10.06	18.21
$e^+e^- \to Zee$	0.48	1.5	1.56	0.69	1.08	2.09
$e^+e^- \to W^+W^-(\gamma)$	12.23	36.06	35.71	15.96	32.97	59.49
$e^+e^- \to \tau^+\tau^-$	0.06	0.17	–	–	–	0.08
$e^+e^- \to We\nu$	0.10	0.29	0.26	0.14	0.26	5.27
$e^+e^- \to e^+e^-$hadrons	–	–	–	–	0.18	0.37

Table 6.14: The composition of the tagged generated event sample according to the simulation normalised to the number of selected events in the data..

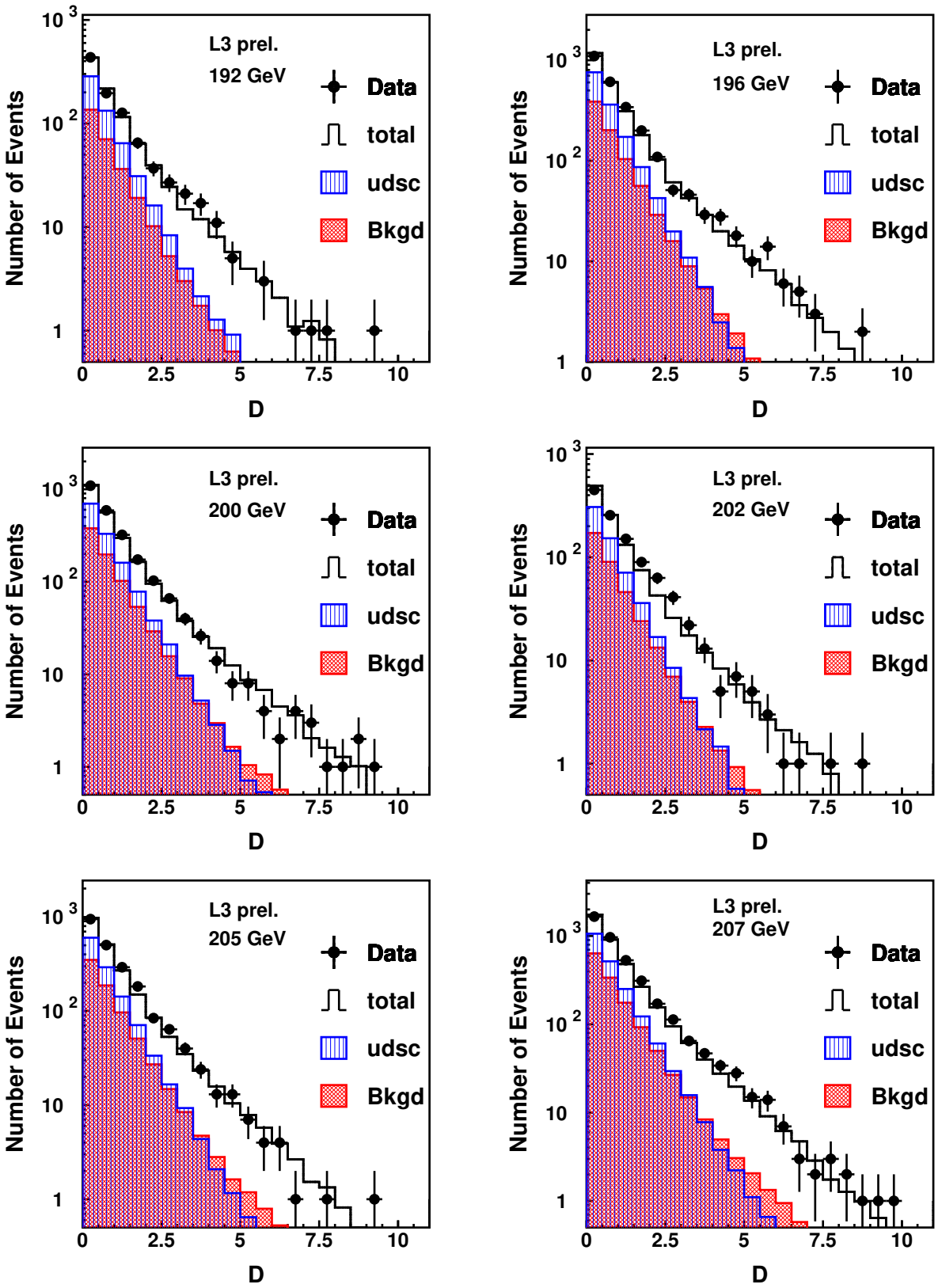

Figure 6.8: Discriminant distributions for the analysed centre–of–mass energies. The black dots are the data, the open histograms represent all generated events and the hatched histograms are the charm and light quark flavours and the background contributions.

$\sqrt{s}$(GeV)	N_b^t	N_c^t	N_{uds}^t
191.6	1875	392	373
195.5	3388	676	707
199.5	3166	726	768
201.7	1706	331	383
205.2	8042	1808	1813
206.7	22224	5009	5182

Table 6.15: The composition of tagged selected signal events is listed. The numbers are not normalised to the number of events in the data.

$\sqrt{s}$(GeV)	$N_{b,ISR}^t$	$N_{c,ISR}^t$	$N_{uds,ISR}^t$
191.6	192	21	22
195.5	326	46	51
199.5	315	44	42
201.7	176	19	26
205.2	748	132	123
206.7	2195	325	359

Table 6.16: The composition of ISR-background events is listed. The numbers are not normalised to the number of events in the data.

Chapter 7

The Measurement of the Total Hadronic Cross Section

The selection of hadronic events, described in section 6.1, and the measurement of the integrated luminosity (see Table 4.1) enables now the measurement of the hadronic cross section, σ_{had}. The measurement is carried out for the analysed centre–of–mass energies listed in section 4.2. The efficiencies in this chapter and the following chapters are computed according to appendix B.

7.1 The Measurement of σ_{had}

The cross section and its statistical uncertainty are calculated by:

$$\sigma \pm \Delta\sigma = \frac{\mathrm{N_{sel}} - \mathrm{N_{bkg}} - \mathrm{N_{ISR}}}{\mathcal{L} \cdot \varepsilon} \pm \frac{\sqrt{\mathrm{N_{sel}}}}{\mathcal{L} \cdot \varepsilon}. \tag{7.1}$$

$\mathrm{N_{sel}}$ is the number of selected data events. $\mathrm{N_{bkg}}$ is the number of generated background events passing the hadronic event selection. $\mathrm{N_{ISR}}$ is the number of ISR-background events described in subsection 5.2.1 and 6.2. The total efficiency, ε, is the product of the selection efficiency, $\varepsilon_{\mathrm{sel}}$, and the trigger efficiency, $\varepsilon_{\mathrm{trig}}$:

$$\varepsilon = \varepsilon_{\mathrm{sel}} \cdot \varepsilon_{\mathrm{trig}}. \tag{7.2}$$

The total efficiency and the values of $\mathrm{N_{sel}}$, $\mathrm{N_{bkg}}$ and $\mathrm{N_{ISR}}$ are listed in Table 7.1.

7.1.1 The Selection Efficiency

The selection efficiency is calculated using generated signal events. It is using the number of events passing the hadronic event selection given in Table 6.1 and the number of events that pass only the criterion on the reconstructed effective centre–of–mass energy ($\sqrt{\mathrm{s'_{reco}}} > 0.85\sqrt{\mathrm{s}}$). The selection efficiency is also corrected for remaining ISR-background

$\sqrt{s}$(GeV)	N_{sel}	N_{bkg}	N_{ISR}	$\varepsilon \pm \Delta\varepsilon$
191.6	949	285.9	64.5	0.9982 ± 0.0003
195.5	2571	818.1	161.6	0.9980 ± 0.0002
199.5	2466	805.1	145.7	0.9979 ± 0.0003
201.7	1108	363.7	64.6	0.9981 ± 0.0003
205.2	2199	750.1	132.0	0.9978 ± 0.0001
206.7	3953	1366.2	239.2	0.9976 ± 0.0001

Table 7.1: The numbers of selected events in data, N_{sel}, generated background events, N_{bkg}, generated ISR-background events, N_{ISR}, and the total efficiency, ε, are listed. The background events and ISR-background events are normalised to the data by the integrated luminosity.

events by subtracting the corresponding events as described above. The selection efficiency is calculated according to appendix B with:

$$n = N^{gen}_{all}(\text{after}) - N^{gen}_{ISR}(\text{after}) \tag{7.3}$$

$$N = N^{gen}_{all}(\text{before}) - N^{gen}_{ISR}(\text{before}) \tag{7.4}$$

$$\varepsilon_{sel} = \frac{n+1}{N+2} \pm \sqrt{\frac{(n+1)(N-n+1)}{(N+3)(N+2)^2}} \tag{7.5}$$

$$\tag{7.6}$$

The notation 'before' and 'after' refers to the selection criteria for the visible energy and the collinearity as explained in section 6.3. The selection efficiency is listed in Table 7.2.

7.1.2 The Trigger Efficiency

The trigger efficiency, ε_{trig}, is obtained from data. The different trigger levels are treated independently and hence the three trigger levels are taken as uncorrelated. The total trigger efficiency is then the product of the trigger efficiencies of the individual trigger levels:

$$\varepsilon_{trig} = \varepsilon^{l1}_{trig} \cdot \varepsilon^{l2}_{trig} \cdot \varepsilon^{l3}_{trig} \tag{7.7}$$

At trigger level-1 all subdetector triggers are read out. Hadronic events have high multiplicity and large energy deposition, hence the TEC and energy trigger should have been activated. The trigger efficiency for trigger level-1, ε^{l1}_{trig}, and its statistical uncertainty are calculated in the following way:

$$\varepsilon^{l1}_{trig} = \varepsilon_{TEC} + \varepsilon_E - \varepsilon_{TEC} \cdot \varepsilon_E \tag{7.8}$$

$\sqrt{s}$(GeV)	$\varepsilon_{\mathrm{sel}} \pm \Delta\varepsilon_{\mathrm{sel}}$
191.6	0.9982 ± 0.0003
195.5	0.9980 ± 0.0002
199.5	0.9983 ± 0.0002
201.7	0.9981 ± 0.0003
205.2	0.9978 ± 0.0001
206.7	0.9980 ± 0.0001

Table 7.2: The selection efficiency with the total error derived from generated signal events.

$$\Delta\varepsilon^{\mathrm{l1}}_{\mathrm{trig}} = \pm\sqrt{(1-\varepsilon_{\mathrm{TEC}})^2 \cdot (\Delta\varepsilon_{\mathrm{E}})^2 + (1-\varepsilon_{\mathrm{E}})^2 \cdot (\Delta\varepsilon_{\mathrm{TEC}})^2}. \tag{7.9}$$

The statistical uncertainty, $\Delta\varepsilon^{\mathrm{l1}}_{\mathrm{trig}}$, is calculated according to the gaussian error propagation law. The single efficiencies for the TEC trigger and the energy trigger is calculated according to appendix B with:

$$\varepsilon_{\mathrm{TEC}} = \frac{\mathrm{N}_{\mathrm{TEC}\oplus\mathrm{E}}+1}{\mathrm{N}_{\mathrm{E}}+2} \pm \sqrt{\frac{(\mathrm{N}_{\mathrm{TEC}\oplus\mathrm{E}}+1)(\mathrm{N}_{\mathrm{E}}-\mathrm{N}_{\mathrm{TEC}\oplus\mathrm{E}}+1)}{(\mathrm{N}_{\mathrm{E}}+3)(\mathrm{N}_{\mathrm{E}}+2)^2}} \tag{7.10}$$

$$\varepsilon_{\mathrm{E}} = \frac{\mathrm{N}_{\mathrm{TEC}\oplus\mathrm{E}}+1}{\mathrm{N}_{\mathrm{TEC}}+2} \pm \sqrt{\frac{(\mathrm{N}_{\mathrm{TEC}\oplus\mathrm{E}}+1)(\mathrm{N}_{\mathrm{TEC}}-\mathrm{N}_{\mathrm{TEC}\oplus\mathrm{E}}+1)}{(\mathrm{N}_{\mathrm{TEC}}+3)(\mathrm{N}_{\mathrm{TEC}}+2)^2}} \tag{7.11}$$

Therefore, the number of hadronic events that have TEC trigger information, $\mathrm{N}_{\mathrm{TEC}}$, the number of hadronic events that have energy trigger information, N_{E}, and the number of events that have TEC trigger and energy trigger information, $\mathrm{N}_{\mathrm{TEC}\oplus\mathrm{E}}$ are counted. The results from trigger level-1 are listed in Table 7.3. The efficiencies resulting from trigger level-2 and level-3 are calculated from events that were accepted, although had a negative decision from the triggers. These events are called prescale events. For trigger level-2 it happens every 20th event and for trigger level-3 every 100th event. None of these events were found in the selected data events listed in Table 6.4, so that $\varepsilon^{\mathrm{l2}}_{\mathrm{trig}}$ and $\varepsilon^{\mathrm{l3}}_{\mathrm{trig}}$ are practically at 100%.

7.2 Systematic Uncertainties

Systematic uncertainties are studied for the event selection, the background and the ISR-background simulation, the selection efficiency, the trigger efficiency and the integrated luminosity.
The event selection is the dominant uncertainty for the measurement of the hadronic cross

$\sqrt{s}$(GeV)	N_E	N_{TEC}	$N_{TEC\oplus E}$	$\varepsilon^{l1}_{trig} \pm \Delta\varepsilon^{l1}_{trig}$
191.6	949	921	921	0.99997 ± 0.00003
195.5	2571	2484	2484	0.99999 ± 0.00001
199.5	2459	2171	2164	0.99956 ± 0.00016
201.7	1107	1091	1090	0.99997 ± 0.00002
205.2	2195	2156	2152	0.99995 ± 0.00002
206.7	3880	3877	3805	0.99963 ± 0.00006

Table 7.3: The number of events with TEC trigger information, energy trigger information and with TEC trigger and energy trigger information. The last column contains the trigger efficiencies for trigger level-1 with statistical uncertainties.

section. The systematic uncertainty of σ_{had} resulting from the event selection, is obtained by varying the selection criteria within reasonable ranges and taking the largest deviation of the cross section as systematic uncertainty. The selection criterion for the visible energy (listed in Table 6.1), $E_{vis}/\sqrt{s}$, is varied between $0.5 \leq E_{vis}/\sqrt{s} \leq 0.7$. The selection criterion for the collinearity is varied between, $2.6 \leq$ collinearity ≤ 2.8. The fluctuation of σ_{had} due to the variation of the selection criteria is depicted in Figure 7.1. The deviation of σ_{had} due to the decreasing number of selected events is small (see Figure 6.2 and Figure 6.3). The largest deviation of σ_{had} due to the variation of the selection criterion for the visible energy is 0.15 while the statistical uncertainty changes from 0.4516 for $E_{vis}/\sqrt{s} \geq 0.5$ to 0.4554 for $E_{vis}/\sqrt{s} \geq 0.7$. Hence the difference in the statistical uncertainty is 0.0038. The same is true for the collinearity where the corresponding numbers are 0.12 compared to 0.0076. The selection criteria for the effective centre–of–mass energy, s', the number of calorimetric clusters, $N_{Cluster}$, and the number of charged tracks, N_{track}, as listed in Table 6.1 is taken as definition of a phase space for hadronic high energy events.

The uncertainty resulting from the background and the ISR-background events is calculated according to the gaussian error propagation law by:

$$\Delta F(x_1, \ldots, x_n) = \pm \sqrt{\sum_{i=1}^{n} \left(\frac{\partial F}{\partial x_i} \right)^2 (\Delta x_i)^2}. \tag{7.12}$$

A parameter $F(x_1, \ldots, x_n)$ is a function of n variables x_i; $(i = 1, \ldots, n)$, then the variation of $F(x_1, \ldots, x_n)$, $\Delta F(x_1, \ldots, x_n)$, is calculated according to equation 7.12 as function of partial derivatives of $F(x_1, \ldots, x_n)$ w.r.t. the n variables x_i; $(i = 1, \ldots, n)$ and the errors of the variables x_i; $(i = 1, \ldots, n)$, Δx_i; $(i = 1, \ldots, n)$.

The efficiencies ε_{bkg} and ε_{ISR}, as listed in Table 6.2 together with their statistical uncertainties, correspond to the variables, x_i; $(i = 1, \ldots, n)$, and their errors, Δx_i; $(i = 1, \ldots, n)$. The cross section formula given in equation 7.1 corresponds to the function $F(x_1, \ldots, x_n)$.

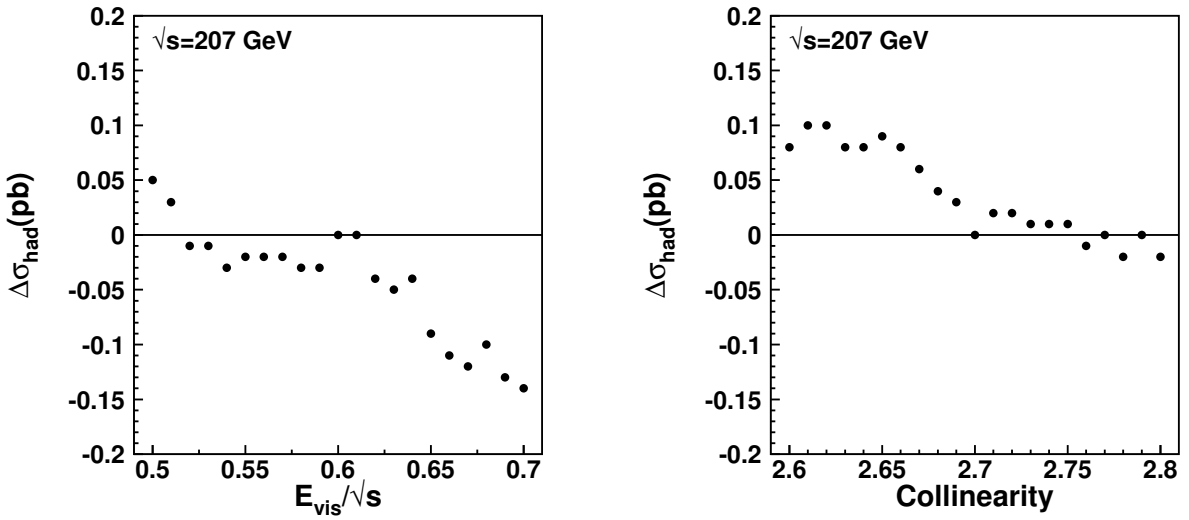

Figure 7.1: The pictures show the deviation of σ_{had} due to the variation of the selection criteria as explained in the text.

The calculation of the systematic uncertainty of σ_{had} resulting from background events, is carried out for each background contribution separately and then added in quadrature as given in equation 7.12. The systematic uncertainty of σ_{had} resulting from the selection efficiency, $\varepsilon_{\mathrm{sel}}$ as listed in Table 7.2 and from the trigger efficiency, $\varepsilon_{\mathrm{trig}}$ as listed in Table 7.3 is calculated the same way. The systematic effect coming from the integrated luminosity, $\mathcal{L}$ as listed in Table 4.1, is also calculated according to equation 7.12 using the statistic uncertainties of the integrated luminosity.
The studied error sources and their corresponding influence on σ_{had} are listed in Table 7.4. The individual uncertainties are added in quadrature and form the total systematic uncertainty of σ_{had} as listed in the last row of Table 7.4.

7.3 Final Results

The results of the measurement of σ_{had} are corrected for full angular acceptance, final state radiation and initial-final state radiation interference following the LEP Electroweak Working Group standards. Since only events with $|\cos\theta \leq 0.98|$ are detectable and hence recorded, the Standard Model prediction of σ_{had} is computed for full angular acceptance without final state radiation and initial-final state radiation interference ($|\cos\theta \leq 1|$, FINR=0 and INTF=0) and limited angular acceptance taking into account final state radiation and initial-final state radiation interference ($|\cos\theta \leq 0.98|$, FINR=1, INTF=1). FINR and INTF denote the ZFITTER [43] steering flags for final state radia-

Source	Δ_{sys}(pb)					
	191.6 GeV	195.5 GeV	199.5 GeV	201.7 GeV	205.2 GeV	206.7 GeV
Event selection	0.400	0.200	0.210	0.300	0.250	0.220
finite MC stat.	0.006	0.004	0.004	0.006	0.003	0.001
Background	0.117	0.106	0.093	0.103	0.101	0.089
ISR-correction	0.064	0.042	0.039	0.055	0.041	0.039
Trigger	0.0006	0.0002	0.0030	0.0004	0.0004	0.0003
Luminosity	0.056	0.019	0.018	0.041	0.019	0.010
Total	0.43	0.23	0.23	0.32	0.27	0.24

Table 7.4: Systematic uncertainty contributions from the investigated sources. The uncertainties of each individual source are added in quadrature and form the total systematic uncertainty of σ_{had}.

tion and initial-final state radiation interference.
The ratio $\sigma_{\text{had}}^{\text{SM}}(|\cos\theta \leq 1|, \text{FINR} = 0, \text{INTF} = 0)/\sigma_{\text{had}}^{\text{SM}}(|\cos\theta \leq 0.98|, \text{FINR} = 1, \text{INTF} = 1)$ is taken as correction factor and multiplied to the measured values of σ_{had}. The results are listed in Table 7.5 and compared to the Standard Model prediction of the hadronic cross section. The theory error on the Standard Model prediction of the hadronic cross section is calculated with ZFITTER V6.35 by varying the free parameters, discussed in section 2.7 by their quoted uncertainties. Only one parameter is varied at the time and the largest deviation of the hence calculated hadronic cross section from the hadronic cross section obtained by taking the central values of the six parameters is taken as error. The errors resulting from the individual variations are added in quadrature and form the theory error of the Standard Model prediction of the hadronic cross section as listed in Table 7.5. In addition the combined LEP measurements of the hadronic cross section, $\sigma_{\text{had}}^{\text{LEP}}$, are listed. The results of the analysis presented here are in good agreement with the combined results of LEP. The results of the measurement of $\sigma_{\text{had}}^{\text{measured}}$ are in good agreement with the Standard Model prediction, $\sigma_{\text{had}}^{\text{SM}}$, as depicted in Figure 7.2.

$\sqrt{s}$(GeV)	$\sigma_{had}^{measured} \pm \Delta_{stat} \pm \Delta_{sys}$(pb)	$\sigma_{had}^{LEP} \pm \Delta_{tot}$(pb)	$\sigma_{had}^{SM} \pm \Delta_{theo}$(pb)
191.6	$21.22 \pm 1.04 \pm 0.43$	22.291 ± 0.523	21.213 ± 0.070
195.5	$20.03 \pm 0.61 \pm 0.23$	20.729 ± 0.338	20.104 ± 0.064
199.5	$19.15 \pm 0.60 \pm 0.23$	19.372 ± 0.319	19.064 ± 0.061
201.7	$19.35 \pm 0.90 \pm 0.32$	19.278 ± 0.430	18.529 ± 0.059
205.2	$18.19 \pm 0.62 \pm 0.27$	18.119 ± 0.316	17.727 ± 0.056
206.7	$17.86 \pm 0.45 \pm 0.24$	17.423 ± 0.263	17.401 ± 0.055

Table 7.5: The results of the measurement of the hadronic cross section compared to the combined LEP measurements, σ_{had}^{LEP}, and the Standard Model prediction, σ_{had}^{SM}. The quoted uncertainties on the combined LEP measurements contain the statistical and the systematic uncertainties added in quadrature. The Standard Model prediction is calculated with ZFITTER V6.35 [43] taking into account QCD and QED corrections and weak corrections. The ZFITTER flags for the final state radiation and initial-final state radiation interference, FINR=0 and INTF=0, are set to zero according to the LEP Electroweak Working Group (LEPEWWG) for the treatment of hadronic final states [47].

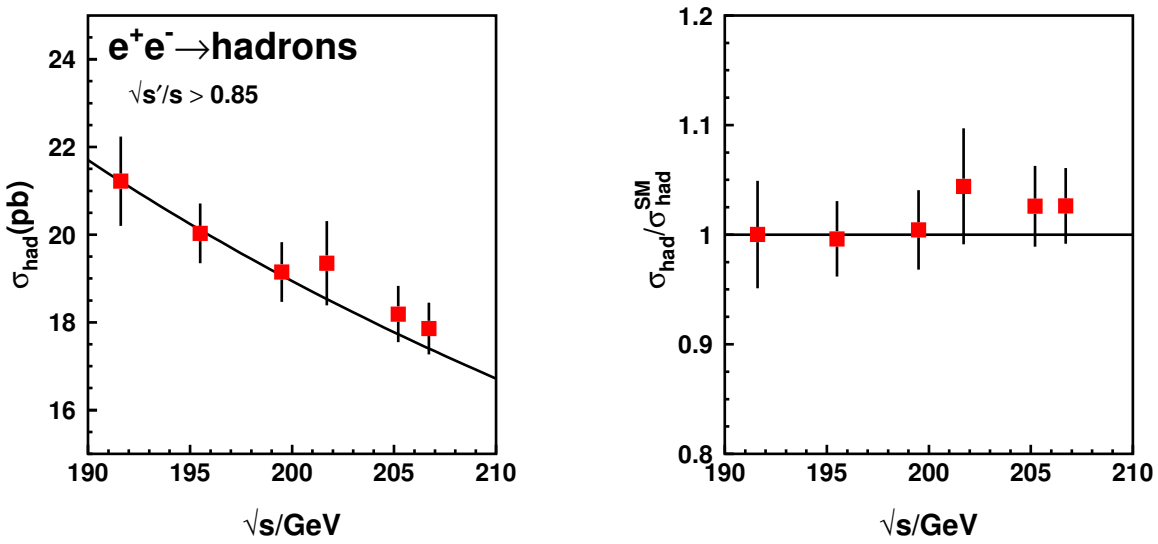

Figure 7.2: The pictures show the measurements of $\sigma_{had}^{measured}$ as listed in Table 7.5 (squares) compared to the Standard Model prediction, σ_{had}^{SM} (curve).

Chapter 8

The Measurement of R_b

The measurement of R_b requires the separation of hadronic events that contain B hadrons from other hadronic final states. The event selection for hadronic events is described in section 6.1. The final state separation of B hadrons is carried out with the B-tag as described in section 6.4. The measurement of R_b is then performed according to the single-tag-method.

8.1 The Measurement of R_b

Due to low statistics the single-tag-method is applied where the whole event is tagged to be a $b\bar{b}$ event [72]. Another method is the double-tag-method, where the event is subdivided into two hemispheres, defined by the primary vertex and the directions of the jets. The hemispheres are then tagged separately for B hadrons. The measurement of R_b, using the double-tag-method, would need higher statistics of hadronic events than given in this analysis, in order to gain anything from the smaller systematic uncertainty possible with this method. The detailed information of the measurement of R_b according to the double-tag-method can be found in [47].
In this analysis, the measurement of R_b is performed according to the single-tag-method. Therefore, a threshold value for the discriminant, $D_{threshold}$, is ascertained. The threshold value is ascertained as result of the optimisation of the total uncertainty of R_b and determined to $D_{threshold} = 2.3$. This is depicted in Figure 8.1. The ratio of the number of selected hadronic events and the number of selected and tagged hadronic events is then equal to:

$$\frac{N^t_{sel} - N^t_{bkg} - N^t_{ISR}}{N_{sel} - N_{bkg} - N_{ISR}} = \varepsilon_b R_b + \varepsilon_c R_c + \varepsilon_{uds} R_{uds}. \tag{8.1}$$

N^t_{sel}, N^t_{bkg} and N^t_{ISR} is the number of tagged data events, tagged background events and tagged ISR-background events as given in section 6.5 and listed in Table 6.13. N_{sel}, N_{bkg} and N_{ISR} are the corresponding events listed in Table 7.1 in section 6.3. The corresponding numbers are listed here again in Table 8.1 and Table 8.2. R_c and R_{uds} correspond to

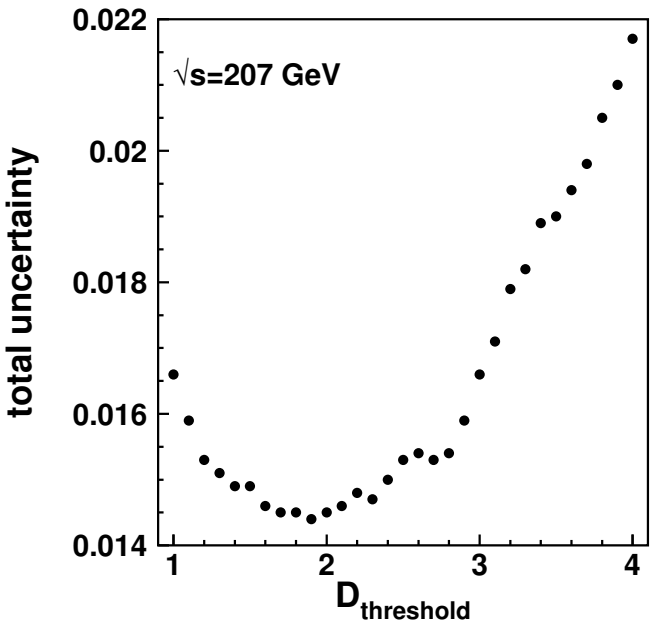

Figure 8.1: The total uncertainty of R_b as a function of $D_{threshold}$, here shown as an example for $\sqrt{s} = 206.7$ GeV. The total uncertainty becomes minimal in the range of $D_{threshold} = 1.7 - 2.3$, for the different centre–of–mass energies listed in Table 4.1. The threshold value is chosen to be $D_{threshold} = 2.3$ for the analysed centre–of–mass energies, because the value of the total uncertainty is almost constant in the range of $D_{threshold} = 1.7 - 2.3$.

$\sqrt{s}$(GeV)	N^t_{sel}	N^t_{bkg}	N^t_{ISR}
191.6	100	16.8	6.8
195.5	250	49.9	17.1
199.5	223	48.7	15.0
201.7	124	22.1	7.0
205.2	197	46.2	12.7
206.7	383	83.6	23.4

Table 8.1: The numbers of tagged data events, tagged background events and tagged ISR-background events.

$\sqrt{s}$(GeV)	N_{sel}	N_{bkg}	N_{ISR}
191.6	949	285.9	64.5
195.5	2571	818.1	161.6
199.5	2466	805.1	145.7
201.7	1108	363.7	64.6
205.2	2199	750.1	132.0
206.7	3953	1366.2	239.2

Table 8.2: The numbers of selected events, background events, ISR-background events are listed. The number of background and ISR-background events are normalised to the number of selected events in data according to equation 6.2.

R_b but for charm and light quark flavours. R_{uds} can be replaced by R_b and R_c using the following relation:

$$R_b + R_c + R_{uds} = 1, \tag{8.2}$$

displaying the fact that the centre–of–mass energies delivered by LEP are to small to pair-produce top quarks. The values for R_c are taken as input from the Standard Model calculated by ZFITTER V6.35. The above equation is resolved with respect to R_b:

$$R_b = \frac{1}{\varepsilon_b - \varepsilon_{uds}} \left[\frac{N^t_{sel} - N^t_{bkg} - N^t_{ISR}}{N_{sel} - N_{bkg} - N_{ISR}} - \varepsilon_c R_c - \varepsilon_{uds}(1 - R_c) \right]. \tag{8.3}$$

8.1.1 The Tagging Efficiencies

The tagging efficiencies denoted as ε_b, ε_c and ε_{uds} are calculated according to appendix B taking into account the number of tagged signal events and the total number of selected signal events of the corresponding quark flavour. The numbers are corrected for ISR-background as described in section 7.1

$$n = N^t_q - N^t_{q,ISR} \tag{8.4}$$

$$N = N_q - N_{q,ISR} \tag{8.5}$$

$$\varepsilon_q = \frac{n+1}{N+2} \pm \sqrt{\frac{(n+1)(N-n+1)}{(N+3)(N+2)^2}}. \tag{8.6}$$

The numbers of tagged signal events, N^t_q, and tagged ISR-background, N^t_{ISR}, are listed in Table 6.15 and Table 6.16 in section 6.5. The total number of signal events, N^{all}_q, and the total number of ISR-background events are listed in Table 6.7 and Table 6.8 in section 6.3. The so obtained tagging efficiencies for the different quark flavours are listed in Table 8.3.

$\sqrt{s}$(GeV)	$\varepsilon_b \pm \Delta\varepsilon_b$	$\varepsilon_c \pm \Delta\varepsilon_c$	$\varepsilon_{uds} \pm \Delta\varepsilon_{uds}$
191.6	0.474 ± 0.008	0.0700 ± 0.004	0.0310 ± 0.0020
195.5	0.468 ± 0.006	0.0630 ± 0.002	0.0280 ± 0.0010
199.5	0.437 ± 0.006	0.0673 ± 0.002	0.0310 ± 0.0010
201.7	0.455 ± 0.008	0.0590 ± 0.002	0.0297 ± 0.0010
205.2	0.437 ± 0.004	0.0650 ± 0.002	0.0290 ± 0.0007
206.7	0.435 ± 0.002	0.0645 ± 0.001	0.0290 ± 0.0004

Table 8.3: The tagging efficiencies for bottom, charm and the combined light quark events and their statistical uncertainties are listed.

8.2 Statistical and Systematic Uncertainties

Statistical Uncertainty:
The statistical uncertainty is the dominant source of uncertainties of R_b. Since the number of tagged events is a sub-sample of the number of selected hadronic events, the calculation of the statistical uncertainty is performed according to appendix B:

$$n = N^t_{sel} \tag{8.7}$$

$$N = N_{sel} \tag{8.8}$$

$$\varepsilon = \frac{n+1}{N+2} \pm \sqrt{\frac{(n+1)(N-n+1)}{(N+3)(N+2)^2}}, \tag{8.9}$$

using N^t_{sel} and N_{sel} as listed in Table 8.1 and Table 8.2. N^t_{sel} is then expressed as a function of ε and N_{sel}. The uncertainty of ε is then propagated to R_b according to the gaussian error propagation law (equation 7.12) discussed in section 7.2 and forms the statistical uncertainty of R_b.

Systematic Uncertainties:
The event selection of signal events and tagged signal events, respectively, cause a systematic effect on the measurement of R_b. The tagging efficiencies derived from the generated signal events have statistical uncertainties due to the finite number of generated events. Moreover, the generated signal events are based on underlying distributions that are used for the modelling of quark fragmentation. The input parameters from the underlying distributions have uncertainties that are propagated to R_b. Therefore, the following sources of systematic uncertainties are studied:

- event selection
- finite Monte Carlo statistics
- background and ISR-background correction

- modelling uncertainties
- tracking effects

Event Selection:

The systematic uncertainty, resulting from the event selection, is studied as described in section 7.2. The selection criteria for the visible energy and the collinearity are varied between, $0.5 \leq E_{vis}/\sqrt{s} \leq 0.7$ and $2.6 \leq$ collinearity ≤ 2.8. The selection criteria for the effective centre–of–mass energy, s', the number of calorimetric clusters, $N_{Cluster}$, and the number of charged tracks, N_{track}, as listed in Table 6.1 is taken as definition of a phase space for hadronic high energy events.
The Figures 8.2 and 8.3 depict the uncertainties of R_b resulting from the variation of the selection criteria for the visible energy, $E_{vis}\sqrt{s}$, and the collinearity. The systematic

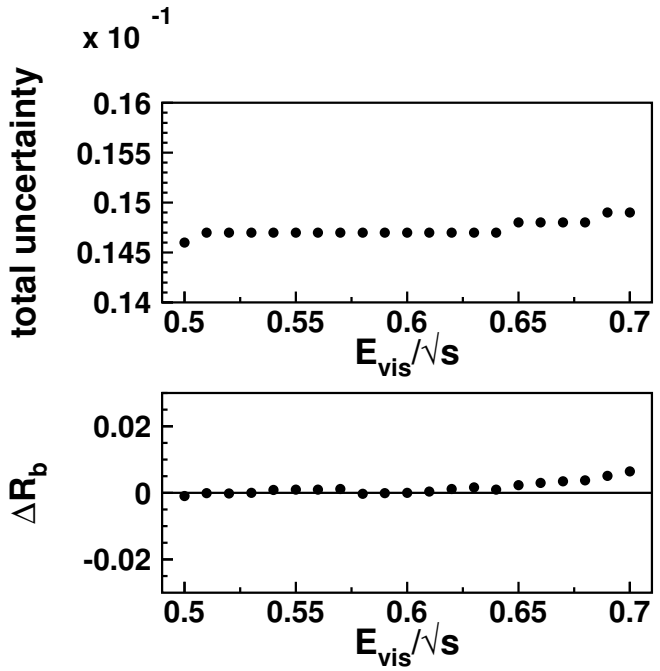

Figure 8.2: The upper picture shows the total uncertainty of R_b as a function of the selection criterion for the visible energy, $E_{vis}/\sqrt{s}$. The resulting uncertainty is almost constant because of the range of the variation (see Figure 6.2). The lower picture shows the fluctuation of R_b, as a function of the selection criterion for the visible energy, $E_{vis}/\sqrt{s}$, with respect to the measured value of R_b. This is an example picture for $\sqrt{s} = 206.7$ GeV. The resulting systematic uncertainty is listed in Table 8.6 for the individual centre–of–mass energies.

uncertainty resulting from the event selection is estimated from the average fluctuation of R_b as a function of the selection criterion. The obtained values are listed in Table 8.6.

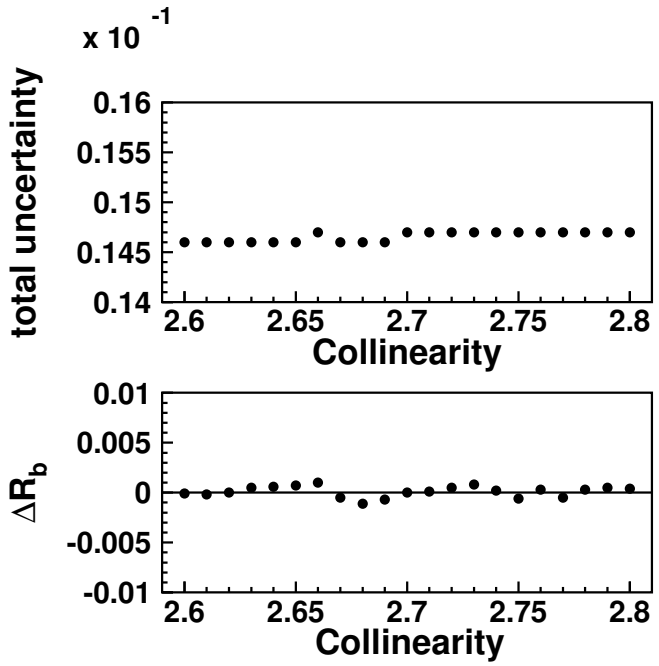

Figure 8.3: The upper picture shows the total uncertainty of R_b as a function of the selection criterion for the collinearity. The lower picture shows the fluctuation of R_b, as a function of the selection criterion for the collinearity, with respect to the measured value of R_b. This is an example picture for $\sqrt{s} = 206.7$ GeV. The resulting systematic uncertainty is listed in Table 8.6 for the individual centre–of–mass energies.

Finite Statistics:
The systematic uncertainty of R_b resulting from finite number of generated events is calculated according to the gaussian error propagation law, given in equation 7.12, using the individual tagging efficiencies and their corresponding statistical uncertainties as listed in Table 8.3. The resulting uncertainties of R_b are added in quadrature and taken as systematic uncertainty of R_b from finite statistics as listed in Table 8.6.

Background and ISR-background Correction:
The systematic uncertainty of R_b due to background and ISR-background correction is also obtained due to the gaussian error propagation law, given in equation 7.12, using the individual statistical uncertainties of the selection efficiencies of the background sources and the ISR-background listed in Table 6.10 and Table 6.11. The uncertainties of R_b resulting from the statistical uncertainties of the selection efficiencies of background and ISR-background are added in quadrature for background and ISR-background separately and listed in Table 8.6.

Quark Modelling:
The systematic uncertainties from quark modelling are obtained from generated signal

events. The quark modelling parameters such as lifetime, branching fractions etc. as listed in Table 8.4, are varied within the corresponding uncertainties and the influence on the discriminant distribution is studied. Modelling uncertainties in ε_c arise from the

Source	Value
b fragmentation parameter:	
$\langle x_E(b) \rangle$	0.702 ± 0.008 [21]
B decay parameters:	
B lifetimes	1.576 ± 0.016 ps [22]
B decay multiplicity	4.955 ± 0.062 [21]
Fractions in $c\bar{c}$-events:	
D^+	0.233 ± 0.027 [22]
D_s	0.103 ± 0.029 [22]
Λ_c	0.063 ± 0.028 [22]
Gluon splitting in $c\bar{c}$-events:	
$g \to c\bar{c}$	$(2.38 \pm 0.48)\%$ [21]
$g \to b\bar{b}$	$(0.13 \pm 0.04) \times g \to c\bar{c}$ [21]
Charm decay parameters:	
D^0 lifetime	0.415 ± 0.004 ps [22]
D^+ lifetime	1.057 ± 0.015 ps [22]
D_s lifetime	0.467 ± 0.017 ps [22]
Λ_c lifetime	0.206 ± 0.012 ps [22]
Charm decay multiplicity:	
D decay multiplicity	2.53 ± 0.06
$BR(D_s \to K^0_S)$	0.46 ± 0.06 [22]
Charm fragmentation parameter:	
$\langle x_E(c) \rangle$	0.484 ± 0.008 [21]
Fractions in uds-events:	
$K^0 \text{and} \Lambda$	JETSET $\pm$ 10%
Gluon splitting in uds-events:	
$g \to c\bar{c}$	$(2.38 \pm 0.48)\%$ [21]
$g \to b\bar{b}$	$(0.13 \pm 0.04) \times g \to c\bar{c}$ [21]

Table 8.4: The modelling parameters to simulate signal events.

residual contamination by charmed hadrons, D^+, D_s, $D^0$and Λ_c. Modelling uncertainties in ε_{uds} arise from the contamination by light hadrons with long lifetime, K^0 and Λ. The lifetimes of K^0 and Λ are varied by $\pm 10\%$ in the Lund Monte Carlo used in the JETSET generator [64] to generate these events. A set of discriminant distributions is generated with JETSET [64], where every distribution corresponds to a varied quark modelling parameter. Since the uncertainties of the quark modelling parameters are independent of the centre–of–mass energy, this set of discriminant distributions is generated for $\sqrt{s} = m_Z$ at LEP I [73]. The varied discriminant distributions cause a modification of the tagging

efficiencies of the different quark flavours, ε_b, ε_c and ε_{uds} and hence a modification of R_b. The resulting uncertainties of the tagging efficiencies are propagated to R_b according to the gaussian error propagation law as explained in equation 7.12. The variations of R_b due to the variations of the tagging efficiencies are listed in Table 8.5. The sign denotes the correlation (positive sign) or anti-correlation (negative sign) between the corresponding parameter and R_b. The individual contributions are summed in quadrature and considered as systematic uncertainty of R_b as listed in Table 8.6.

Tracking Effects:

The uncertainty of R_b due to the tagging procedure is called tracking effects. It is obtained by re-tuning the B-tag. The tuning of the B-tag is based on the precise determination of the impact parameter of a particle track (see section 6.4). Hence, the precise position and size of the beam spot [70] and multiple scattering effects on the track reconstruction are computed. The input parameters for the B-tag are the distances of closest approach (impact parameters) of the tracks (see section 6.4) and parameters to account for multiple scattering of a particle in the material. They are separately varied by the computed uncertainties and the B-tag is re-tuned. This provides modified discriminant distributions. The modified distributions are used to measure R_b. The deviations of these measurements to the measured R_b according to the nominal discriminant distribution are considered as systematic uncertainty and listed in Table 8.6.

Additional Systematics from the B-tag:

At 201.7 GeV centre–of–mass energy a technical problem occured, affecting higher values of the discriminant for the data. A consistency check of the influence of the average size of the beam spot was carried out [70]. The average size amounts to an order of 30-200 μm, compared to the average impact parameter of tracks from N hadrons of 0.5 mm. A wrong determined size of the beam spot would amount to the order of $\mathcal{O}(\%)$ and is hence not responsible for this effect.

Therefore, an independent sample of W^+W^- events is selected and the discriminant distribution is studied. The selection of high energy W^+W^- events is carried out applying the selection criteria listed in Table 6.1 and applying one more criterion $-\log(y_{34}) \leq 5.0$, where the parameter y_{34} describes the transition of a three-jet event to a four-jet event (see appendix A). The corresponding distribution is shown in Figure 8.4.

Since W^+W^- events do not have a significant decay lengths, these events do not have high discriminant values. The discriminant distribution shows a systematic discrepancy between the W^+W^- events selected from data and the simulated W^+W^- events. A procedure is applied to correct for the discrepancy, where random numbers N are generated. These numbers are added eventwise with a certain correction factor C to the discriminant D of the simulated W^+W^- events:

$$\bar{D} = D \cdot (1 + C \cdot |N|). \tag{8.10}$$

Hence the binwise χ^2 of the matching between the data and the generated W^+W^- events is calculated in the following way:

$$\chi^2 = \frac{1}{N_{bin}} \sum_{i=1}^{N_{bin}} \frac{(N^i_{data} - N^i_{W^+W^-}(\bar{D}))^2}{N^i_{data}}, \tag{8.11}$$

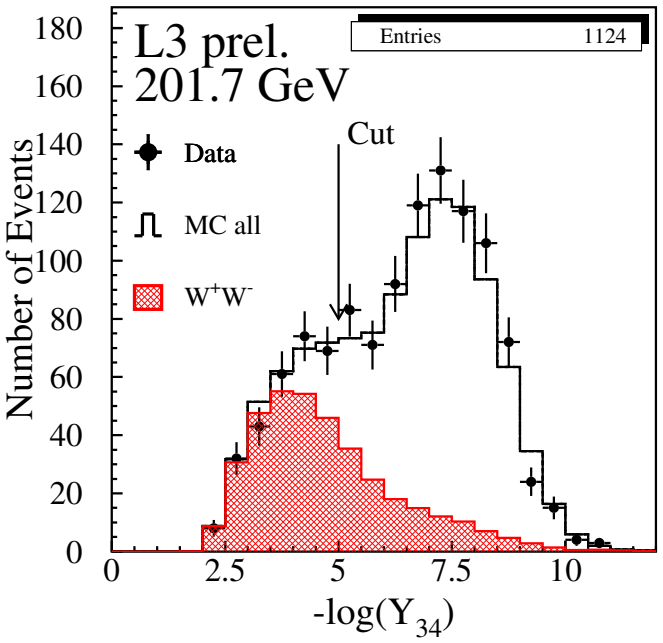

Figure 8.4: The distribution of $-\log(y_{34})$. The dots represent the data, the open histogram represents the generated signal events and the hatched histogram represents the generated W^+W^- events.

where N_{bin} is the number of bins of the discriminant distribution, N^i_{data} is the number of events in the data in the i-th bin and $N^i_{W^+W^-}(\bar{D})$ is the number of generated W^+W^- events in the i-th bin as function of the modified discriminant distribution.
The matching between the data and the generated W^+W^- events as function of the correction factor, C, is shown in Figure 8.5. At $C = 0.07$ the curve has its minimum and the best matching between the selected W^+W^- and simulated W^+W^- events is achieved. The correction factor is applied to the discriminant distribution of the generated $q\bar{q}$ sample. The difference of the measurement of R_b with and without applying the correction factor is taken as additional systematic uncertainty.
The attentive reader might have noticed the high separation power of the selection criterion on $-\log(y_{34})$ in order to reduce the W^+W^- background in the selected data sample, described in section 6.1. An additional cut on $-\log(y_{34})$ enlarges the statistical uncertainty both of σ_{had} and R_b while the systematic uncertainty due to background subtraction is already much smaller than the statistical uncertainty (see section 7.2 in Table 7.4 and section 7.3 in Table 7.5 and this section in Table 8.6 and section 8.4 in Table 8.8).
The systematic uncertainties of R_b and the corresponding sources are listed in Table 8.6.

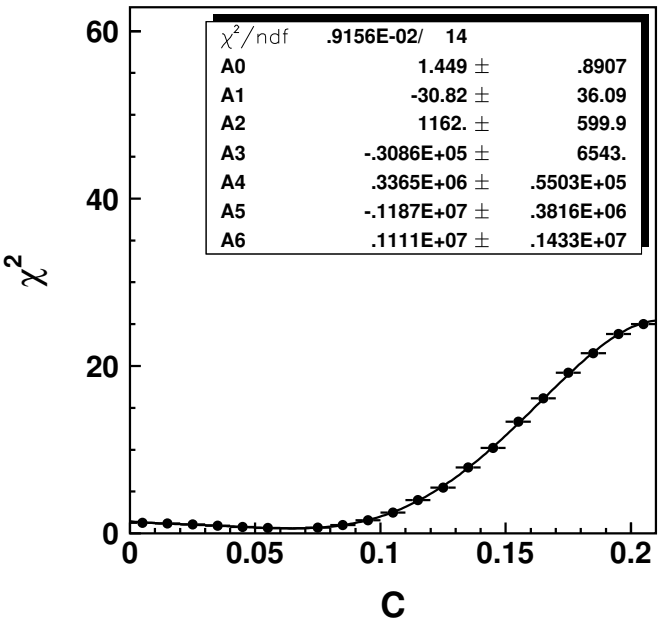

Figure 8.5: The matching between data and simulated events for the selected W^+W^- sample as a function of the correction factor. Zero denotes a perfect matching.

8.3 Correlation between R_b and R_c

R_b is anti-correlated to R_c and the dependence can be parametrised as:

$$R_b = R_b^{meas.} + a(R_c)\frac{(R_c - R_c^{SM})}{R_c}. \quad (8.12)$$

The values for $a(R_c)$ are obtained from generated events and listed in Table 8.7 together with the values of R_c^{SM}.

8.4 Final Results

The measurements of R_b are listed in Table 8.8 with the statistical and systematic uncertainties and are compared to the Standard Model prediction. In addition the combined LEP measurements of R_b are listed. The results of the analysis presented here are in good agreement with the combined results of LEP. The measured results are depicted in Figure 8.6 together with results from a previous analysis.

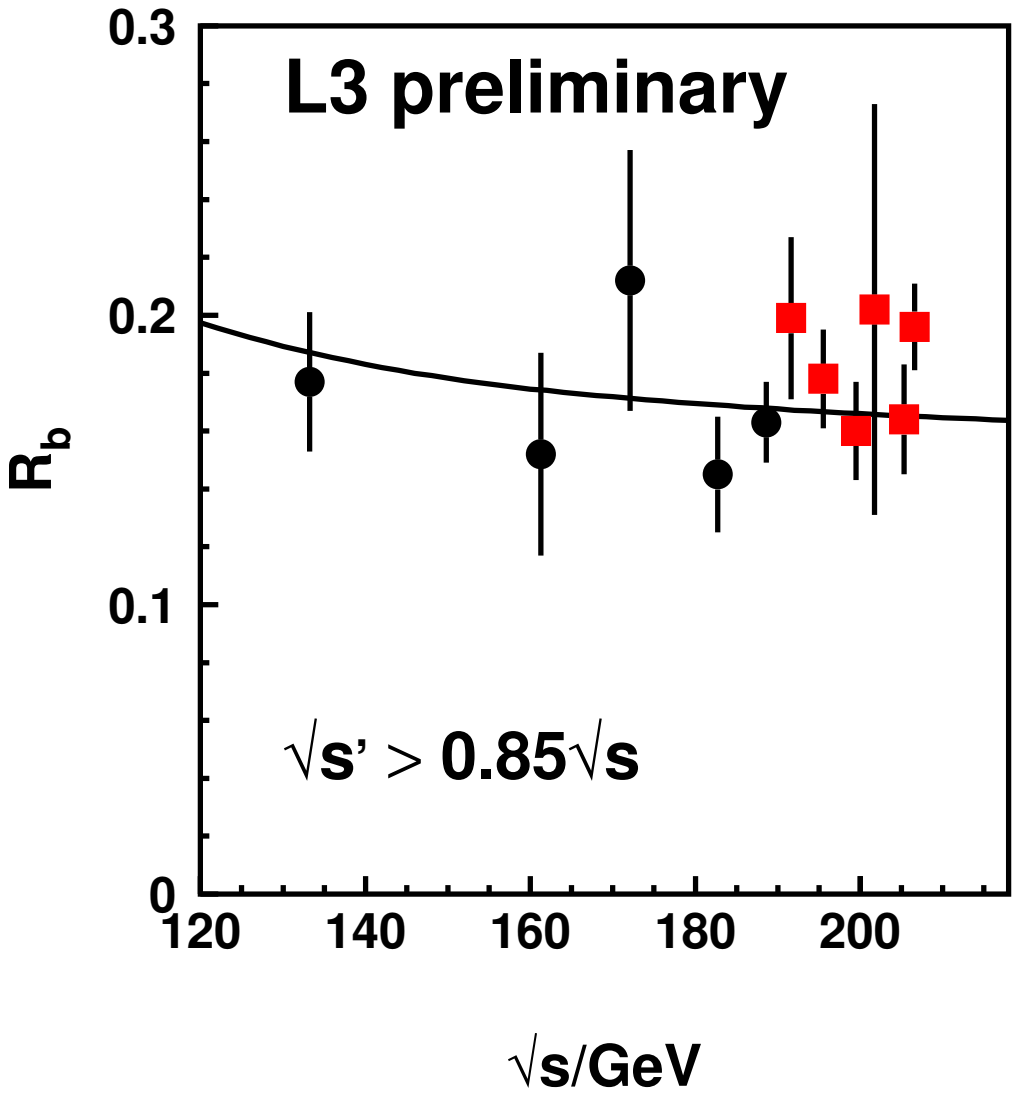

Figure 8.6: The measurement of R_b compared to the Standard Model prediction. The black dots represent the published results from 130 GeV to 189 GeV [72]. The squares represent the results of this analysis.

Source	ΔR_b					
	192 GeV	196 GeV	200 GeV	202 GeV	205 GeV	207 GeV
B fragmentation parameter:						
$\langle x_E(b) \rangle$	0.0023	0.0021	0.0018	0.0026	0.0020	0.0025
B decay parameters:						
B lifetimes	0.0006	0.0005	0.0004	0.0007	0.0005	0.0006
B decay multiplicity	0.0017	0.0015	0.0013	0.0019	0.0015	0.0018
Fractions in $c\bar{c}$-events:						
D^+	-0.0005	-0.0005	-0.0005	-0.0007	-0.0005	-0.0005
D_s	< 0.0001	< 0.0001	< 0.0001	-0.0001	< 0.0001	< 0.0001
Λ_c	0.0002	0.0002	0.0002	0.0003	0.0002	0.0002
Gluon splitting in $c\bar{c}$-events:						
$g \to c\bar{c}$	< 0.0001	< 0.0001	< 0.0001	< 0.0001	< 0.0001	< 0.0001
$g \to b\bar{b}$	< 0.0001	< 0.0001	< 0.0001	< 0.0001	< 0.0001	< 0.0001
c decay parameters:						
D^0 lifetime	-0.0001	-0.0001	-0.0001	-0.0001	-0.0001	-0.0001
D^+ lifetime	-0.0001	-0.0001	-0.0001	-0.0001	-0.0001	-0.0001
D_s lifetime	< 0.0001	< 0.0001	< 0.0001	-0.0001	< 0.0001	< 0.0001
Λ_c lifetime	< 0.0001	< 0.0001	< 0.0001	< 0.0001	< 0.0001	< 0.0001
c lifetime:	0.0001	0.0001	0.0001	0.0002	0.0001	0.0001
c decay multiplicity:						
$D^+ \to 1$ prong	< 0.0001	< 0.0001	< 0.0001	< 0.0001	< 0.0001	< 0.0001
$D^+ \to 5$ prong	< 0.0001	< 0.0001	< 0.0001	< 0.0001	< 0.0001	< 0.0001
$D^0 \to 0$ prong	< 0.0001	< 0.0001	< 0.0001	< 0.0001	< 0.0001	< 0.0001
$D^0 \to 4$ prong	0.0001	0.0001	0.0001	0.0001	0.0001	0.0001
$D^0 \to 6$ prong	< 0.0001	< 0.0001	< 0.0001	< 0.0001	< 0.0001	< 0.0001
$D_s \to 1$ prong	< 0.0001	< 0.0001	< 0.0001	0.0001	0.0001	0.0001
$D_s \to 5$ prong	-0.0001	-0.0001	-0.0001	-0.0001	-0.0001	-0.0001
$D_s \to K_S^0$	-0.0001	-0.0001	-0.0001	-0.0001	-0.0001	-0.0001
c fragmentation parameter:						
$\langle x_E(c) \rangle$	-0.0003	-0.0003	-0.0004	-0.0005	-0.0003	-0.0003
Fractions in uds-events:						
K^0andΛ	-0.0003	-0.0004	-0.0004	-0.0003	-0.0005	-0.0005
Gluon splitting in uds-events:						
$g \to c\bar{c}$	< 0.0001	< 0.0001	< 0.0001	< 0.0001	< 0.0001	< 0.0001
$g \to b\bar{b}$	< 0.0001	< 0.0001	< 0.0001	< 0.0001	< 0.0001	< 0.0001
total	0.0030	0.0027	0.0024	0.0035	0.0027	0.0033

Table 8.5: The systematic uncertainties resulting from the quark modelling. The numbers are the corresponding deviations from the measured value and the positive(negative) sign indicates the correlation(anti-correlation) between the parameter and R_b.

Source	Δ_{sys}					
	192 GeV	196 GeV	200 GeV	202 GeV	205 GeV	207 GeV
Event selection						
$\frac{E_{vis}}{\sqrt{s}}$	0.003	0.003	0.003	0.003	0.003	0.003
collinearity	0.001	< 0.001	0.001	0.001	0.001	0.001
Event selection total	0.003	0.003	0.003	0.003	0.003	0.003
quark-modelling	0.003	0.003	0.002	0.004	0.003	0.003
finite MC stat.	0.005	0.003	0.003	0.005	0.002	0.001
Background	0.003	0.002	0.002	0.003	0.003	0.003
ISR-correction	0.003	0.002	0.002	0.003	0.002	0.002
Tracking effects.	0.003	0.003	0.003	0.003	0.003	0.003
additional systematic	–	–	–	0.066	–	–
Total	0.007	0.005	0.005	0.066	0.005	0.005

Table 8.6: The systematic uncertainties of the investigated sources.

$\sqrt{s}$(GeV)	a(R_c)	$R_c^{SM} \pm \Delta_{theo}$
191.6	-0.023	0.2530 ± 0.0002
195.5	-0.016	0.2541 ± 0.0002
199.5	-0.023	0.2551 ± 0.0003
201.7	-0.018	0.2556 ± 0.0003
205.2	-0.023	0.2564 ± 0.0003
206.7	-0.022	0.2567 ± 0.0003

Table 8.7: The coefficients a(R_c) and the corresponding values for R_c^{SM} calculated by ZFITTER V6.35 taking into account QED corrections, QCD corrections and weak corrections. The ZFITTER flags for the final state radiation and initial-final state radiation interference are set to FINR=0 and INTF=1. The therotical uncertainty on R_c^{SM} is obtained by varying the input parameters by their quoted uncertainties as listed in section 2.7.

$\sqrt{s}$(GeV)	$R_b^{meas.} \pm \Delta_{stat} \pm \Delta_{sys}$	$R_b{}^{LEP} \pm \Delta_{tot}$	$R_b^{SM} \pm \Delta_{theo}$
191.6	$0.199 \pm 0.027 \pm 0.007$	0.1541 ± 0.0149	0.1654 ± 0.0002
195.5	$0.178 \pm 0.016 \pm 0.005$	0.1542 ± 0.0098	0.1648 ± 0.0002
199.5	$0.160 \pm 0.016 \pm 0.005$	0.1675 ± 0.0100	0.1641 ± 0.0003
201.7	$0.202 \pm 0.027 \pm 0.066$	0.1635 ± 0.0143	0.1638 ± 0.0002
205.2	$0.164 \pm 0.018 \pm 0.005$	0.1588 ± 0.0126	0.1633 ± 0.0003
206.7	$0.196 \pm 0.014 \pm 0.005$	0.1680 ± 0.0108	0.1631 ± 0.0003

Table 8.8: The results of the measurement of R_b compared to the combined LEP measurements, $R_b{}^{LEP}$, and the Standard Model prediction, R_b^{SM}. The quoted uncertainties on the combined LEP measurements contain the statistical and the systematic uncertainties added in quadrature. The Standard Model predictions are calculated with ZFITTER V6.35 [43] taking into account QED corrections, QCD corrections and weak corrections. The ZFITTER flags for the final state radiation and initial-final state radiation interference are set to FINR=0 and INTF=1. The theoretical uncertainties as quoted for σ_{had} due to the variation of the input parameters as discussed in section 2.7 are much smaller than the Standard Model prediction of R_b and basically caused by the large uncertainty on the mass of the Standard Model Higgs boson.

Chapter 9

Interpretation

The measurements of $\sigma_{\mathrm{had}}^{\mathrm{tot}}$ and$\mathrm{R_b}$ together with the measurements at the Z-resonance allow to study the vector and axial vector couplings of the Z boson to the bottom quark in the Standard Model and to test models beyond the Standard Model. The investigation of new phenomena in Elementary Particle Physics is enabled by studying deviations of the measured parameters from the Standard Model predictions. The analysis method and results obtained are presented in this chapter.

9.1 Analysis Method

The interpretation of the measurements in terms of couplings and scales is carried out by performing a χ^2-fit. The χ^2 function is then of the form,

$$\chi^2 = \sum_{\mathrm{i,j}} (\mathrm{x_i} - \mathrm{y_i(a)}) \mathrm{V_{ij}^{-1}} (\mathrm{x_j} - \mathrm{y_j(a)}), \tag{9.1}$$

where x is the vector of observations, y(a) is the vector of theoretical predictions containing the fit parameters a. The theory can be the Standard Model or another model. $\mathrm{V_{ij}}$ is the error matrix of the observations x given by:

$$\mathbf{V} = \begin{pmatrix} \mathrm{V_{11}} & \cdots & \mathrm{V_{1n}} \\ \vdots & \ddots & \vdots \\ \mathrm{V_{n1}} & \cdots & \mathrm{V_{nn}} \end{pmatrix}. \tag{9.2}$$

The individual matrix elements are given by:

$$\mathrm{V_{ij}} = \Delta^2_{\mathrm{stat}} + \Delta^2_{\mathrm{sys,uncorr}} + \Delta^2_{\mathrm{sys,corr}}, \quad \mathrm{i = j} \tag{9.3}$$

$$\mathrm{V_{ij}} = \Delta^{\mathrm{i}}_{\mathrm{sys,corr}} \cdot \Delta^{\mathrm{j}}_{\mathrm{sys,corr}}, \quad \mathrm{i \neq j}. \tag{9.4}$$

The error matrix, $\mathrm{V_{ij}}$, can be parametrised as a matrix of correlation coefficients multiplied by the vectors of total errors:

$$\mathrm{V_{ij}} = \mathrm{v} \rho_{\mathrm{ij}} \mathrm{v^T}. \tag{9.5}$$

The matrix elements of ρ_{ij} are one for the diagonal elements and the absolute values are between zero and one for the non-diagonal elements. The sign of non-zero values for the non-diagonal elements is either a plus for correlation and a minus for anti-correlation. A zero value for the non-diagonal elements indicates no correlation. The vectors of total errors are then:

$$v = \begin{pmatrix} \sqrt{V_{11}} \\ \vdots \\ \sqrt{V_{nn}} \end{pmatrix}, \tag{9.6}$$

where the elements V_{ii}, $(i = 1, \ldots n)$, are given above. In the case where the observations are statistically independent of each other, the matrix V_{ij} has only non-zero diagonal elements. Hence, the χ^2-function can be expressed as,

$$\chi^2 = \left(\sum_i \frac{(x_i - y_i(a))}{\sigma_i} \right)^2, \tag{9.7}$$

where σ_i are the uncertainties of the individual measurements. In the following, the minimisation of the χ^2-function is carried out by MINUIT [74], which provides values and errors for the fit parameters, a.

9.2 The Effective Vector and Axial Vector Couplings in the SM

The measurement of σ_{had} and R_b at high energies together with the measurements at the Z-resonance enable the study of the effective vector and axial vector couplings of the Z boson to bottom quarks. We have seen in section 2.7 that the dependence of σ_{had}, R_b and A_{fb}^b on the vector and axial vector couplings differs by an additional term from the equations at the Z-resonance ($\sqrt{s} = m_Z$). The $\gamma - Z$-interference becomes an important contribution and provides more information on the vector and axial vector couplings (see equation 2.42- 2.44).

At LEP I the effective vector and axial vector couplings entered only as quadratic sum and as products the pseudo-obesrvables σ_{had}^0, R_b^0 and $A_{fb}^{0,b}$ (see equation 2.91). Due to this fact, the values of the couplings and their signs cannot be distinguished. The ambiguity of the signs of $\bar{g}_V^b$ and $\bar{g}_A^b$ could be resolved because the $\gamma - Z$-interference provides terms proportional to $Q_e Q_b \bar{g}_A^e \bar{g}_A^b$ and $Q_e Q_b \bar{g}_V^e \bar{g}_V^b$. The sign of the couplings to the bottom quark is then determined with respect to the sign of the couplings to the electron and the electric charge of the bottom quark.

A χ^2-fit (see section 9.1) is performed to obtain the values of the effective couplings, $\bar{g}_V^b$ and $\bar{g}_A^b$. The χ^2-function is based on five parameters describing the lineshape of the Z-resonance. The measurement of these five parameters is carried out at LEP I. The five input parameters are listed in Table 9.1. The Standard Model predictions are calculated

on the basis of the set of Standard Model parameters as discussed in section 2.7. The five lineshape parameters are expressed in terms of the total width of the Z boson, Γ_Z, the hadronic decay width of the Z boson, Γ_{had}, the vector and axial vector couplings of the Z boson to the bottom quark, $\bar{g}_V^b$ and $\bar{g}_A^b$, and the vector and axial vector couplings of the Z boson to the leptons, $\bar{g}_V^l$ and $\bar{g}_A^l$. These six parameters will be the free parameters of the fit. The mass of the Z boson, m_Z, determines the exact position of the resonance

Parameter	Observed	Standard Model prediction
m_Z	91189.5 ± 3.1 MeV	–
Γ_Z	2502.5 ± 4.2 MeV	$2492.7^{+3.8}_{-5.2}$ MeV
σ^0_{had}	41.535 ± 0.055 nb	41.476 ± 0.012 nb
R^0_l	20.810 ± 0.060	20.733 ± 0.018
$A^{0,l}_{fb}$	0.0192 ± 0.0024	0.0151 ± 0.0012

Table 9.1: The input parameters from the Z-resonance measured at L3. The mass of the Z boson, m_Z, the total width of the Z boson, Γ_Z, determines the width of the Z-resonance the total hadronic cross section, σ^0_{had}, the ratio of the hadronic and the leptonic branching fractions of the Z boson, R^0_l, and the total leptonic forward-backward asymmetry, $A^{0,l}_{fb}$ [75]. The correlation matrix is listed in section C in Table C.1.

on the energy scale. The total width of the Z boson, Γ_Z, determines the decay width. The branching fractions of the Z boson, Γ_f (see section 2.4), determine the height of the resonance.
The ratio of the hadronic and leptonic branching fractions of the Z boson, $R^0_l = \Gamma_{had}/\Gamma_l$ (see equation 2.80 and 2.81), and the hadronic cross section, σ^0_{had}, at the Z resonance (see equation 2.91) depend both on the effective couplings, $\bar{g}_V^b$ and $\bar{g}_A^b$. The total leptonic forward-backward asymmetry, $A^{0,l}_{fb}$, depends on the effective vector and axial vector couplings of Z boson to the leptons. The asymmetries for the different final state lepton pairs e^+e^-, $\mu^+\mu^-$ and $\tau^+\tau^-$ are equal apart from corrections due to different lepton masses which are taken into account. This fact is understood as lepton universality and predicted by the Standard Model. On the basis of lepton universality, the coupling parameter of the electrons, $\mathcal{A}_e$, and the coupling parameter of the taus, $\mathcal{A}_\tau$, is extracted from the L3 measurement of the tau lepton polarisation and combined with the coupling parameter of the leptons obtained from the leptonic forward-backward asymmetries, $\mathcal{A}_e$, $\mathcal{A}_\mu$ and $\mathcal{A}_\tau$. The value of $\mathcal{A}_l$ is taken into account in the fit in order to constrain the leptonic effective vector and axial vector couplings [75]:

$$\mathcal{A}_l = 0.1575 \pm 0.0067. \tag{9.8}$$

In addition the measurements of σ_{had} and R_b presented in this work and previous measurements of σ_{had}, R_b and A^b_{fb} are used, starting from the measurements at the Z-resonance

up to the high energy measurements presented in this analysis. The measured values used in the fit are listed in Table 9.2. The measured values of σ_{had} and $\mathrm{R_b}$ are multiplied to

$\sqrt{s}$(GeV)	$\mathrm{R_b^{meas.}}$	$\mathrm{A_{fb}^{b,meas.}}$	$\sqrt{s}$(GeV)	$\sigma_{\mathrm{had}}^{\mathrm{tot,meas.}}$(pb)
m_Z	$0.2176 \pm 0.0015 \pm 0.0026$	0.1015 ± 0.0073	130	$84.2 \pm 4.4 \pm 1.0$
133	$0.177 \pm 0.023 \pm 0.005$	–	136	$66.6 \pm 3.9 \pm 0.8$
161	$0.152 \pm 0.035 \pm 0.005$	–	161	$37.3 \pm 2.2 \pm 0.7$
172	$0.212 \pm 0.045 \pm 0.007$	–	172	$28.2 \pm 2.2 \pm 0.6$
183	$0.145 \pm 0.020 \pm 0.004$	–	183	$24.7 \pm 0.8 \pm 0.4$
189	$0.163 \pm 0.013 \pm 0.005$	0.61 ± 0.20	189	$23.1 \pm 0.4 \pm 0.3$
192	$0.199 \pm 0.027 \pm 0.007$	–	192	$21.2 \pm 1.0 \pm 0.4$
196	$0.178 \pm 0.013 \pm 0.005$	–	196	$20.0 \pm 0.6 \pm 0.3$
200	$0.160 \pm 0.013 \pm 0.005$	–	200	$19.2 \pm 0.6 \pm 0.3$
202	$0.202 \pm 0.027 \pm 0.066$	–	202	$19.4 \pm 0.9 \pm 0.3$
205	$0.164 \pm 0.018 \pm 0.005$	–	205	$18.2 \pm 0.6 \pm 0.2$
207	$0.196 \pm 0.014 \pm 0.005$	–	207	$17.9 \pm 0.5 \pm 0.3$

Table 9.2: The results of $\sigma_{\mathrm{had}}^{\mathrm{tot}}$, $\mathrm{R_b}$ and $A_{\mathrm{fb}}^{\mathrm{b}}$ used in the χ^2-fit. The measurements are performed at L3 [72, 73, 76–79].

obtain the $\mathrm{b\bar{b}}$-production cross section (see equation 2.87). The correlations between σ_{had} and $\mathrm{R_b}$ are computed according to equation 9.4 using common systematic uncertainties of σ_{had} and $\mathrm{R_b}$ as listed in Table 7.4 and Table 8.6 as correlated systematic uncertainties, $\Delta_{\mathrm{sys,corr}}$. The results are listed in Table 9.3. The effective couplings, $\bar{\mathrm{g}}_{\mathrm{V}}^{\mathrm{b}}$ and $\bar{\mathrm{g}}_{\mathrm{A}}^{\mathrm{b}}$, can be replaced by left-handed and right-handed couplings, defined in equation 2.33 and 2.34. The results for the left- and right-handed couplings are listed in Table 9.4. In addition, a fit is performed to the combined heavy flavour measurements from the Z-resonance of the LEP experiments and the SLD experiment. The measured constraints are listed in Table 9.5 and Table 9.6. Furthermore, the combined leptonic coupling parameter, $\mathcal{A}_{\mathrm{l}}$, from LEP I and SLD is taken into account [47]:

$$\mathcal{A}_{\mathrm{l}} = 0.1501 \pm 0.0016. \tag{9.9}$$

The effective vector and axial vector couplings of leptons, bottom and charm quarks and the hadronic branching fraction and the total width of the Z boson are fitted jointly. The results of the fit to the LEP I and SLD measurements are listed in Table 9.7 and Table 9.8, respectively. In Figure 9.2 the results for $\bar{\mathrm{g}}_{\mathrm{V}}^{\mathrm{b}}$ and $\bar{\mathrm{g}}_{\mathrm{A}}^{\mathrm{b}}$ from the fit to the L3 measurements

Parameter	Fit	Standard Model	Deviation(σ)
$\bar{g}_V^b$	$-0.3024^{+0.0333}_{-0.0426}$	-0.3435	0.97
$\bar{g}_A^b$	$-0.5300^{+0.0273}_{-0.0184}$	-0.4985	1.15
$\bar{g}_V^e$	$-0.0397^{+0.0016}_{-0.0016}$	-0.0368	1.81
$\bar{g}_A^e$	$-0.5016^{+0.0005}_{-0.0005}$	-0.5013	0.60
Γ_{had}	$1751.1^{+3.8}_{-3.8}$ MeV	$1739^{+3.2}_{-4.1}$ MeV	2.34
Γ_Z	$2502.6^{+4.2}_{-4.2}$ MeV	$2492.7^{+3.8}_{-5.2}$ MeV	1.45

Table 9.3: The results of the free parameters obtained from the fit to the L3 measurements. The Standard Model predictions are calculated with ZFITTER V6.35 taking into account QED corrections, QCD corrections and weak corrections. The correlation matrix is listed in section C in Table C.2.

Parameter	Fit	Standard Model	Deviation(σ)
$\bar{g}_L^b$	$-0.4162^{+0.0082}_{-0.0082}$	-0.4215	0.65
$\bar{g}_R^b$	$+0.1137^{+0.0257}_{-0.0347}$	$+0.0775$	1.04

Table 9.4: The results for left- and right-handed couplings of the Z boson extracted from the fit to the L3 measurements compared to the Standard Model predictions calculated with ZFITTER V6.35 [43].

from the Z-resonance and the high energy measurements is compared to the result from the fit to the LEP I and SLD measurements from the Z-resonance only. In case of the L3 result the contour describes the 68% and the 95% confidence level. The LEP I and SLD results are depicted with the 68%, 95% and 99% confidence level contours, respectively. The Figure 9.3 depicts the results of the fit for $\bar{g}_L^b$ and $\bar{g}_R^b$ in the same way as for $\bar{g}_V^b$ and $\bar{g}_A^b$. The asterisk in both pictures denotes the Standard Model prediction for $\bar{g}_V^b$, $\bar{g}_A^b$ and $\bar{g}_L^b$, $\bar{g}_R^b$, respectively. The ambiguity as shown in the Figures 9.2 and 9.3 for the result obtained from the L3 data is resolved by the higher precision of the combined $A_{fb}^{0,b}$ measurements from LEP I as shown in the Figures for the LEP I combined data and the SLD data. Since $R_b^0 \approx (g_V^b)^2 + (g_A^b)^2$ and $A_{fb}^{0,b} \approx g_V^b g_A^b/[(g_V^b)^2 + (g_A^b)^2]$, R_b^0 can be pictured as a circle in the $g_V^b - g_A^b$-plane and $A_{fb}^{0,b}$ can be pictured as two straight lines in the $g_V^b - g_A^b$-plane with their origins at $(g_V^b, g_A^b) = (0, 0)$. This is depicted in Figure 9.1 from the measurement of R_b^0 and $A_{fb}^{0,b}$ of L3 at LEP I. The width of the circle is determined by the total uncertainty of R_b^0. The total uncertainty of $A_{fb}^{0,b}$ defines the four possible regions for the allowed values in the $g_V^b - g_A^b$-plane at 68% and 95% confidence level. The upper right quadrant is ruled out because the signs of $\bar{g}_V^b$ and $\bar{g}_A^b$ are determined w.r.t. the sign of the electron vector

and axial vector couplings and the electric charge of the bottom quark as mentioned in section 9.2.

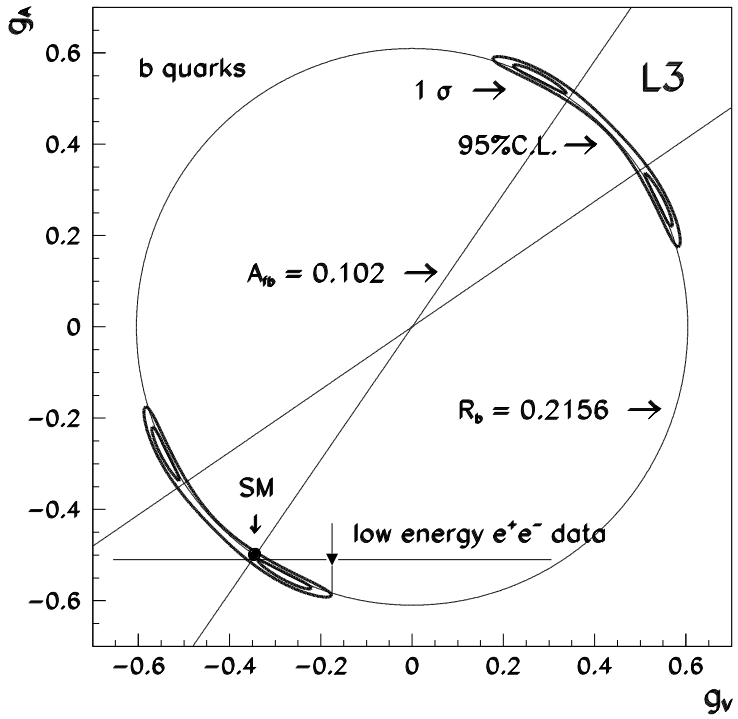

Figure 9.1: The Measurement of the effective couplings $\bar{g}_V^b$ and $\bar{g}_A^b$. The circle defined by R_b^0 and the straight lines defined by $A_{fb}^{0,b}$ measured at L3 at the Z-resonance. The intersection defines the possible regions for the allowed values of $\bar{g}_V^b$ and $\bar{g}_A^b$. The asterisk denotes the Standard Model prediction. In addition the results from the low energy e^+e^--experiments at PEP, PETRA and KEK are also shown [80].

Parameter	Value	Standard Model	Deviation(σ)
m_Z	91187.5 ± 2.1 MeV	–	–
Γ_Z	2495.2 ± 2.3 MeV	$2492.7^{+3.8}_{-5.2}$ MeV	1.09
σ^0_{had}	41.540 ± 0.037 nb	41.476 ± 0.012 nb	1.73
R_l	20.767 ± 0.025	20.733 ± 0.018	1.36
$A^{0,l}_{fb}$	0.0171 ± 0.0010	0.0151 ± 0.0012	2.00

Table 9.5: The input parameters from the Z-resonance from combined LEP measurements [47]. The correlation matrix is listed in section C in Table C.3.

Parameter	Value	Standard Model	Deviation(σ)
R^0_b(LEP)	0.21646 ± 0.00065	0.21578 ± 0.00018	1.12
R^0_c(LEP)	0.1719 ± 0.0031	0.17225 ± 0.00009	0.11
$A^{0,b}_{fb}$(LEP)	0.0990 ± 0.0017	0.1039 ± 0.0028	2.85
$A^{0,c}_{fb}$(LEP)	0.0685 ± 0.0034	0.0743 ± 0.0022	1.71
$\mathcal{A}_b$(SLD)	0.922 ± 0.020	0.935	0.65
$\mathcal{A}_c$(SLD)	0.670 ± 0.026	0.668	0.08

Table 9.6: Additional input parameters measured at the Z-resonance from LEP I and SLD measurements [47]. The correlation matrix is listed in section C in Table C.4.

The result from the fit to the LEP I and SLD measurements deviates by almost 3 standard deviations from the Standard Model predictions. This is mainly caused by the forward-backward asymmetry of the bottom quarks at the Z-resonance at LEP which is 2.8 standard deviations lower than the Standard Model prediction [47].

Parameter	Fit	Standard Model	Deviation(σ)
$\bar{g}_V^b$	$-0.3218^{+0.0076}_{-0.0080}$	-0.3435	2.71
$\bar{g}_A^b$	$-0.5146^{+0.0053}_{-0.0049}$	-0.4985	3.04
$\bar{g}_V^e$	$-0.0376^{+0.00036}_{-0.00036}$	-0.0368	2.22
$\bar{g}_A^e$	$-0.5013^{+0.00026}_{-0.00026}$	-0.5013	0.00
$\bar{g}_V^c$	$0.1841^{+0.0068}_{-0.0067}$	0.1911	1.03
$\bar{g}_A^c$	$0.5041^{+0.0052}_{-0.0053}$	0.5013	0.54
Γ_{had}	$1744.3^{+2.0}_{-2.0}$ MeV	$1739^{+3.2}_{-4.1}$ MeV	2.65
Γ_Z	$2495.2^{+2.3}_{-2.3}$ MeV	$2492.7^{+3.8}_{-5.2}$ MeV	1.09

Table 9.7: The results of the free parameters obtained from the fit to the LEP I and SLD measurements. The Standard Model predictions are calculated with ZFITTER V6.35 taking into account QED corrections, QCD corrections and weak corrections [47]. The correlation matrix is listed in section C in Table C.5.

Parameter	Fit	Standard Model	Deviation(σ)
$\bar{g}_L^b$	$-0.4182^{+0.0015}_{-0.0015}$	-0.4215	2.20
$\bar{g}_R^b$	$+0.0964^{+0.0062}_{-0.0066}$	$+0.0775$	2.86

Table 9.8: The results for left- and right-handed couplings of the Z boson extracted from the fit to the LEP I and SLD measurements and listed together with the Standard Model predictions.

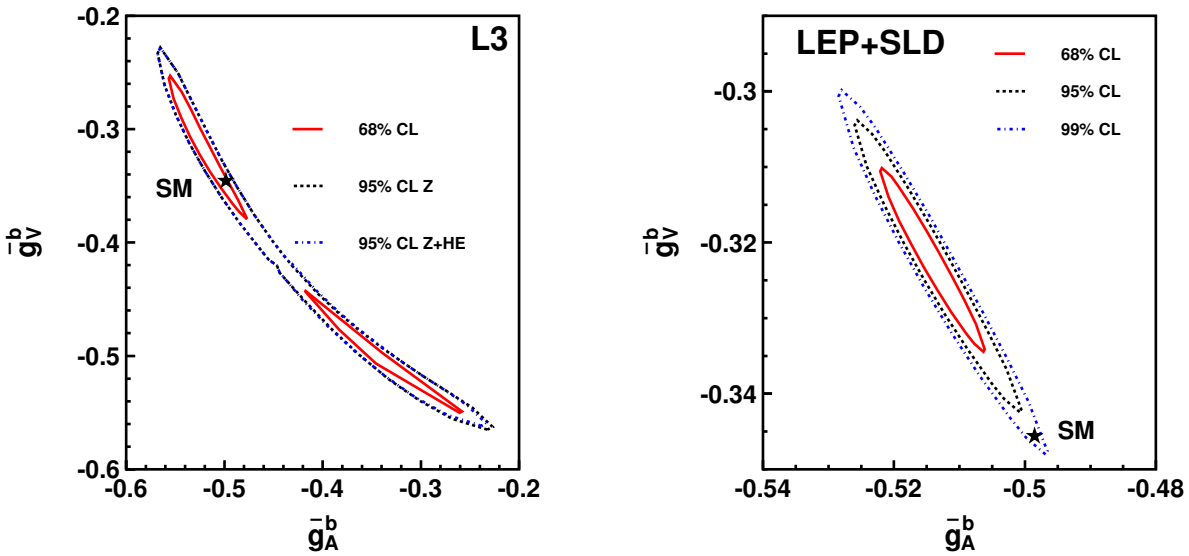

Figure 9.2: The left picture shows the results for $\bar{g}_V^b$ and $\bar{g}_A^b$ from the fit to the L3 measurements at 68% and 95% confidence level. The right picture shows the results for $\bar{g}_V^b$ and $\bar{g}_A^b$ from the fit to the LEP I and SLD measurements at 68%, 95% and 99%. The asterisk indicates the Standard Model prediction.

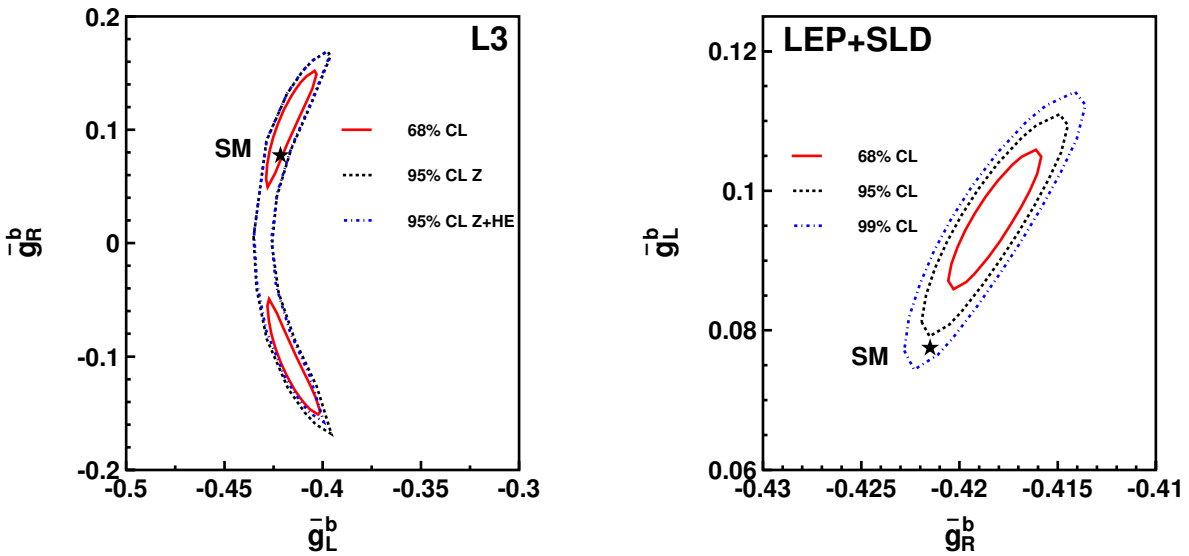

Figure 9.3: The picture shows the results for $\bar{g}_L^b$, $\bar{g}_R^b$ as for the effective vector and axial vector couplings in Figure 9.2.

9.3 New Physics

The previous section has shown that the results obtained from the fit to the combined measurements of LEP and SLD deviates by almost 3 standard deviations from the Standard Model predictions. The deviation might be caused by extensions of the Standard Model, dicussed in section 2.8. These extensions provide additional terms to the Standard Model cross section of electroweak interactions and explain the deviation in terms of new phenomena in Elementary Particle Physics.

9.3.1 Contact Interactions

In case of four-fermion contact interactions, the cross section is expressed in terms of helicity amplitudes (see subsection 2.8.1). The parameter η_{ik} as given in subsection 2.8.1 denotes the contribution to a certain helicity amplitude. The values for η_{ik} are listed in Table 9.9, the indices denote the helicity and the plus and the minus sign denote the constructive and destructive interference with the Standard Model terms, respectively. Assuming that contact interactions contribute with the same strengths to all

Model	LL	RR	LR	RL	VV	AA	V0	A0
η_{LL}	±1	0	0	0	±1	±1	±1	0
η_{RR}	0	±1	0	0	±1	±1	±1	0
η_{LR}	0	0	±1	0	±1	∓1	0	±1
η_{LR}	0	0	0	±1	±1	∓1	0	±1

Table 9.9: The parameters η_{ik} $(i, k = L, R)$ define to which helicity amplitudes the contact interactions contribute and hence determine the model.

quark flavours, the explicit inclusion of the $b\bar{b}$ cross section (R_b) in the analysis improve substantially the contact interaction limits for quarks. The cross sections are expressed in the modified helicity amplitudes (see equation 2.58 and equation 2.97). The χ^2-fit is carried out, taking $\varepsilon = 1/\Lambda^2$ as the free parameter of the fit, where $\varepsilon = 0$ in the limit that there are no contact interactions. The deviations of ε, achieved at 95% confidence level, are converted into lower limits of Λ. The limits are obtained by integrating over the physically allowed range from $\varepsilon \geq 0$ for Λ_+ and $\varepsilon \leq 0$ for Λ_-.
In Figure 9.4 the achieved results are depicted. The solid bars are obtained when only the hadronic cross section is taken into account. The hatched bars show a substantial improvement partially several TeV of the lower limits of Λ_- and Λ_+ when in addition the results of R_b are taken into account. The contact interactions are assumed to contribute to each quark flavour with equal strength and hence the effect partially cancels between the up-type and down-type quarks in the hadronic cross section. The explicit inclusion of the $b\bar{b}$ cross section in terms of R_b and σ_{had} resolves this effect.

	$q\bar{q}$		$b\bar{b}$		$q\bar{q}$ and $b\bar{b}$		$b\bar{b}$(LEP)	
	Λ_-	Λ_+	Λ_-	Λ_+	Λ_-	Λ_+	Λ_-	Λ_+
LL	3.5	5.0	9.8	7.1	9.8	6.4	9.3	11.8
RR	4.8	3.6	2.2	4.9	5.3	4.4	2.2	7.7
LR	4.5	3.9	2.8	3.9	4.5	4.1	3.1	5.5
RL	5.9	3.0	4.9	2.4	6.1	4.2	7.0	2.5
VV	7.1	5.0	2.7	8.2	9.0	7.1	10.0	13.3
AA	4.8	7.2	11.9	9.1	11.9	8.6	11.6	14.6
V0	5.9	3.0	11.3	8.5	10.7	7.3	11.0	13.9
A0	4.5	3.9	4.7	3.5	6.6	3.8	6.4	4.0

Table 9.10: The lower limits of Λ_- and Λ_+ in TeV at 95% confidence level. The first column contains the limits obtained from the hadronic cross section measured at L3. The second column contains the limits achieved from the $b\bar{b}$ cross section measurement at L3 only. The first column contains the limits in TeV obtained from the hadronic cross section and $b\bar{b}$ cross section measured at L3. The fourth column contains the limits in TeV achieved from the combined LEP measurements of the $b\bar{b}$ cross section [22]. Λ_- and Λ_+ refer to a destructive and constructive interference with the Standard Model, respectively. They correspond to the upper and lower signs of η_{ik} in Table 9.9.

The results for the hadronic cross section only and the hadronic cross section with the additional information of $b\bar{b}$ cross section are listed in Table 9.10. The limits on the four-fermion contact interactions including right-handed extensions, Λ^-_{RR} and Λ^+_{RL}, are lower than four the other chiralities (see Table 9.9).

9.3.2 Fermion Sizes

The introduction of non-vanishing fermion sizes is a specific form of contact interaction. In case of a measurable quark size, the cross section changes according to subsection 2.8.2. The fit is performed for the L3 and the combined LEP measurements assuming electrons to be point-like particles ($f_e(s) = 1$), but the size of the quarks to be variable and equal for all quark flavours. The upper limits for the size of the quarks are listed in Table 9.11. For the first time the fit is performed for bottom quarks only. The result is well compatible with the assumption that bottom quarks are point-like particles and therefore upper limits at 95% confidence level are set on the size of the quarks. Hence, the radius of the quarks is less than $1.3 \cdot 10^{-17}$cm.

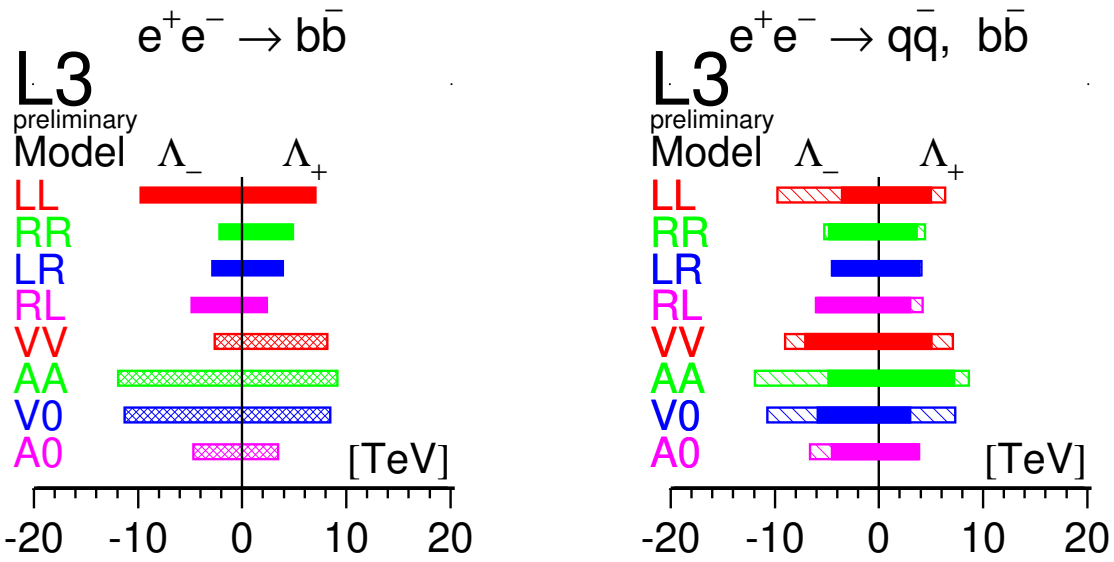

Figure 9.4: The left picture shows the lower limits on Λ_- and Λ_+ at 95% confidence level obtained for bottom quarks only (see second column in Table 9.10). The right picture shows the lower limits on Λ_- and Λ_+ at 95% confidence level obtained from the hadronic cross section and the $b\bar{b}$ cross section. The solid bars correspond to the results obtained from the hadronic cross section only (see first column in Table 9.10) and the hatched bars correspond to the results taking also into account the $b\bar{b}$ cross section (see third column in Table 9.10).

	R in 10^{-17} cm
L3 $q\bar{q}$	2.5
L3 $b\bar{b}$	6.4
LEP $q\bar{q}$	1.3

Table 9.11: The upper limits at 95% confidence level of the quark radius obtained from a fit to hadronic cross section measurements of L3 and the LEP combined analyses.

9.3.3 Extra Z Bosons

A more specific ansatz for a Standard Model extension is the introduction of an extra heavy gauge boson $m_{Z'}$ as discussed in subsection 2.8.3. A more detailed view on the Feynman diagram of the the four-fermion contact interaction shown in Figure 2.11 might be resolved introducing an extra boson as another mediator of forces acting between the fermions. The measurements carried out at the Z-resonance predict a small down to a

vanishing mixing between Z and Z′. The fits are performed obtaining lower limits at 95% confidence level on the mass, $m_{Z'}$, for the different models assuming no mixing of Z and Z′. The lower limits of the mass of an extra heavy gauge boson $m_{Z'}$ are listed in Table 9.12. Figure 9.5 shows the limits on $m_{Z'}$ obtained at 95% confidence level for the χ, ψ, η as

model	$m_{Z'}^{limit}$(L3)(GeV) with R_b	$m_{Z'}^{limit}$(LEP)(GeV)
χ	497	678
ψ	350	463
η	373	436
LR	435	800

Table 9.12: The lower limits of the Z′ mass for the χ, ψ, η and LR model at 95% confidence level achieved from a fit to the L3 measurements with R_b and the combined LEP measurements, respectively. Note that the lower limits on $m_{Z'}^{limit}$(LEP) are obtained for a mixing angle θ_M fixed to zero (see also [81]).

function of Θ_6 and for the LR model as function of α_{LR}. The dashed curves are obtained from a fit including only the R_b measurement as listed in Table 8.8. The solid curves are obtained including the measurements of σ_{had} as listed in Table 7.5, R_b and the leptonic cross section.

9.3.4 Graviton Exchange

In case of graviton exchange introduced in subsection 2.8.4, the free parameter is the mass scale M_s. The lower limits on M_s achieved from a fit to the L3 and the combined LEP measurements are listed in Table 9.13. Graviton exchange is excluded below 407 GeV

	M_s in GeV
L3 $q\bar{q}$	425
LEP $q\bar{q}$	407

Table 9.13: The lower limits of the mass scale M_s at 95% confidence level obtained from a fit to hadronic cross section measurements of L3 and the LEP combined analyses.

centre–of–mass energy.

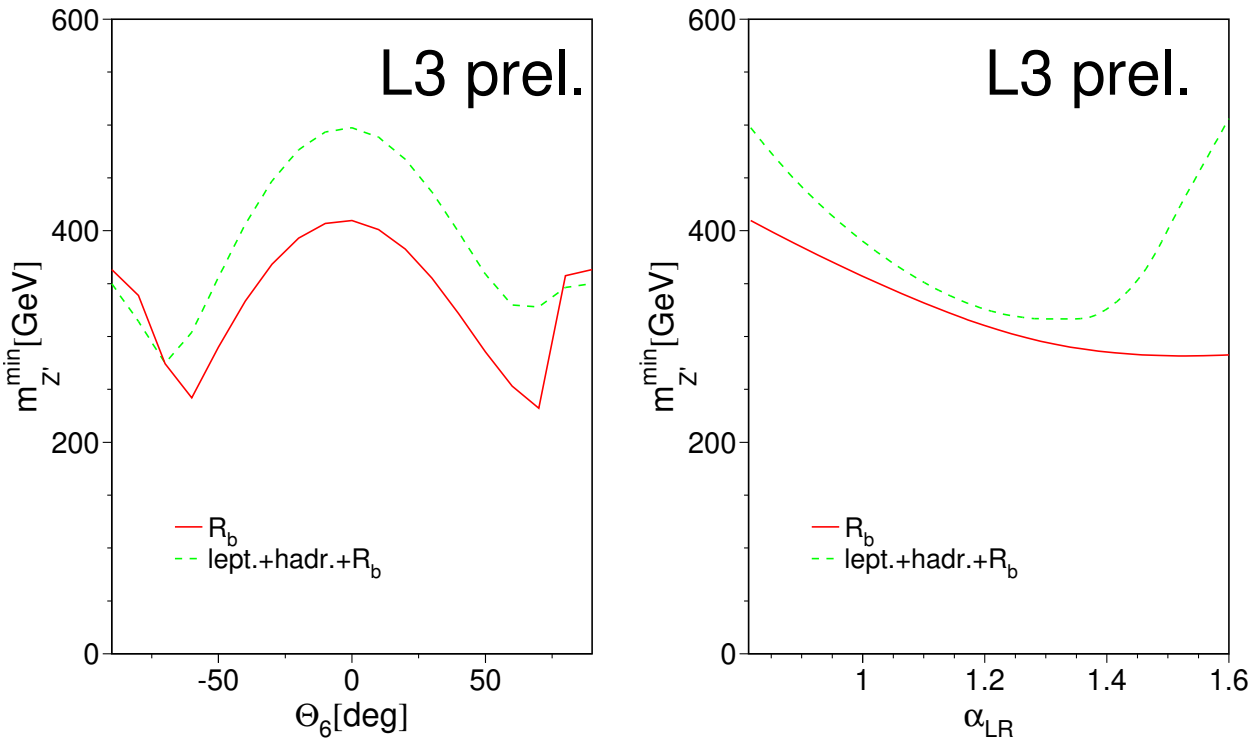

Figure 9.5: The results of the fit to the L3 measurements at 95% confidence level. The left picture shows the lower limit on $m^{limit}_{Z'}$ as function of Θ_6 including only the R_b measurement (dashed curve) and including the measurement of σ_{had}, R_b, the leptonic cross sections and asymmetries (solid curve). The right picture shows the two curves for $m^{limit}_{Z'}$ as function of α_{LR}.

Chapter 10

Conclusions and Outlook

The hadronic cross section, σ_{had} and the cross section ratio $\mathrm{R_b}$ at centre–of–mass energies from $\sqrt{\mathrm{s}} = 192$ GeV to $\sqrt{\mathrm{s}} = 207$ GeV are measured and listed in Table 10.1 and Table 10.2, respectively.
The results for the effective vector and axial-vector couplings of the Z boson to the bottom quarks are obtained by a χ^2-fit. The deviation is smaller than 1 standard deviation in case only L3 measurements are considered, but deviate by 3 standard deviations from the Standard Model prediction for the combined LEP and SLD measurements. In case of the combined LEP and SLD analyses, the deviation is mainly caused by the forward-backward asymmetry of the bottom quarks at the Z-resonance, which is 2.8 standard deviations smaller than the Standard Model prediction. The measurements are investigated for extensions of the Standard Model like contact interactions, non-vanishing size of the quarks, an extra heavy gauge boson and graviton exchange in extra dimensions. None of the studied extensions are able to explain the deviation. The vector and axial-

$\sqrt{\mathrm{s}}$(GeV)	$\sigma_{\mathrm{had}} \pm \Delta_{\mathrm{stat}} \pm \Delta_{\mathrm{sys}}$(pb)
191.6	$21.22 \pm 1.02 \pm 0.42$
195.5	$20.03 \pm 0.61 \pm 0.32$
199.5	$19.15 \pm 0.62 \pm 0.32$
201.7	$19.35 \pm 0.92 \pm 0.32$
205.2	$18.19 \pm 0.63 \pm 0.23$
206.7	$17.86 \pm 0.54 \pm 0.32$

Table 10.1: The measured hadronic cross sections, σ_{had}.

$\sqrt{\mathrm{s}}$(GeV)	$\mathrm{R_b^{meas.}} \pm \Delta_{\mathrm{stat}} \pm \Delta_{\mathrm{sys}}$
191.6	$0.199 \pm 0.027 \pm 0.007$
195.5	$0.178 \pm 0.016 \pm 0.005$
199.5	$0.160 \pm 0.016 \pm 0.005$
201.7	$0.202 \pm 0.027 \pm 0.066$
205.2	$0.164 \pm 0.018 \pm 0.005$
206.7	$0.196 \pm 0.014 \pm 0.005$

Table 10.2: The measurement of $\mathrm{R_b}$ for the corresponding centre–of–mass energies.

vector couplings as well as the left-handed and right-handed couplings obtained from a

Parameter	Fit L3	FIT LEP	Standard Model
$\bar{g}_V^b$	$-0.3024^{+0.0333}_{-0.0426}$	$-0.3218^{+0.0076}_{-0.0080}$	-0.3435
$\bar{g}_A^b$	$-0.5300^{+0.0273}_{-0.0184}$	$-0.5146^{+0.0053}_{-0.0049}$	-0.4985
$\bar{g}_L^b$	$-0.4162^{+0.0082}_{-0.0082}$	$-0.4182^{+0.0015}_{-0.0015}$	-0.4215
$\bar{g}_R^b$	$+0.1137^{+0.0257}_{-0.0347}$	$+0.0964^{+0.0062}_{-0.0066}$	$+0.0775$

Table 10.3: The comparison with the Standard Model prediction of the vector and axial-vector couplings and the left- and right-handed couplings obtained from the fit to the L3 measurements and to the combined LEP measurements, respectively.

χ^2-fit are listed in Table 10.3 for L3 and LEP combined, respectively. New phenomena in Elementary Particle Physics as investigated in terms of extensions of the Standard Model do not explain decisively the observed deviations from the Standard Model prediction. Hence, limits are set on the free parameters of the extended models.
The ansatz of contact interactions is model independent and does not assume specific structures of the interaction. The lower limits on the energy scales of the contact interactions show no indication of new phenomena in physics. The additional input of the measured cross section ratio, R_b improves the lower limits of the scale, Λ. The results are listed in Table 10.4. A deviation due to a possible substructure of the quarks can neither be confirmed nor excluded. Upper limits are set on the radius of all quark flavours jointly and on the radius of bottom quarks explicitly. The results are listed in Table 10.5. The introduction of an additional heavy gauge boson Z' is model dependent. The results of the four discussed models are inconclusive for the existence of an extra heavy gauge boson, $m_{Z'}$ as additional fundamental force. The lower limits on the mass of a Z' are improved by taking the measurement of R_b. The results from the fit to the L3 measurements are listed in Table 10.6. The exchange of gravitons due to the existence of extra dimensions can be excluded up to 407 GeV centre–of–mass energy. The achieved results from L3 and LEP combined measurements are listed in Table 10.7.

10.1 Conclusions

The Standard Model is confirmed up to 210 GeV centre–of–mass energy. The inclusion of the L3 measurements at centre–of–mass energies above the Z-resonance are not precise enough to significantly improve the uncertainties on the vector and axial-vector couplings of the Z boson to the bottom quarks. The precision of the current L3 measurements are of the order of 10%. In order to achieve a significant improvement, a precision of the order of 1% or better would be required.
Limits are set on the free parameters of the studied Standard Model extensions.
The deviation of the vector and axial-vector couplings and hence the left- and right-handed couplings of the Z boson to the bottom quarks is mainly caused by the forward-backward asymmetry on the Z-resonance, $A_{\mathrm{fb}}^{0,\mathrm{b}}$measured at LEP. There are eight independent measurements of $A_{\mathrm{fb}}^{0,\mathrm{b}}$from the four LEP collaborations (ALEPH, DELPHI, L3, OPAL). Each of the four LEP collaborations has measured $A_{\mathrm{fb}}^{0,\mathrm{b}}$in two independent ways. Either tagging a lepton (electron or muon) in the decay chain of the B hadron and conclude from the lepton charge on the charge of the final state quark or measuring the average charge of the resulting jet. When the combined leptonic coupling parameter, $\mathcal{A}_{\mathrm{e}}$, from LEP and SLD is taken into account, the coupling parameter of the bottom quark, $\mathcal{A}_{\mathrm{b}}$ can be extracted according to equation 2.91 and be compared to the result of the direct measurement of $\mathcal{A}_{\mathrm{b}}$ from SLD. All nine independent measurements of $\mathcal{A}_{\mathrm{b}}$ are below the Standard Model prediction. The probability for this is $(1/2)^9 \approx 2$ per mille [83, 84]. The leaves three possibilities:

1. **a statistical fluctuation:** very unlikely because of the high statistical precision of the measurements
2. **poorly understood systematic effect:** is under study by the LEP collaborations
3. **new physics:** different possibilities also w.r.t. the Standard Model Higgs boson are discussed [85], wait for future experiments

In order to understand this deviation, a more precise measurement of $A_{\mathrm{fb}}^{0,\mathrm{b}}$at the Z-resonance needs to be performed.

	$q\bar{q}$ and $b\bar{b}$		$b\bar{b}$	
	Λ_-	Λ_+	Λ_-	Λ_+
LL	9.8	6.4	9.8	7.1
RR	5.3	4.4	2.2	4.9
LR	4.5	4.1	2.8	3.9
RL	6.1	4.2	4.9	2.4
VV	9.0	7.1	2.7	8.2
AA	11.9	8.6	11.9	9.1
V0	10.7	7.3	11.3	8.5
A0	6.6	3.8	4.7	3.5

Table 10.4: The lower limits of Λ_- and Λ_+ at 95% confidence level [82].

	R in 10^{-17} cm
L3 $q\bar{q}$	2.5
L3 $b\bar{b}$	6.4
LEP $q\bar{q}$	1.3

Table 10.5: The upper limits on the radius of the quarks at 95% confidence level obtained from a fit to hadronic cross section measurements of L3 and the LEP combined analyses and the upper limit on the radius of the bottom quarks from L3 measurements.

model	$m_{Z'}^{limit}$(L3)(GeV)
χ	497
ψ	350
η	373
LR	435

Table 10.6: The lower limits of the Z′ mass for the χ, ψ, η and LR model at 95% confidence level achieved from a fit to the L3 measurements.

	M_s in GeV
L3 $q\bar{q}$	425
LEP $q\bar{q}$	407

Table 10.7: The lower limits of the mass scale M_s at 95% confidence level obtained from a fit to hadronic cross section measurements of L3 and the LEP combined analyses.

Appendix A

Jet Clustering Algorithm

Hadronic events are characterised by a large number of charged particle tracks and a large energy fraction deposited in the HCAL (see section 3.3.5) and the BGO (see section 3.3.3). The fragmentation of final state quarks boosts the particles in a certain direction. The tracks and energy depositions resulting from the fragmentation are clustered into jets. Here the JADE clustering algorithm is described more detailed. The clustering is carried out, computing a quantity y_{ij} for all pairs of particles:

$$y_{ij} = \frac{2(1-\cos\theta_{ij})\min(E_i^2, E_j^2)}{s}. \tag{A.1}$$

E_i and E_j are the energies of particle i and particle j, respectively. θ_{ij} is the angle between the particles. Then the two particles (i,j) with the smallest value of y_{ij} are combined and replaced by a 'pseudo-particle' with four-momentum $p_{(i,j)} = p_i + p_j$ and energy $E_{(i,j)} = |p_i + p_j|$, if their y_{ij} is smaller than a given resolution parameter, y_{cut}. The combination is repeated until all pairs of objects (particles and/or pseudo-particles) have $y_{ij} > y_{cut}$. y_{cut} is approximately given by $y_{cut} = M_j^2/s$, where M_j is the maximum invariant jet mass. The remaining objects are called jets. The masses of the particles and pseudo-particles are neglected in equation A.1 relative to an exact effective mass calculation. In Figure A.1 a typical four jet event, as seen in L3, is shown. The jet resolution parameter, y_{cut}, amounts to $y_{cut} = 0.08$. All kinematic and geometric information of a jet (jet energy, jet polar and azimuthal angles etc.) is obtained in a recursive way by iterative combination procedures of the original particles kinematic and geometric information.

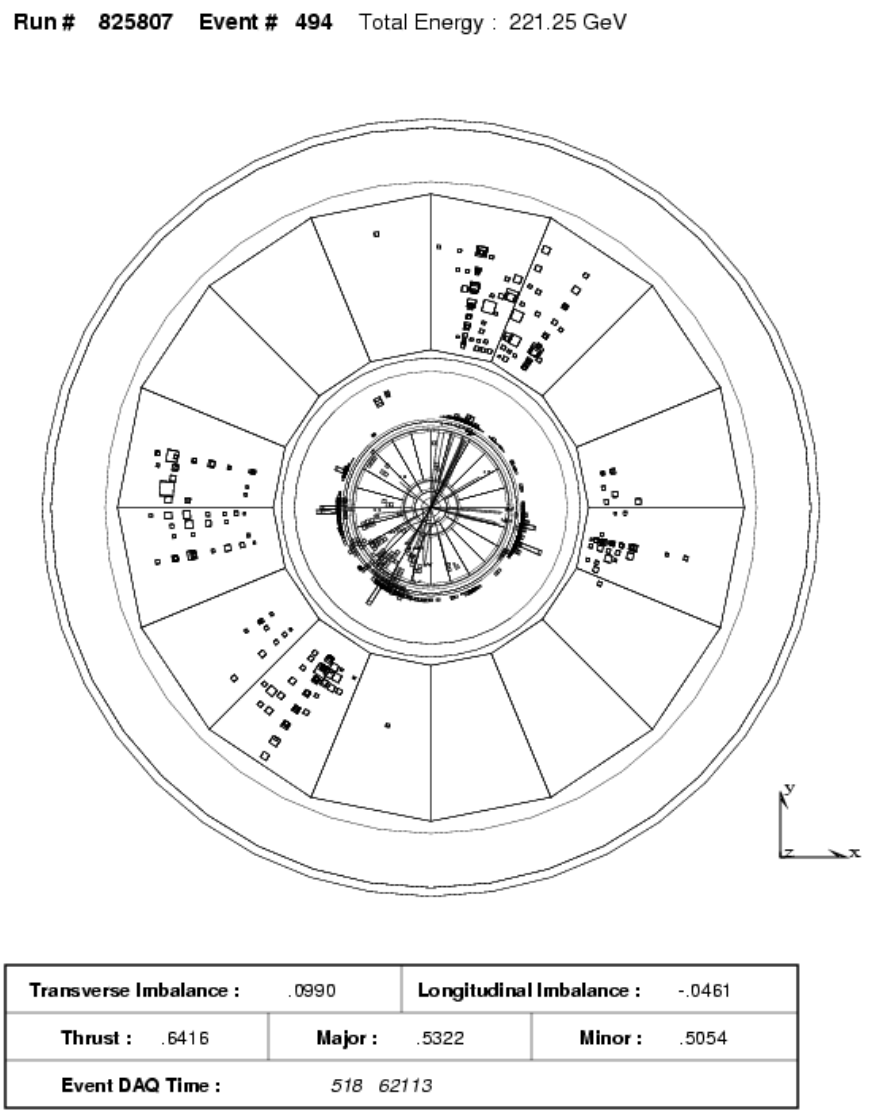

Figure A.1: A four jet event in the L3 detector. The front-view of the cross section of the L3 detector is shown. The particle tracks and energy depositions in the different subdetector shells are clustered in four jets.

Appendix B

Efficiency Calculation

The efficiency ε is obtained from a sample of N events of which n pass the selection. n is then a subsample of N. Usually, the efficiency ε is expressed as:

$$\varepsilon = \frac{\mathrm{n}}{\mathrm{N}}. \tag{B.1}$$

This is true, if the number of trials, N, and the efficiency, ε, are known and the number of reconstructed events, n, has to be determined. Usually the number of trials, N, and the number of reconstructed events, n, is known and the efficiency has to be computed. The probability to observe n events out of a sample of N trials is distributed according to the binomial distribution:

$$\mathrm{P}_\varepsilon(\mathrm{n}) = \binom{\mathrm{n}}{\mathrm{N}} \varepsilon^{\mathrm{n}} (1-\varepsilon)^{\mathrm{N}-\mathrm{n}}. \tag{B.2}$$

Without any prior knowledge of the efficiency, ε, except the assumption that the value of ε is certainly in an interval [0,1], the probability distribution of ε is according to Bayes' theorem and Bayes' postulate [86] computed as follows:

$$\mathrm{P}(\varepsilon) = \frac{\mathrm{P}_\varepsilon(\mathrm{n})}{\int\limits_0^1 \mathrm{d}\varepsilon \mathrm{P}_\varepsilon(\mathrm{n})}. \tag{B.3}$$

Using:

$$\int\limits_0^1 \mathrm{x}^{\mathrm{n}} (1-\mathrm{x})^{\mathrm{m}} \mathrm{dx} = \frac{\mathrm{n!m!}}{(\mathrm{n}+\mathrm{m}+1)!} \tag{B.4}$$

one obtains for the average value of ε:

$$\bar{\varepsilon} = \int\limits_0^1 \varepsilon \mathrm{P}(\varepsilon) \mathrm{d}\varepsilon = \frac{\int\limits_0^1 \varepsilon^{\mathrm{n}+1} (1-\varepsilon)^{\mathrm{N}-\mathrm{n}} \mathrm{d}\varepsilon}{\int\limits_0^1 \varepsilon^{\mathrm{n}} (1-\varepsilon)^{\mathrm{N}-\mathrm{n}} \mathrm{d}\varepsilon} = \frac{\mathrm{n}+1}{\mathrm{N}+2}. \tag{B.5}$$

Similarly for the average of ε^2:

$$\overline{\varepsilon^2} = \int_0^1 \varepsilon^2 \mathrm{P}(\varepsilon)\mathrm{d}\varepsilon = \frac{\int_0^1 \varepsilon^{\mathrm{n}+2}(1-\varepsilon)^{\mathrm{N}-\mathrm{n}}\mathrm{d}\varepsilon}{\int_0^1 \varepsilon^{\mathrm{n}}(1-\varepsilon)^{\mathrm{N}-\mathrm{n}}\mathrm{d}\varepsilon} = \frac{(\mathrm{n}+2)(\mathrm{n}+1)}{(\mathrm{N}+3)(\mathrm{N}+2)}. \tag{B.6}$$

Hence, one obtains for the standard deviation:

$$\sigma_\varepsilon = \sqrt{\overline{\varepsilon^2} - \bar{\varepsilon}^2} = \sqrt{\frac{(\mathrm{n}+1)(\mathrm{N}-\mathrm{n}+1)}{(\mathrm{N}+3)(\mathrm{N}+2)^2}}. \tag{B.7}$$

Therefore, efficiencies and their standard deviation are calculated as:

	Binomial	Standard
efficiency	$\varepsilon = \dfrac{\mathrm{n}+1}{\mathrm{N}+2}$	$\varepsilon = \dfrac{\mathrm{n}}{\mathrm{N}}$
standard deviation	$\Delta\varepsilon = \sqrt{\dfrac{(\mathrm{n}+1)(\mathrm{N}-\mathrm{n}+1)}{(\mathrm{N}+3)(\mathrm{N}+2)^2}}$	$\Delta\varepsilon = \dfrac{\sqrt{\varepsilon(1-\varepsilon)}}{\mathrm{N}}$

Table B.1: The comparison of the efficiency calculation and its standard deviation according to the binomial probability distribution and the standard way.

Appendix C

Correlation Coefficients

The correlations between the free parameters from the fits described in section 9.2.

	m_Z	Γ_Z	σ^0_{had}	R_l	$A^{0,l}_{fb}$
m_Z	1.00	0.06	0.01	0.07	0.04
Γ_Z		1.00	−0.35	0.00	0.02
σ^0_{had}			1.00	0.12	0.01
R_l				1.00	−0.02
$A^{0,l}_{fb}$					1.00

Table C.1: The correlations between the five input parameters from the L3 measurements presented in Table 9.1.

	$\bar{g}^b_V$	$\bar{g}^b_A$	$\bar{g}^e_V$	$\bar{g}^e_A$	Γ_{had}	Γ_Z
$\bar{g}^b_V$	1.000	−0.977	−0.662	0.221	−0.003	0.010
$\bar{g}^b_A$		1.000	0.652	−0.216	−0.026	−0.036
$\bar{g}^e_V$			1.000	−0.321	−0.003	−0.030
$\bar{g}^e_A$				1.000	0.080	−0.649
Γ_{had}					1.000	0.659
Γ_Z						1.000

Table C.2: The correlations between the free parameters of the fit to the L3 measurements.

	m_Z	Γ_Z	σ^0_{had}	R_l	$A^{0,l}_{fb}$
m_Z	1.000	−0.023	−0.045	0.033	0.055
Γ_Z		1.000	−0.297	0.004	0.003
σ^0_{had}			1.000	0.183	0.006
R_l				1.000	−0.056
$A^{0,l}_{fb}$					1.000

Table C.3: The correlations between the five input parameters from combined LEP measurements and SLD measurements as presented in Table 9.5.

	R^0_b	R^0_c	$A^{0,b}_{fb}$	$A^{0,c}_{fb}$	$\mathcal{A}_b$	$\mathcal{A}_c$
R^0_b	1.00	−0.14	−0.08	0.01	−0.08	0.04
R^0_c		1.00	0.04	−0.01	0.03	−0.05
$A^{0,b}_{fb}$			1.00	0.15	0.02	0.00
$A^{0,c}_{fb}$				1.000	0.00	0.01
$\mathcal{A}_b$					1.00	0.13
$\mathcal{A}_c$						1.00

Table C.4: The correlations between the combined LEP measurements and SLD measurements used in the fit.

	$\bar{g}^b_V$	$\bar{g}^b_A$	$\bar{g}^e_V$	$\bar{g}^e_A$	$\bar{g}^c_V$	$\bar{g}^c_A$	Γ_{had}	Γ_Z
$\bar{g}^b_V$	1.000	−0.956	−0.328	0.040	−0.171	0.034	−0.032	−0.021
$\bar{g}^b_A$		1.000	0.313	0.001	0.162	0.000	−0.072	−0.053
$\bar{g}^e_V$			1.000	−0.032	0.106	−0.050	−0.014	−0.040
$\bar{g}^e_A$				1.000	−0.016	−0.017	−0.380	−0.761
$\bar{g}^c_V$					1.000	−0.156	0.019	0.012
$\bar{g}^c_A$						1.000	0.056	0.040
Γ_{had}							1.000	0.703
Γ_Z								1.000

Table C.5: The correlations between the free parameters of the fit to the combined LEP measurements and SLD measurements.

Bibliography

[1] S. Weinberg, Phys. Rev. Lett., **19**, (1967), 1264.

[2] S. L. Glashow, Nucl. Phys., **22**, (1961), 579.

[3] A. Salam and J. C. Ward, Phys. Lett., **13**, (1964), 168.

[4] H. Fritzsch, M. Gell-Mann and H. Leutwyler, Phys. Lett., **B47**, (1973), 365.

[5] J. S. Schwinger, Phys. Rev., **82**, (1951), 664.

[6] P. W. Higgs, Phys. Lett., **12**, (1964) 132;
P. W. Higgs, Phys. Rev. Lett., **13**, (1964) 508;
P. W. Higgs, Phys. Rev., **145**, (1966) 1156;
F. Englert and R. Brout, Phys. Rev. Lett., **13**, (1964) 321;
G. S. Guralnik and C. R. Hagen, Phys. Rev. Lett., **13**, (1964) 585.

[7] J. Goldstone, A. Salam and S. Weinberg, Phys. Rev., **127**, (1962), 965.

[8] A. Kopp, DESY-THESIS-2000-009, (2000).

[9] M. J. G. Veltman, Nucl. Phys., **B123**, (1977) 89;
M. Consoli and S. Lo Presti and L. Maiani, Nucl. Phys., **B223**, (1983) 474;
J. Fleischer and F. Jegerlehner, Nucl. Phys., **B228**, (1983) 1.

[10] M. Gell-Mann, Phys. Lett., **8**, (1964), 214.

[11] G. Köpp, D. Schaile, M. Spira and P. M. Zerwas, Z. Phys., **C65**, (1995), 545.

[12] N. Cabibbo, Phys. Rev. Lett., **10**, (1963) 531;
M. Kobayashi and T. Maskawa, Prog. Theor. Phys., **49**, (1973) 652.

[13] X. Artru and G. Mennessier, Nucl. Phys., **B70**, (1974), 93.

[14] X. Artru, Phys. Rept., **97**, (1983), 147.

[15] R. Odorico, Nucl. Phys., **B172**, (1980), 157.

[16] G. C. Fox and S. Wolfram, Nucl. Phys., **B168**, (1980), 285.

[17] R. D. Field and S. Wolfram, Nucl. Phys., **B123**, (1983), 65.

[18] T. D. Gottschalk, Nucl. Phys., **B214**, (1983), 201.

[19] C. Peterson, D. Schlatter, I. Schmitt and P. M. Zerwas, Phys. Rev., **D27**, (1983), 105.

[20] V. G. Kartvelishvili, A. K. Likhoded and V. A. Petrov, Phys. Lett., **B78**, (1978), 615.

[21] LEPHF/2001-01 and references therein;
ALEPH Collab., D. Abbaneo *et al.*, ALEPH Note 2001-077 PHYSIC 2001-027;
DELPHI Collab., P. Abreu *et al.*, DELPHI Note 2001-134 PHYS-908;
L3 Collab., M. Acciarri *et al.*, L3 Note 2713;
OPAL Collab., G. Abbiendi *et al.*, OPAL Technical Note TN705;
SLD Collab., SLD PHYSICS NOTE 270.

[22] Particle Data Group, D. E. Groom *et al.*, Eur. Phys. J., **C15**, (2000), 1.

[23] O. Nachtmann, *Elementarteilchenphysik-Phänomene und Konzepte*. Vieweg u. Sohn, Braunschweig, 1986.

[24] A. Djouadi and M. Spira, Phys. Lett., **B228**, (1989), 443.

[25] A. Djouadi, ed. P. Zerwas, DESY 92-123B, (1992).

[26] G. 't Hooft and M. J. G. Veltman, Nucl. Phys., **B44**, (1972), 189.

[27] K. I. Aoki, Z. Hioki, M. Konuma, R. Kawabe and T. Muta, Prog. Theor. Phys. Suppl., **73**, (1982), 1.

[28] T. van Ritbergen and R. G. Stuart, Phys. Lett., **B437**, (1998), 201.

[29] T. van Ritbergen and R. G. Stuart, Phys. Rev. Lett., **82**, (1999), 488.

[30] W. F. L. Hollik, Fortschr. Phys., **38**, (1990), 165.

[31] G. Altarelli, R. Barbieri and F. Caravaglios, Nucl. Phys., **B405**, (1993), 3.

[32] A. A. Akhundov, D. Y. Bardin and T. Riemann, Nucl. Phys., **B276**, (1986), 1.

[33] M. Steinhauser, Phys. Lett., **B429**, (1998), 158.

[34] H. Burkhardt and B. Pietrzyk, Phys. Lett., **B356**, (1995), 398.

[35] M. Davier and A. Höcker, Phys. Lett., **B419**, (1998), 419.

[36] M. Davier and A. Höcker, Phys. Lett., **B435**, (1998), 427.

[37] S. Eidelman and F. Jegerlehner, Z. Phys., **C67**, (1995), 585.

[38] M. L. Swartz, Phys. Rev., **D53**, (1996), 5268.

[39] R. Alemany, M. Davier and A. Höcker, Eur. Phys. J., **C2**, (1998), 123.

[40] J. H. Kühn and M. Steinhauser, Phys. Lett., **B437**, (1998), 425.

[41] A. D. Martin, J. Outhwaite and M. G. Ryskin, Phys. Lett., **B492**, (2000), 69.

[42] H. Burkhardt and B. Pietrzyk, Phys. Lett., **B513**, (2001), 46.

[43] D. Bardin, Comput. Phys. Commun., **133**, (2001), 229.

[44] D. Bardin, G. Passarino and W. Hollik, CERN Report 95-03, (1995).

[45] K. Chetyrkin, j. Kühn and A. Kwiatkowski, CERN Report 95-03, (1995).

[46] A. B. Arbuzov, D. Y. Bardin and A. Leike, Mod. Phys. Lett., **A7**, (1992), 2029.

[47] CERN-EP/2001-098 and references therein;
LEPEWWG/2001-02;
ALEPH Collab., D. Abbaneo *et al.*, ALEPH Note 2001-078 PHYS 2001-028;
DELPHI Collab., P. Abreu *et al.*, DELPHI Note 2001-131 PHYS 906;
L3 Collab., M. Acciarri *et al.*, L3 Note 2723;
OPAL Collab., G. Abbiendi *et al.*, OPAL Note PR 350;
hep-ex/0112021;
see also http://www.cern.ch/LEPEWWG.

[48] LEP Higgs Working Group, (2001), **hep-ex/0107029**.

[49] E. Eichten, K. D. Lane and M. E. Peskin, Phys. Rev. Lett., **50**, (1983), 811.

[50] E. Fermi, Z. Phys., **88**, (1934) 161-177;
E. Fermi, Nuovo Cim., **11**, (1934) 1-19.

[51] L. S. Durkin and P. Langacker, Phys. Lett., **B166**, (1986), 436.

[52] A. Leike, S. Riemann, T. Riemann, Z-Z' mixing in presence of standard weak loop corrections, 1991, hep-ph/9808374.

[53] L3 Collab., O. Adriani *et al.*, Phys. Lett., **B306**, (1993), 187.

[54] N. Arkani-Hamed, S. Dimopoulos and G. R. Dvali, Phys. Lett., **B429**, (1998), 263.

[55] N. Arkani-Hamed, S. Dimopoulos and G. R. Dvali, Phys. Rev., **D59**, (1999), 086004.

[56] G. F. Giudice, R. Rattazzi and J. D. Wells, Nucl. Phys., **B544**, (1999), 3.

[57] J. A. Bakken *et al.*, Nucl. Instrum. Meth., **A275**, (1989) 81;
S. Lanzano *et al.*, Nucl. Instrum. Meth., **A289**, (1990) 335;
O. Adriani *et al.*, Nucl. Instrum. Meth., **A302**, (1991) 53;
B. Adeva *et al.*, Nucl. Instrum. Meth., **A323**, (1992) 109;
K. Deiters *et al.*, Nucl. Instrum. Meth., **A323**, (1992) 162;
M. Chemarin *et al.*, Nucl. Instrum. Meth., **A349**, (1994) 345;
M. Acciarri *et al.*, Nucl. Instrum. Meth., **A351**, (1994) 300;
G. Basti *et al.*, Nucl. Instrum. Meth., **A374**, (1996) 293;
A. Adam *et al.*, Nucl. Instrum. Meth., **A383**, (1996) 342.

[58] L3 Collab., M. Acciarri *et al.*, L3 note 1911, (1997).

[59] S. Jadach, W. Placzek, E. Richter-Was, B. F. L. Ward Z. Was, Comput. Phys. Commun., **102**, (1997), 229.

[60] B. F. L. Ward, S. Jadach, M. Melles and S. A. Yost, Phys. Lett., **B450**, (1999), 262.

[61] R. Brun, F. Bruyant, M. Maire, A. C. McPherson and P. Zanarini, CERN Report, DD/EE/84-1, (1987).

[62] H. C. Fesefeldt and F. Carminati, RWTH Aachen Report PITHA, 85/02, (1985).

[63] S. Jadach, B. F. L. Ward and Z. Was, Comput. Phys. Commun., **130**, (2000), 260.

[64] T. Sjøstrand, Comput. Phys. Commun., **82**, (1994), 74.

[65] S. Jadach, B. F. L. Ward and Z. Was, Comput. Phys. Commun., **79**, (1994), 503.

[66] R. Engel, Z. Phys. **C66**, (1995) 203;
R. Engel and J. Ranft, Phys. Rev. **D54**, (1996) 4244.

[67] F. A. Berends, R. Pittau and R. Kleiss, Comput. Phys. Commun., **85**, (1995), 437.

[68] M. Skrzypek, S. Jadach, W. Placzek and Z. Was, Comput. Phys. Commun., **94**, (1996), 216.

[69] L3 Collab., M. Acciarri *et al.*, Phys. Lett., **B411**, (1997), 373.

[70] L3 Collab., M. Acciarri *et al.*, L3 note 2630, (2000).

[71] D. Brown and M. Frank, ALEPH Note 92-135 PHYSIC 92-124, CERN, (1992).

[72] L3 Collab., M. Acciarri *et al.*, Phys. Lett., **B485**, (2000), 71.

[73] L3 Collab., M. Acciarri *et al.*, Phys. Lett., **448**, (1999), 152.

[74] F. James and M. Roos, Comput. Phys. Commun., **10**, (1975), 343.

[75] L3 Collab., M. Acciarri *et al.*, Eur. Phys. J., **C16**, (2000), 1.

[76] L3 Collab., M. Acciarri *et al.*, Phys. Lett., **B370**, (1996), 195.

[77] L3 Collab., M. Acciarri *et al.*, Phys. Lett., **B407**, (1997), 361.

[78] L3 Collab., M. Acciarri *et al.*, Phys. Lett., **B479**, (2000), 101.

[79] L3 Collab., M. Acciarri *et al.*, Eur. Phys. J., **C13**, (2000), 47.

[80] R. Marshall, Z. Phys., **C43**, (1989), 607.

[81] L3 Collab., M. Acciarri *et al.*, L3 note 2759, (2002).

[82] L3 Collab., M. Acciarri *et al.*, L3 note 2647, (2001).

[83] J. H. Field and D. Sciarrino, Mod. Phys. Lett., **A15**, (2000), 761.

[84] J. H. Field, private communication.

[85] M. S. Chanowitz, Phys. Rev. Lett., **87**, (2001), 231802.

[86] A. G. Frodesen, O. Skjeggestad and H. Tøfte, *Probability And Statistics In Particle Physics*. Universitetsforlaget, NORWAY Universitetsforlaget Box 2977 Tøyen Oslo 6, 1979.

Acknowledgements

In particular I wish to thank my advisor Sabine Riemann for her open mind and the fruitful discussions concerning physics in the last three years. I learned a lot about what the Standard Model means to a physicist. My colleagues of the L3 group in Zeuthen deserve a special thank for the opportunity to develope my skills and their constant support in various questions.
The work in the L3 collaboration offered the possibility to get to know many interesting people from all around the world and I enjoyed the numerous discussions about the different views on the world in all its vast variety. I am grateful to Simon Blyth, who taught how important it is to develope an efficient working style and introduced me in the details of the analysis of the forward-backward asymmetry measurement of bottom quarks. I thank John H. Field and Thomas Hebbeker for the careful reading of the manuscript.
This work would have been impossible without all the technicians, engineers and physicists that have built, maintained and succesfully ran the LEP machine and the L3 detector.
A special thank goes to my colleagues Sergei Likhoded, Alexei Raspereza, Michael Unger and Ricardo Vasquez Sierra for unforgettable social events. A warm and special thank goes to my parents and my girlfriend Nadine, who always supported me and hence my work and made this possible.

Hiermit erkläre ich, dass ich diese Arbeit selbständig verfasst und keine anderen als die angegebenen Quellen und Hilfsmittel benutzt habe.

Unterschrift